Fermilab

FERMILAB-THESIS-1993-15

# Determination of the Strong Coupling Constant ($\alpha_s$) and a Test of Perturbative QCD Using $W+$ Jets Processes in the DØ Detector

A Dissertation Presented

by

Jaehoon Yu

to

The Graduate School

in Partial Fulfillment of the Requirements

for the Degree of

Doctor of Philosophy

in

Physics

State University of New York
at
Stony Brook

August 1993

State University of New York
at Stony Brook

The Graduate School

Jaehoon Yu

We, the dissertation committee for the above candidate for the Doctor of Philosophy degree, hereby recommend acceptance of the dissertation.

---

dissertation director
professor Robert L. McCarthy

---

chairman of defense
Professor Paul D. Grannis

---

committee member
Professor George Sterman

---

committee member
Physics Department, Michigan State University
Professor Hendrik Weerts

---

outside member
Fermi National Accelerator Laboratory
Physicist Walter T. Giele

This dissertation is accepted by the Graduate School.

---

Graduate School

# Abstract of the Dissertation

# Determination of the Strong Coupling Constant ($\alpha_s$) and a Test of Perturbative QCD Using $W+$ Jets Processes in the DØ Detector

by

Jaehoon Yu

Doctor of Philosophy

in

Physics

State University of New York at Stony Brook

1993

The DØ experiment has accumulated data for a study of inclusive $W$ production corresponding to a total integrated luminosity of $14.3 \pm 1.7\, pb^{-1}$ during the 1992-1993 Fermilab Tevatron collider run. The total number of $W \rightarrow e+\nu$ candidates is 9770. The ratio of the number of $W+1$ jet events to that of $W+0$ jet events has been measured as a function of jet minimum $E_T$. Using this ratio the strong coupling constant, $\alpha_s$ at $Q^2 = M_W^2$ is measured to be $\alpha_s(M_W^2) = 0.124 \pm 0.005(stat) \pm 0.006(MC) \pm 0.008(theory)^{+0.026}_{-0.022}(sys)$ or $(^{+0.028}_{-0.025}$

combined) with a jet minimum $E_T$ of 25 GeV. A quantitative test of perturbative QCD has been made by comparing the experimentally measured ratio with the theoretical predictions. The theoretical predictions of the ratio in both the leading order and next-to-leading order are in good agreement with the measured ratio.

To my parents and my family.

# Contents

**List of Figures** . . . . . **xii**

**List of Tables** . . . . . **xiv**

**Acknowledgements** . . . . . **xv**

**1 Introduction** . . . . . **1**

1.1 Physics motivation . . . . . 1

1.2 Perturbative QCD and the strong coupling constant, $\alpha_s$ . . . . 3

1.3 Thesis organization . . . . . 8

**2 The DØ detector** . . . . . **10**

2.1 The DØ tracking system . . . . . 12

2.1.1 Vertex detector(VTX) . . . . . 14

2.1.2 Transition radiation detector (TRD) . . . . . 15

2.1.3 Drift chambers (CDC and FDC) . . . . . 17

2.2 The DØ calorimeter system . . . . . 18

2.2.1 Central calorimeter (CC) . . . . . 20

2.2.2 End calorimeter (EC) . . . . . 24

2.2.3 Massless gaps and the ICD . . . . . 28
2.3 The muon system . . . . . 28
2.4 Trigger and Data Acquisition system . . . . . 30
2.4.1 Level 0 . . . . . 30
2.4.2 Hardware trigger (The Level 1) . . . . . 31
2.4.3 Software triggers (The Level 2) . . . . . 32

**3 Data sample . . . . . 34**
3.1 Triggers . . . . . 34
3.1.1 Level 1 . . . . . 34
3.1.2 Level 2 . . . . . 36
3.2 Particle identification . . . . . 39
3.2.1 Interaction Vertex . . . . . 39
3.2.2 Electrons and photons . . . . . 41
3.2.3 Jets . . . . . 45
3.2.4 Muons . . . . . 51
3.2.5 Missing $E_T$ . . . . . 52
3.3 Offline selection criteria . . . . . 53
3.4 Total efficiency . . . . . 61
3.5 Final data sample . . . . . 62

**4 Backgrounds . . . . . 66**
4.1 QCD multi-jet events and instrumental effects . . . . . 68
4.2 Background from electroweak processes . . . . . 77
4.2.1 $Z \rightarrow e^+ + e^-$ . . . . . 77

4.2.2 $Z \rightarrow \tau^+ + \tau^-$ . . . . . 80
4.2.3 Drell-Yan $(q\bar{q} \rightarrow \gamma \rightarrow e^+ + e^-)$ . . . . . 83
4.2.4 $W[\rightarrow \tau(\rightarrow e\nu_e\nu_\tau) + \nu] + X$ . . . . . 84
4.3 Summary of estimated backgrounds . . . . . 84

**5 $\alpha_s$ determination . . . . . 88**
5.1 The theoretical cross section calculations . . . . . 89
5.2 DYRAD . . . . . 92
5.3 Method of $\alpha_s$ determination . . . . . 97

**6 Results . . . . . 101**
6.1 The ratio of the number of the $W + 1$ jet to the $W + 0$ jet events 101
6.2 Measured value of $\alpha_s$ . . . . . 105

**7 Conclusions . . . . . 108**

# List of Figures


1.1 Lowest order QCD vacuum polarization diagrams. . . . . 6

2.1 A cut away view of the DØ detector . . . . . 11

2.2 A cross section of the DØ tracking system . . . . . 13

2.3 A cut away view of the DØ calorimeter system. . . . . 18

2.4 A unit cell structure of the DØ calorimeter. . . . . 20

2.5 A block diagram of the DØ trigger and data acquisition system 33

3.1 $\chi^2$ distributions of electrons (unshaded), pions (shaded), and electrons from the $W$ . . . . . 43

3.2 dE/dx distributions in drift chambers . . . . . 45

3.3 Jet $E_T$ resolution of the DØ calorimeter. . . . . 47

3.4 Calorimeter relative response of jet to photon as a function of jet $E_T$ ($E_T^j$). . . . . 48

3.5 H-matrix $\chi^2$ distributions of electrons from $Z \rightarrow e^+e^-$ events from collider data in the CC. . . . . 56

3.6 H-matrix $\chi^2$ distributions of electrons from $Z \rightarrow e^+e^-$ events from collider data in the EC. . . . . 56

3.7 Isolation fraction distributions of electrons from $Z \rightarrow e^+e^-$ events from collider data in the CC. . . . . 57

3.8 Isolation fraction distributions of electrons from $Z \rightarrow e^+e^-$ events from collider data in the EC. . . . . 57

3.9 Track matching significance distributions of electrons from $Z \rightarrow e^+e^-$ events from collider data in the CC. . . . . 58

3.10 Track matching significance distributions of electrons from $Z \rightarrow e^+e^-$ events from collider data in the EC. . . . . 58

3.11 $E_T^e$ distributions for selected candidates for all $W$ (histogram), $W+0$ jet(solid circle), and $W+1$ jet (open circle) with $E_T^{min} >$ 25GeV. . . . . 62

3.12 $\not\!\!E_T$ distributions for selected candidates for all $W$ (histogram), $W+0$ jet(solid circle), and $W+1$ jet (open circle) with $E_T^{min} >$ 25GeV. . . . . 63

3.13 $M_T^W$ distributions for selected candidates for all $W$ (histogram), $W+0$ jet(solid circle), and $W+1$ jet (open circle) with $E_T^{min} >$ 25GeV. . . . . 64

3.14 $P_T^W$ distributions for selected candidates for all $W$ (histogram), $W+0$ jet(solid circle), and $W+1$ jet (open circle) with $E_T^{min} >$ 25GeV. . . . . 64

4.1 $\not\!\!E_T$ distributions for W+0j in CC. Open circles represent "good" electrons and solid circles are "bad" electrons. . . . . 70

4.2 $\not\!\!E_T$ distributions for W+1j in CC. Open circles represent "good" electrons and solid circles are "bad" electrons. . . . . 71
4.3 $\not\!\!E_T$ distributions for W+0j in EC. Open circles represent "good" electrons and solid circles are "bad" electrons. . . . . 71
4.4 $\not\!\!E_T$ distributions for W+1j in EC. Open circles represent "good" electrons and solid circles are "bad" electrons. . . . . 72
4.5 QCD background fraction for W+0j in CC vs jet minimum $E_T$ cut ($E_T^{min}$). . . . . 74
4.6 QCD background fraction for W+1j in CC vs jet minimum $E_T$ cut ($E_T^{min}$). . . . . 75
4.7 QCD background fraction for W+0j in EC vs jet minimum $E_T$ cut ($E_T^{min}$). . . . . 75
4.8 QCD background fraction for W+1j in EC vs jet minimum $E_T$ cut ($E_T^{min}$). . . . . 76
4.9 Effective cross section of $Z \rightarrow e^+ + e^-$ Monte Carlo samples ($\sigma_{eff}(Z \rightarrow e^+ + e^-)$ vs jet minimum $E_T$ cut ($E_T^{min}$) in the CC. 78
4.10 Effective cross section of $Z \rightarrow \tau^+ + \tau^-$ Monte Carlo samples ($\sigma_{eff}(Z \rightarrow \tau^+ + \tau^-)$) vs $E_T^{min}$ in the CC. . . . . 81
4.11 Effective cross section of $Z \rightarrow \tau^+ + \tau^-$ Monte Carlo samples ($\sigma_{eff}(Z \rightarrow \tau^+ + \tau^-)$) vs $E_T^{min}$ in the EC. . . . . 81

5.1 Some lowest order Feynmann diagrams for W+0 parton, 1 parton, and 2 parton processes . . . . . 94

6.1 Ratio of number of the $W + 1$jet and the $W + 0$jet events vs $E_T^{min}$ 102

6.2 $E_T$ distributions of the highest reconstructed jet associated with $W$. The two functions are emprical best fits to the data. . . . 104

6.3 Measured values of $\alpha_s$ as a function of jet minimum $E_T$ cut ($E_T^{min}$) 106

7.1 Extrapolated values of $\alpha_s$ using the DØ measurement. The dashed line is the extrapolation of $\alpha_s$ using the DØ measurement in Eq.7.2 . . . . . 109

# List of Tables


2.1 Characteristics of vertex and central drift chamber . . . . . 16

2.2 Central Calorimeter characteristics . . . . . 22

2.3 End Calorimeter characteristics . . . . . 25

2.4 Design parameters of the DØ muon system . . . . . 29

3.1 History of the Level 1 trigger . . . . . 35

3.2 Efficiencies of electron quality cuts . . . . . 59

4.1 Fraction of QCD background for W+0j and W+1j with the electron in the CC as a function of jet minimum $E_T$ cut ($E_T^{min}$) 68

4.2 Fraction of QCD background for W+0j and W+1j with the electron in the EC as a function of jet minimum $E_T$ cut ($E_T^{min}$) 69

4.3 $\sigma_{eff}(Z \rightarrow e^+ + e^-)$ for jet minimum $E_T$ cutoff ($E_T^{min}$) values in the CC. . . . . 79

4.4 $\sigma_{eff}(Z \rightarrow \tau^+ + \tau^-)$ for jet minimum $E_T$ cutoff in the CC. . . . 82

4.5 $\sigma_{eff}(Z \rightarrow \tau^+ + \tau^-)$ for jet minimum $E_T$ cutoff in the EC. . . . 83

4.6 Number of background events . . . . . 85

4.7 Number of signal events after background subtraction. . . . . 85

5.1 Parameters used for DYRAD Monte Carlo generation . . . . . 95

5.2 Parameters for cross sections in nb's using $MRSD^0$ parton distribution function. . . . . 100

6.1 Ratio of the number of the $W + 1$ jet and $W + 0$ jet events as a function of $E_T^{min}$. . . . . 103

6.2 $\alpha_s$ as a function of $E_T^{min}$ . . . . . 107

# Acknowledgements

My life in the DØ experiment began on January 1988 as a novice graduate student in the experiment. Since then, my entire life has been full of excitement. I was given many chances to carry out projects by myself as well as to supervise several different crews of people to get jobs done. All of my accomplishments couldn't have been possible without the great support from all the members of the DØ family. Therefore, I owe very special thank to all the people in the DØ family.

My special thanks to my advisor Bob McCarthy who has been incredibly patient with my English and has encouraged my own way of pursuing problems. I also owe a lot of appreciation to my friends Terry Heuring, Jerry Blazey, Srini Rajagopalan, Jim Cochran, Pat Mooney, and many others who helped me correcting my foolish English mistakes. A very special thank to the convener of the QCD group, Harry Weerts, who originally suggested this topic for my thesis, respected my idea, encouraged me, and spent a lot of time discussing with me. I also owe a special gratitude to Walter Giele, a theorist of the Fermilab theory division, who has been always willing to discuss physical aspects of experimental measurements, to discuss the theoretical backgrounds,

and to encourage me.

I owe many thanks to a lot of DØ physicists from whom I have learned a lot of different aspects of physics and have learned to widen my insight. Furthermore, I appreciate to DØ technical personnel who took my complaints and did their best to help me out.

I would like to dedicate this work to my parents who raised me and always encouraged me throughout my entire life with a strong support. Finally, I would like to thank to my wife Eunsun, my son Ryu, and my daughter Cheong for their incredible endurance duing past several years of painstaking life of a graduate student's family. Without their support at home, my research would have been much harder to carry out.

# Chapter 1

# Introduction

## 1.1 Physics motivation

High momentum transfer phenomena are known to be a clean way of identifying certain processes from hard interactions. These processes are predictable with perturbative QCD because of their short distance nature (high momentum transfer). Particle physics is concerned with how well a theory can explain observed physical phenomena with proper correlations of the physical observables. It is not always obvious how to measure the degree of accuracy of a theory. Therefore, one of the tasks given to particle physicists is to define a clear physical observable and to measure the observable as precisely as possible so that an unambiguous comparison of the theoretical prediction and the experimental results can be made.

After the discovery of weak vector bosons at CERN [1], an observable was found for a quantitative test of perturbative QCD prediction. The observable was the ratio of the cross sections of the $W + 1$ jet process and the $W + 0$

jet process. The ratio was used by both the UA1 and UA2 experiments to determine the strong coupling constant ($\alpha_s$) [2]. Since these processes involve a weak vector boson, the identification of the events in experiment can be done with little ambiguity. Furthermore, since the momentum transfer of these processes involving the $W$ vector boson is sufficiently high (on the order of the mass of $W$), a theoretical prediction by the perturbative QCD is reliable.

Recent progress in theory has improved the prediction of the cross sections of the $W + 0$ jet [3] and the $W + 1$ jet [4] processes to next-to-leading order. In addition, the technique of the parton final state phase space Monte Carlo integration [4] made it possible to do more realistic theoretical predictions of the ratio. From the experimental point of view, the Fermilab Tevatron has achieved remarkable improvements in delivering higher luminosity. This, together with improvements in experimental techniques, has greatly increased the number of $W$ events collected. These recent improvements in both the theory and the experiment have enabled a more precise comparison between theoretical prediction and the experimental results of the ratio. It has also been found that the global behavior of the ratio as a function of jet minimum transverse energy cuts ($E_T^{min}$) provides yet another means of a more precise and a quantitative test of perturbative QCD [5]. At the same time, the observable can also provide a means of determining the strong coupling constant, $\alpha_s$.

In this thesis, the ratio of the number of the $W + 1$ jet, $N_{W+1jet}(E_T^{min})$,

and the $W + 0$ jet, $N_{W+0jet}(E_T^{min})$, events,

$$R_{data}(E_T^{min}) = \frac{N_{W+1jet}(E_T^{min})}{N_{W+0jet}(E_T^{min})}, \tag{1.1}$$

is measured from events with the $W$ decaying into $e + \nu$ final states as a function of $E_T^{min}$. The measured values of the ratio are then compared with perturbative QCD predictions for a quantitative test of the theory. Furthermore, the strong coupling constant is determined using the relationship between the experimentally measured ratio and the theoretical prediction.

## 1.2 Perturbative QCD and the strong coupling constant, $\alpha_s$

Quantum Chromo-dynamics, QCD in short, is a quantum field theory describing the strong interaction, one of three known fundamental interactions in nature (gravitational, electroweak, and strong interaction). In QCD the strong interaction is interpreted as the interaction between color charged quarks [6]. The color charges are just another kind of quantum number. There are three color charges (red, green, and blue) and corresponding anti colors. The forces between color charged quarks are then mediated by colored field quanta (gauge particles called gluons [7]). The first evidence of the existence of gluons came from an $e^+e^-$ collider experiment. Since $e^+$ and $e^-$ annihilate into a photon via electroweak interaction, the final state was expected to be two quarks from the decay of the photon. This is because the mediator of strong interaction does not interact with photons, one of the mediators of

electroweak interaction, so that the photon would not decay into gluons. The quarks in the final state would then turn into streams of strongly interacting colorless particles (hadrons) because the strong interaction is very strong no colored state can be observed. These streams of hadrons are called jets (see section 3.2.3). However, if there was a gluon which can be radiated from a colored quark then more than two jets would result in the final state. Since gluons are also colored, they also turn into jets so that the final state would have three jets. The first evidence of three jet events was found in experiments at PETRA [8].

Characteristics of hadrons resulting from a hard interaction can be described well by the quark model. On the other hand, an isolated quark has never been observed. Evidently, the forces between quarks are strong. Nevertheless, cross sections at high enough energy are well described by a model that quarks do not interact at all between themselves. In other words at short distances, equivalently at large momentum transfer, the effective coupling constant vanishes. This phenomenon is called *asymptotic freedom.* Asymptotic freedom is a property of a renormalizable field theory with a non-Abelian gauge field [9]. The concept of asymptotically free gauge field theory with color quantum numbers needed to be introduced to explain the dynamics of the Bjorken scaling [10] which was experimentally proved from deep inelastic lepton-nucleon scattering in late 1960's.

The basic premise of QCD is that the strong interaction is a copy of electromagnetic interaction. In other words, the interaction between partons with color charges can be interpreted in the same way as electromagnetic in-

teraction between electrically charged objects. Then the color charge can be interpreted in the same way as electrical charge. Since in Quantum Electro-Dynamics (QED) an electron can continuously emit and absorb photons and the photons can convert into electron-positron pairs, the electron is pictured as surrounded by virtual electron-positron pairs. However, since opposite charge attracts, the positrons will preferentially be closer to the original electron. The vacuum surrounding the electron becomes polarized thus screening the real charge of the electron (*vacuum polarization*). Therefore, the charge of the electron appears smaller when probed from long distances. Consequently, the charge effectively increases as the probing distance decreases. This property of the vacuum polarization affects the effective coupling in QED,

$$\alpha(Q^2) = \frac{\alpha(Q_0^2)}{1 - \frac{\alpha(Q_0^2)}{3\pi} log(\frac{Q^2}{Q_0^2})}. \tag{1.2}$$

The change in the value of the effective coupling ($\alpha$), as one goes from a process involving a typical momentum transfer $Q_0^2$ to one involving $Q^2 (> Q_0^2)$, depends logarithmically on the ratio $\frac{Q^2}{Q_0^2}$. Equation 1.2 is obtained by summing the higher order corrections, involving terms of the general form $\alpha^n [log(\frac{Q^2}{Q_0^2})]^m$, but retaining only the leading logarithms (i.e., m=n, leading log approximation).

The same analogy can be applied to the color charge of a quark. The screening of the color charge of a quark would have been exactly the same as that of electron if gluons did not carry color charge themselves. However, due to the non-Abelian property (generators in the SU(3) group do not commute with each other) of QCD, the gluons themselves couple to each other.

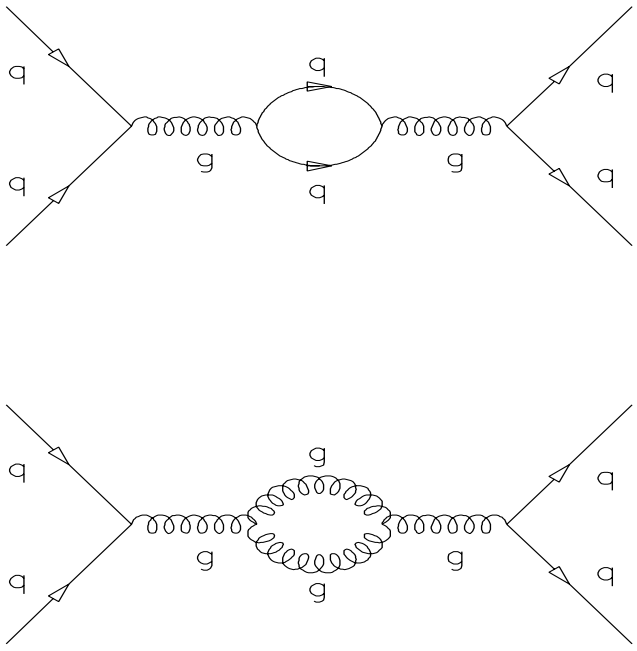


Figure 1.1: Lowest order QCD vacuum polarization diagrams.

Therefore, since a gluon emitted from the quark can turn into a gluon pair, the screening process receives contributions from yet another type of vacuum polarization diagrams (the bottom diagram in Fig. 1.1). Certain states of polarization of the gluon pairs in the loop diagrams produce an antiscreening effect. As a consequence the effective color charge decreases, unlike in QED, as one probes closer to the original quark. The two lowest order diagrams of QCD vacuum polarization are shown in Fig. 1.1. This antiscreening effect causes the *asymptotic freedom* phenomena.

These vacuum polarization loop diagrams contribute to divergences in perturbative QCD calculation. These divergences are equivalent to the violations of energy conservation caused by virtual states. To overcome these di-

vergences, Ultra Violet (UV) divergences, a renormalization is necessary. The renormalization is a systematic way of removing the divergences. To renormalize a theory, a parameter must be introduced to scale the momentum. This scale has a dimension of a mass and is called renormalization scale ($\mu$). This parameter is completely arbitrary. Therefore, it is necessary to specify rules determining the values of the scale $\mu$ for each divergence. These rules are called renormalization schemes. There are two well known schemes. One is the *momentum subtraction* scheme where the scale $\mu$ is chosen such that the mass of the propagator to be zero at a fixed set of momenta. Therefore, in this scheme the value of parameter $\mu$ varies depending on the divergent loop integrals. The other scheme is the *minimal subtraction* scheme where the scale $\mu$ is chosen the same for all divergent integrals and appears as a free parameter in renormalized cross sections. This scheme is favored by many perturbative $QCD$ calculations. The theoretical prediction used in this analysis uses a *modified minimal subtraction* scheme ($\overline{MS}$ scheme).

The vacuum polarization diagrams give, after the renormalization and the leading logarithmic approximation, the QCD running coupling constant,

$$\alpha_s(Q^2) = \frac{\alpha_s(\mu^2)}{1 + \frac{\alpha_s(\mu^2)}{12\pi}(11N_c - 2n_f)log(Q^2/\mu^2)} \tag{1.3}$$

where $N_c$ is the number of color charges and $n_f$ is the number of the light quark flavors at the $Q^2$ scale. At a sufficiently low $Q^2$ the effective coupling becomes large as can be inferred from equation 1.3. It is customary to denote this scale as $\Lambda^2_{QCD}$, where

$$\Lambda^2_{QCD} = \mu^2 exp[\frac{-12\pi}{(11N_c - 2n_f)\alpha_s(\mu^2)}] \tag{1.4}$$

Then $\alpha_s(Q^2)$ in equation 1.3 becomes

$$\alpha_s(Q^2) = \frac{12\pi}{(11N_c - 2n_f)log(Q^2/\Lambda^2_{QCD})}. \quad (1.5)$$

For $Q^2$ of order $\Lambda^2_{QCD}$, the effective coupling becomes large so quarks and gluons arrange themselves into strongly bound states , namely hadrons (*quark confinement*). Therefore, $\Lambda_{QCD}$ can be interpreted as the scale which determines the range of momentum transfer for reliable perturbative QCD calculations.

To summarize this section, the perturbative QCD is the theory describing the strong interaction in the high momentum transfer phenomena. However, the theory has limits in its reliability. The limit can be determined by the scale $\Lambda_{QCD}$ which can not be predicted by the theory. The only way to determine $\Lambda_{QCD}$ is by measuring the strong coupling constant ($\alpha_s$) from experiments. Therefore, a precise measurement of the strong coupling constant is necessary. In addition, once the value of $\Lambda_{QCD}$ is determined at a certain $Q^2$, $\alpha_s$ at any $Q^2$ can be determined using the relationship in Eq. 1.5. Furthermore, the theoretical prediction of physical observables with a certain $Q^2$ can be done reliably.

## 1.3 Thesis organization

The DØ detector is a large multi-purpose detector commissioned at the DØ collision hall at the Fermilab Tevatron collider. The design of the DØ detector focuses on high transverse momentum ($P_T$) phenomena at the center

of mass energy of $\sqrt{s} = 1.8$ TeV. The emphasis is on accurate measurements of transverse energy ($E_T$) and missing $E_T$ ($\not\!\!E_T$ ) with a good hermeticity of the detector. The DØ detector is discussed in more detail in chapter 2.

Interpretation of the recorded data is important. The reconstruction program assigns the identities of observed objects. The reconstruction (or identification) algorithms of physical objects are discussed in chapter 3 together with the data reduction processes and offline selection criteria.

The physical observable used in this analysis, the ratio between the $W+1$ jet and $W+0$ jet cross sections is very sensitive to background subtraction. We, therefore, discuss the estimation of background from various processes in chapter 4.

Theoretical prediction of this observable plays a very important role in determining the strong coupling constant, $\alpha_s$. In chapter 5 some theoretical aspects, the Monte Carlo, and the method of $\alpha_s$ determination are discussed.

In chapter 6 we discuss the ratio of the $W+0$ jet and the $W+1$ jet cross section. The ratio is compared with next-to-leading order perturbative QCD prediction for various $\alpha_s$ values. Global behavior of the ratio is discussed. Finally the value of the measured strong coupling constant is presented.

Chapter 7 concludes this analysis.

# Chapter 2

# The DØ detector

The DØ detector illustrated in Fig. 2.1, consists of three major detector systems which surround the interaction point at Fermilab's DØ collision hall. The three systems are a tracking system, a calorimeter system, and a muon system. The tracking system, illustrated in Fig. 2.2, consists of four different detectors. In the central portion of the detector covering pseudorapidity ($\eta \equiv -ln[tan\frac{\theta}{2}]$, where $\theta$ is the polar angle from the beam axis) from approximately -1.2 to +1.2 is the transition radiation detector (TRD), and the central drift chamber(CDC). The vertex detector (VTX) covers the pseudorapidity region from approximately -2.0 to +2.0. These three chambers form concentric cylinders around the beam pipe which carries protons and antiprotons to the collision point. The direction protons proceed is defined as the positive $z$. The pseudorapidity range $3.1 > |\ \eta\ | > 1.4$ is covered by forward and backward drift chambers (FDC). The DØ detector does not have a central magnetic field. The absence of a central magnetic field makes the detector compact.

The DØ calorimetry consists of uranium/liquid argon ($LAr$) sampling cal-

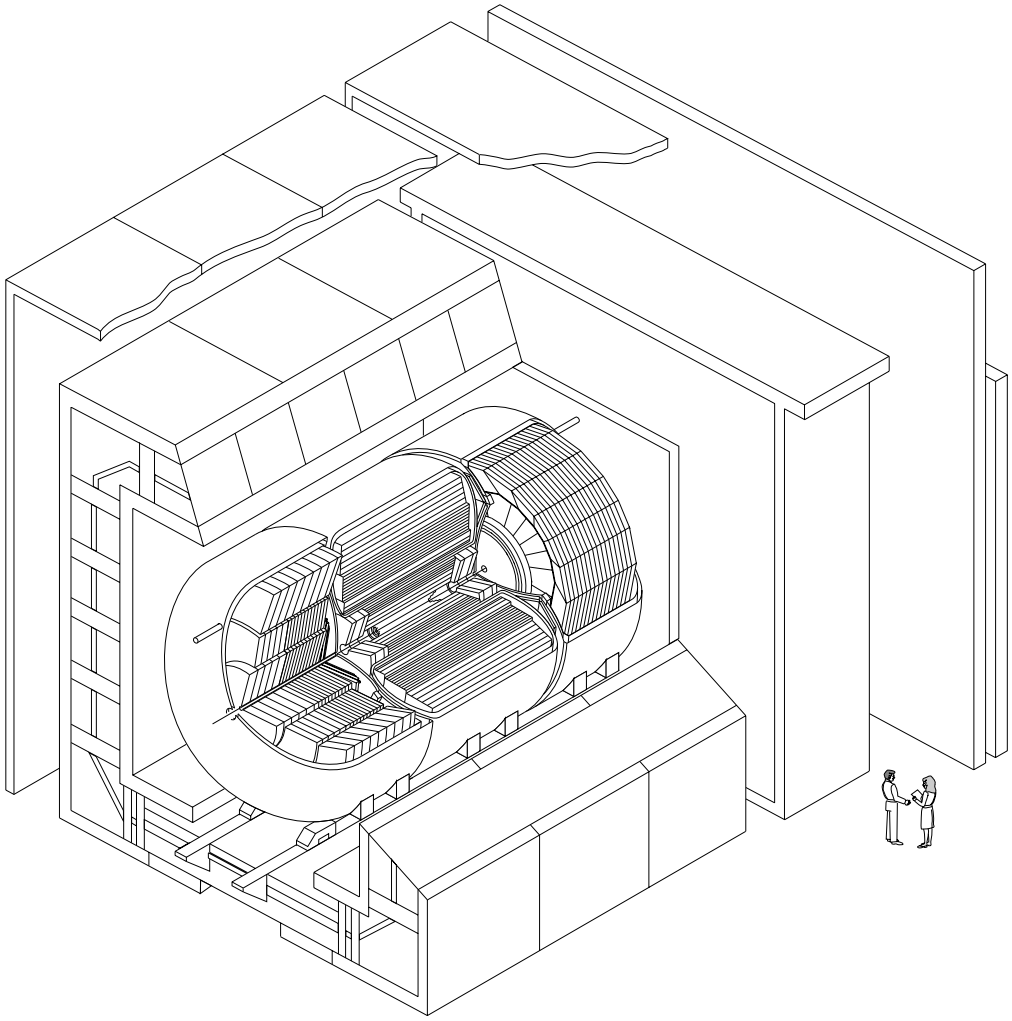

Figure 2.1: A cut away view of the DØ detector

orimeters. The calorimeter system has three major detectors covering different ranges in pseudorapidity. The central calorimeter (CC) covers the pseudorapidity range of $\mid \eta \mid < 1.1$ and the two end calorimeters (EC) cover a larger pesudorapidity range, $1.1 < \mid \eta \mid < 4.5$.

The muon system surrounds all the other detector systems. It has three layers of chambers. The inner-most layer, the closest layer to the interaction point, is called the $A$ layer. This layer is followed by a toroidal magnet system with a localized field and subsequent B and C layers. The track impact point in the three layers is used to determine the bend angle in the magnetic field from which the muon momentum is inferred. The muon system has pseudorapidity coverage up to approximately 3.7 units in pseudorapidity.

## 2.1 The DØ tracking system

The tracking system is very important for this analysis because the identification of an electron relies not only on the shape of calorimeter energy clusters in the electromagnetic part of the detector but also on the matching between the cluster position in the calorimeter and the track position in the tracking systems. Good spatial resolution in $\eta - \phi$(azimuthal) space is essential to identify whether an electromagnetic energy cluster in the calorimeter is due to an electron or a photon. The tracking system plays an important role in identifying the multiplicity of overlapping charged particles by making use of pulse heights and comparing them to minimum isonizing particles (MIP).

The DØ tracking system, illustrated in Fig. 2.2, consists of three different

Figure 2.2: A cross section of the DØ tracking system

detector systems in the central pseudorapidity region. First, the vertex chamber surrounds the interaction point $2\pi$ in azimuth ($\phi$) from an inner radius of 3.7cm to an outer radius of 16.2cm. This detector is intended to be used for good determination of the interaction vertex which is crucial for determining the $E_T$ of objects from hard interactions. Second, for good electron identification three concentric layers of the transition radiation detector surround the vertex detector. Third, the central drift chamber follows immediately after the

transition radiation and just before the electromagnetic calorimeter. The CDC is intended for identification of the trajectories of the charged particles from the interaction and the determination of the position of the interaction vertex. The location of the central drift chamber was chosen so that a conversion of a photon to an $e^+e^-$ pair can be identified before reaching the calorimeter. Table 2.1 summarizes characteristics of the vertex chambers and the central drift chambers.

Forward drift chambers on either side of the interaction point just before the end electromagnetic calorimeters provide tracking coverage at large $\eta$. These chambers also provide good spatial resolution of charged particle trajectories and hermetic coverage around the interaction point.

A detailed description of each of the detector follows.

### 2.1.1 Vertex detector(VTX)

In a collider experiment it is very important to determine the vertex of a hard interaction for an accurate measurement of transverse energy of an object. The vertex chamber is designed to provide precise measurements of charged tracks in the vicinity of the interaction region in order to provide information in reconstructing the interaction vertex. The walls of the vertex chamber are made of a low density material (carbon fiber) to minimize the rate of photon conversions to $e^+e^-$ pairs and to minimize the energy loss of particles before they get to the calorimeter.

The vertex chamber [12] consists of three mechanically independent layers

of drift cells with. The outer two layers of the chamber are broken into 32 azimuthal sectors, whereas the inner layer consists of 16 sectors in azimuth. The wires in each layer are supported by G-10 bulkheads mounted on either side of the carbon fiber tube defining its inner radius. Each sector consists of eight sense wires which are read out on both ends to measure $z$ position using charge division. The sense wires are staggered $\pm 100$ $\mu$m relative to the sector centerline to resolve left-right ambiguity. A spatial resolution of $60\mu$m for drift distances greater than 2mm was measured for the vertex detector [13]. The track pair resolution efficiency was measured to be better than 90% for separations greater than 0.63mm [13].

### 2.1.2 Transition radiation detector (TRD)

The transition radiation detector uses the property that charged particles radiate photons (X-rays for highly relativistic, $\gamma = 1/\sqrt{1-(v/c)^2} > 10^3$, charged particles) when crossing the boundary of two materials with different dielectric or magnetic properties. The energy of such radiated photons can be made to depend linearly on the *Lorentz* $\gamma$ factor. The energy is inversely proportional to the square root of the mass of the charged particle crossing the media. Thus, the transition radiation detector can be a good tool in separating hadrons (strongly interacting particles) from electrons.

Since the DØ detector does not have a central magnetic field, it was anticipated that many fake electrons from jets would be observed composed of neutral hadrons which decay to photons with an overlapping low energy

| Drift Chamber | VTX | CDC |
|---|---|---|
| Maximum Length (cm) | 116.8 | 179.4 |
| Number of layers | 3 | 4 |
| Phi sectors/layer | 16,32,32 | 32 |
| Sense wires/sector | 8 | 7 |
| Total number of sense wires | 640 | 903 |
| Number of alternate readout channels | 832 | 256 |
| Sense wire stagger ($\mu$m) | 100 | 200 |
| Maximum drift distance (mm) | 13.7 | 70.8 |
| Gas mixture | $CO_2/C_2H_4$ | $Ar/CH_4/CO_2$ |
| Pressure of gas (atm) | 1 | 1 |
| Drift Velocity ($\mu$m/nsec) | 8 | 34 |
| Sense wire resolution ($\mu$m) | 60 | 200 |
| Charge division resolution (cm) | $\pm 1^a$ | - |
| Alternate readout resolution (mm) | - | 20 |
| Pair resolution (mm) | 7 | 10 |

Table 2.1: Characteristics of vertex and central drift chamber

[a]Design spec.

charged hadron. The transition radiation detector was built by DØ to compensate for the lack of a central magnetic field in separating electrons from this background.

The TRD surrounds the vertex detector concentrically along the beam pipe. The total collected charge on anode wires can be used to distinguish electrons from hadrons. This detector system was tested at a test beam at $CERN$ and shown to have an $e/\pi$ rejection factor of 30 while retaining 90% of the electrons [14]. Therefore, the TRD can play a key roll in discriminating

electrons from its backgrounds.

### 2.1.3 Drift chambers (CDC and FDC)

A drift chamber is a tracking device which uses the drift time of ionization electrons from gas molecules liberated by the traversing charged particle to measure the trajectory of the ionizing particle. The DØ detector has three drift chambers other than the vertex chamber. The central region (approximately $| \eta | < 1.2$) is covered by the central drift chamber. The range of pseudorapidity $| \eta | > 1.4$ is covered by two forward drift chambers one on either side of the CDC. The drift chambers are not subject to any magnetic fields. The CDC forms a concentric ring around the TRD providing a good pointer to central calorimeter energy clusters. The spatial resolutions measured at Fermilab's test beam facility were 2mm along the length of the detector ($z$) and 150$\mu$m in the $r\phi$ plane. [15]. The CDC consists of four layers which are staggered by half the size of a sector relative to each other so that no crack in the $\phi$ direction is aligned. Each layer consists of 32 sectors each of which has 8 sense wires providing information for determining polar ($\theta$) and azimuthal angle ($\phi$) of a track and 2 delay lines providing $z$ information.

Located on either side of the central drift chamber are the forward drift chambers (FDC). These FDC's were tested at Fermilab's test beam facility and were shown to have a spatial resolution of 200$\mu$m in the $r\phi$ plane [16]. The FDC's have three layers of chambers. A $\Phi$ chamber with wires running radially is sandwiched between two $\Theta$ chambers. The $\Phi$ chamber provides

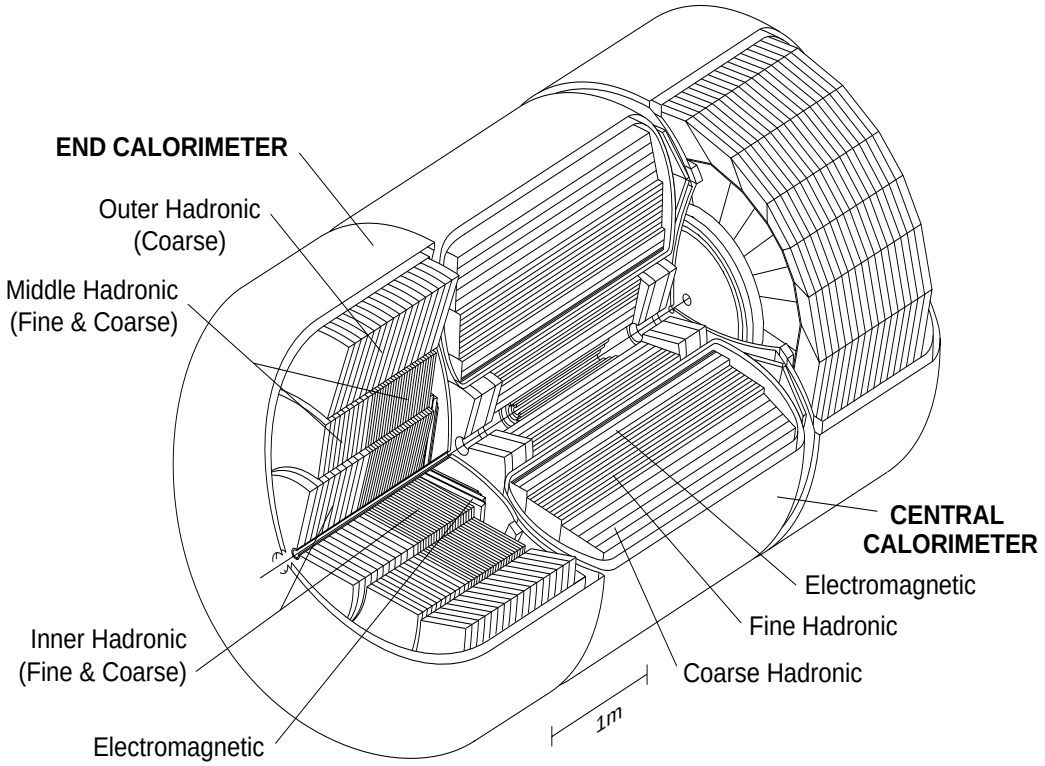


Figure 2.3: A cut away view of the DØ calorimeter system.

information in azimuthal direction and the Θ chambers provide information in polar angle of the charged track. These layers are staggered in the $r\phi$ plane so that no cracks are aligned. The staggering of the wires reduces the ambiguity in identifying tracks from ghost hits (mirror images on either side of sense wires).

## 2.2 The DØ calorimeter system

There are two basic types of calorimeters used to measure the energy of a particle. One is a total absorption calorimeter. As a particle traverses this

type of calorimeter, the particle loses all of its energy in the material and all the energy lost by the particle is seen by the detector. The second type of calorimeter is a sampling calorimeter. A sampling calorimeter samples only a part of the energy lost by a particle. A correction has to be made to convert the fraction of the energy measured to the full energy lost by the particle. This conversion factor is called the sampling fraction. A sampling calorimeter is normally composed of a dense absorbing material and a less dense active material. In the less dense material ionization charge is produced by the particles in the shower traversing through the material. Showers of particles are mostly produced in the absorbing material where most of the initial particle's energy is lost. Calorimeters are designed to produce electronic signals proportional to the deposited energy.

The DØ calorimeters, shown in Fig. 2.3, are sampling calorimeters. The absorber materials used in the DØ calorimeters are uranium, copper, and stainless steel. The active medium is liquid argon ($LAr$). The basic structure, shown in Fig. 2.4, of the DØ calorimeter is an absorber material between two 2.3mm LAr gaps on either side of a 1.3mm thick G10 board. The G10 boards have copper pads inside and are covered with a resistive coating on their outer surfaces. The energy of particles traversing the detector is measured by collecting the charge deposited in $LAr$ gaps. The shower of particles from the interaction of the primary particle ionize the $LAr$. The electrons liberated from the $LAr$ drift across the gap because an electric field is applied between the absorber and the resistive coat. The current induces a charge on the copper pads. The current needed to supply this charge to the pad is provided

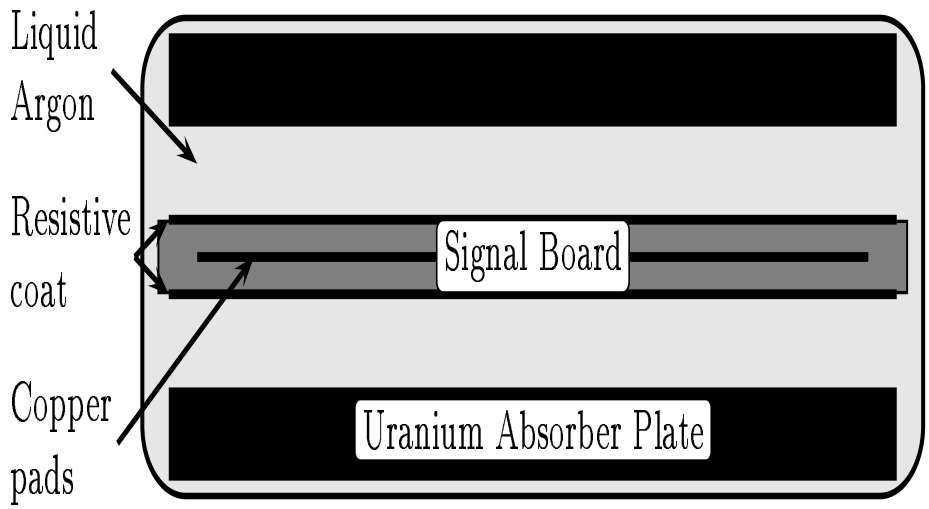


Figure 2.4: A unit cell structure of the DØ calorimeter.

and measured by preamplifiers. The strength of the applied field is $8.7kV/cm$ under normal operating conditions.

In the following two subsections the DØ calorimeter system will be discussed in more detail. More intensive description of the calorimeter construction and characteristics can be found from Refs. [17] and [18].

### 2.2.1 Central calorimeter (CC)

The central calorimeter covers the central portion of the detector, roughly $| \eta | < 1.2$. The CC is subdivided into three different subsystems. From innermost to outer-most they are the electromagnetic calorimeter, the fine hadronic calorimeter, and the coarse hadronic calorimeter.

The lateral segmentation of the calorimeters is $0.1 \times 0.1$ in $\eta - \phi$ space at

all longitudinal depths except the third readout layer of the electromagnetic calorimeter. The segmentation of this layer is $0.05 \times 0.05$ in $\eta - \phi$ space in order to optimize the position resolution at the shower maximum for electrons and photons [17] [18]. Table 2.2 summarizes characteristics of the CC.

### CC Electromagnetic (EM) calorimeter

The central most calorimeter of the CC is the electromagnetic calorimeter. Its main purpose is the energy measurement of electromagnetic particles like electrons and photons. This portion forms a cylinder around the beam direction. The detector uses depleted uranium as the absorbing material. In general, the mean free path of electromagnetic particles is expressed in the units of radiation lengths ($X_0$). The electromagnetic calorimeter has a total of $20.5X_0$. The fraction the energy of electromagnetic particles left after traversing a depth, $x$, of material is expressed as;

$$P(x) = e^{\frac{-x}{X_0}} \tag{2.1}$$

The longitudinal depth of the CCEM contains 97% of most showers induced from EM particles. More details can be found in table 2.2.

The resolution of a sampling calorimeter [19] is typically expressed as follows:

$$(\frac{\sigma}{E})^2 = C^2 + \frac{S^2}{E} + \frac{N^2}{E^2} \tag{2.2}$$

where $E$ is the mean energy of the incident particle, $C$ is a constant term which reflects calibration errors such as momentum error variation of the test

| Central Calorimeter | EM | FH | CH |
|---|---|---|---|
| Number of modules | 32 | 16 | 16 |
| Absorber [a] | Uranium | Uranium | Copper |
| Absorber Thickness (cm) | 0.3 | 0.6 | 4.65 |
| Argon gap (cm) | 0.23 | 0.23 | 0.23 |
| Number of signal boards/module | 21 | 50 | 9 |
| Longitudinal depth | 20.5 $X_0$ | 3.2 $\Lambda$ | 3.2 $\Lambda$ |
| Number of readout layers | 4 | 3 | 1 |
| Number of signal boards/readout depth | 2,2,7,10 | 21,16,13 | 9 |
| Total $X_0$ [b] | 20.5 | 96.0 | 32.9 |
| Total $\Lambda$ [c] | 0.76 | 3.2 | 3.2 |
| Sampling fraction (%) | 11.79 | 6.79 | 1.45 |
| Readout segmentations ($\Delta\phi \times \Delta\eta$) [d] | $0.1 \times 0.1$ | $0.1 \times 0.1$ | $0.1 \times 0.1$ |
| Total number of readout cells | 10368 | 3000 | 1224 |
| Maximum pseudorapidity coverage | $\pm 1.2$ | $\pm 1.0$ | $\pm 0.6$ |

Table 2.2: Central Calorimeter characteristics

[17] [18]

[a] Uranium absorbers are depleted. FH absorbers are Uranium and 1.7% of Niobium alloy

[b] Total radiation length at $\eta = 0$

[c] Total interaction length at $\eta = 0$

[d] The third layer of the EM calorimeter is $0.05 \times 0.05$ in $\eta - \phi$ space.

beam and thickness variation of the $LAr$ gaps, $S$ is the sampling fluctuation term due to the fluctuations of showers in the $LAr$ gaps and $N$ is the noise term including both electronic noise and noise induced by the radioactivity of the absorber. The energy resolution of CCEM has been measured at the DØ test beam. The measured values for the CCEM are $C = 0.003 \pm 0.004$, $S = (0.162 \pm 0.011)\sqrt{GeV}$ and $N = 0.140GeV$ for electrons [20].

### CC Fine hadronic (FH) calorimeter

The fine hadronic calorimeter is designed to collect energy deposited by more penetrating particles such as pions. The CCFH forms a cylindrical ring around the EM calorimeter so both CCFH and CCEM are concentric about the beam direction. The CCFH ring is composed of 16 CCFH modules covering $2\pi$ in $\phi$. In general, hadronic particles interact differently in material than EM particles. Nuclear interactions are the major type of interactions through which hadronic particles lose their energy. The fraction of hadrons not undergoing nuclear interaction after a certain depth, $x$, of material is expressed:

$$P(x) = e^{\frac{-x}{\Lambda}} \tag{2.3}$$

where $\Lambda$, the interaction length, is the mean free path of a hadron in matter. Since the CCFH follows the CCEM calorimeter which is approximately $0.76\Lambda$, approximately 53% of hadrons start showering before they enter the first layer of the CCFH. More detailed information on the CCFH can be found in table 2.2.

#### CC Coarse hadronic (CH) calorimeter

Since hadronic showers show large fluctuations in the depth of interaction, the DØ calorimeter system has additional calorimetry to provide leakage coverage. In the central region, the CCCH forms a cylinder just outside of the CCFH so that all three calorimeters are concentric around the direction of beam. The CCCH ring consists of 16 modules staggered with the CCFH so no longitudinal cracks between the two rings are aligned. The absorber material of the CCCH consist of nine $4.75cm$ thick copper plates totaling approximately $3.2\Lambda$ at $\eta = 0$.

### 2.2.2 End calorimeter (EC)

The end calorimeters (EC) cover the pseudorapidity range $1.1 <| \eta |< 4.5$ The EC's consist of four different types of modules. The ECEM is located on the front face of the EC nearest to the interaction region. The ECIH is located immediately behind the ECEM. Sixteen ECMH modules surround the ECIH concentrically. Sixteen ECOH modules form a concentric ring just outside of the ECMH.

#### EC electromagnetic calorimeter

The ECEM module has a diameter of approximately $2m$ and a total thickness of $24.1cm$. In the DØ detector, ECEM is positioned with its front face $1.70m$ away from the nominal interaction point. The absorber material used in the ECEM is 4mm thick depleted uranium and the active medium is $LAr$. The

| End Calorimeter | EM | IFH | ICH | MFH | MCH | OH |
|---|---|---|---|---|---|---|
| Number of modules | 1 | 1 | 1 | 16 | 16 | 16 |
| Absorber [a] | U | U | SS [b] | U | SS | SS |
| Absorber Thickness (cm) | 0.4 | 0.6 | 0.6 | 0.6 | 4.65 | 4.65 |
| Liquid Argon gap (cm) | 0.23 | 0.21 | 0.21 | 0.22 | 0.22 | 0.22 |
| $N_{signal-boards}$/module | 18 | 64 | 12 | 60 | 14 | 24 |
| Longitudinal depth | $20.5X_0$ | $4.4\Lambda$ | $4.1\Lambda$ | $3.6\Lambda$ | $4.4\Lambda$ | $4.4\Lambda$ |
| Number of readout layers | 4 | 4 | 1 | 4 | 1 | 3 |
| $N_{signal-boards}$/readout depth | 2,2,6,8 | 16 | 14 | 15 | 12 | 8 |
| Total $X_0$ | 20.5 | 121.84 | 32.78 | 115.5 | 37.95 | 65.07 |
| Total $\Lambda$ | 0.949 | 4.91 | 3.57 | 4.05 | 4.08 | 7.01 |
| Sampling fraction (%) | 11.9 | 5.66 | 1.53 | 6.68 | 1.64 | 1.64 |
| Cell size in $\eta$ [c] | 0.1 [d] | 0.1 | 0.1 | 0.1 | 0.1 | 0.1 |
| Cell size in $\phi$ | 0.1 | 0.1 | 0.1 | 0.1 | 0.1 | 0.1 |
| Minimum rapidity covered | $\pm 1.4$ | $\pm 1.6$ | $\pm 2.0$ | $\pm 1.0$ | $\pm 1.3$ | $\pm 0.7$ |
| Maximum rapidity covered | $\pm 4.0$ | $\pm 4.45$ | $\pm 4.45$ | $\pm 1.7$ | $\pm 1.9$ | $\pm 1.4$ |
| Total number of channels | 7488 | 5900[e] | | 1664 [f] | | 960 |

Table 2.3: End Calorimeter characteristics

[17] [18]

[a] Uranium(U) absorbers are depleted. IFH and MFH absorbers are Uranium and 1.7% Niobium alloy

[b] SS is stainless steel

[c] $\Delta\phi \times \Delta\eta = 0.2 \times 0.2$ in the region of $\eta \geq 3.2$

[d] The third layer of EM calorimeter is segmented $0.05 \times 0.05$ in $\eta - \phi$ space

[e] The sum of the number of the IH readout channels

[f] The sum of the number of the MH readout channels

pseudorapidity coverage of the ECEM is $\pm 1.4$ to $\pm 4.0$ in rapidity units providing hermetic coverage of the EM calorimeter down to the beam pipe. The relative energy resolution of the ECEM as a function of energy was measured in the 1989 DØ test beam. The parameters in the resolution function (Eq. 2.2) are $C = 0.003 \pm 0.003$, $S = (0.157 \pm 0.006)\sqrt{GeV}$ and $N = (0.29 \pm 0.03)GeV$ [21]. The spatial resolution was also determined using 50 $GeV$ electrons by comparing the test beam track and energy weighted position of the shower solely in layer 3 of the ECEM. This resolution can be parameterized as:

$$\sigma(mm) = 1.0 + 0.035x^2 \tag{2.4}$$

where x is the distance of the impact position in layer 3 from the edge of a tower in the units of mm. The ECEM position resolution varies approximately as $\sqrt{E}$ [21]. More ECEM characteristics can be found in table 2.3.

**EC inner hadronic (IH) calorimeter**

The inner hadronic calorimeter is a cylinder shaped module following the ECEM with inner and outer radii of 3.92 and 86.4cm. The IH consists of two different detectors: fine and coarse hadronic (IFH and ICH). The fine hadronic portion consists of 4 readout layers, each containing sixteen 6 mm thick uranium-niobium(1.7%) alloy plates as absorber. The leakage calorimeter (ICH) consists of thirteen 46.5 mm thick stainless steel plates as absorber. The ICH has only one readout layer. The pseudorapidity coverage of the ECIH is $1.6 < |\eta| < 4.5$. Table 2.3 shows more characteristics of the ECIH module.

### EC middle hadronic (MH) calorimeter

Around the inner hadronic calorimeter, concentric to the beam pipe, is the middle hadronic calorimeter ring consisting of sixteen modules. The MH has two different portions. The first 4 readout layers of the MH form the middle fine hadronic (MFH) and the last one depth forms the middle coarse hadronic (MCH). The MFH modules have 6 mm thick uranium-niobium(2%) alloy as absorber material and the MCH modules have 46.5mm thick stainless steel plates as absorber. The pseudorapidity coverage of the ECMH is $1.1 <| \eta |< 2.0$.

The energy resolution has been measured in the 1987 DØ test beam using 25 to 150 GeV electrons and pions. The parameters in the resolution function are $C = (0.010 \pm 0.004)$, $S = 0.233 \pm 0.010\sqrt{GeV}$, and $N = 1.22$GeV for electrons, and $C = (0.047 \pm 0.005)\sqrt{GeV}$, $S = 0.439 \pm 0.042\sqrt{GeV}$, and $N = 1.28$GeV for pions[20].

### EC outer hadronic (OH) calorimeter

The ECOH ring consists of 16 modules surrounding the ECMH ring concentrically. The ECOH covers the pseudorapidity $0.7 <| \eta |< 1.4$. The absorber of this calorimeter is 46.5 mm thick stainless steel plates inclined at an angle of 60° with respect to the beam axis. This calorimeter provides leakage coverage for hadron showers as CCCH does. The characteristics of the ECOH modules are summarized in table 2.3.

### 2.2.3 Massless gaps and the ICD

The region $0.8<|\ \eta\ |<1.4$ in the DØ calorimeter contains considerable amount of uninstrumented material. The energy lost in this region is not detected. To correct for the energy loss in the uninstrumented region, the DØ detector calorimeter system adopted two different type of detectors. One is an array of scintillation counter tiles called the intercryostat detector (ICD). An array of ICD modules is mounted on the front surface of each EC cryostat. Each ICD array consists of 384 scintillator tiles of size $0.1 \times 0.1$ in $\eta - \phi$ space. These tiles are the same size as the calorimeter cells and form a pseudo-projective structure with the calorimeter cells. The ICD readout uses phototubes.

In addition to the ICD, massless gap modules are mounted on the surfaces of the CCFH, ECMH, and ECOH modules. These modules consist of two signal boards surrounded by three $LAr$ gaps. The size of the readout cells of the massless gaps is $0.1 \times 0.1$ in $\eta - \phi$ space [17] [18]. The massless gaps reside inside the calorimeter cryostats.

## 2.3 The muon system

The DØ muon detection system consists of five separate solid-iron toroidal magnets surrounded by proportional drift chambers. These measure charged particle track trajectories down to approximately 3 degrees from the beam pipe. This system enables DØ to identify muons and measure their trajectories and momenta. Muon momenta are measured using the bend angle determined

| | |
|---|---|
| Magnetic field strength | 2 T |
| Magnetic kick (90°) | 0.61 GeV/c |
| System precision goal in bend plane | 500 $\mu$m (Diffusion limit, 200 $\mu$m) |
| System precision goal in non-bend plane | 2-3 mm (charge ratio, $\pm$1.0%) |
| $\delta p/p$ (multiple scattering limit)[a] | 18% |
| $3\sigma$ sign determination ($\theta, \phi$ 90°,0°) | $P_t \leq$350 GeV/c |
| Interaction lengths (90°) | 13.4 |
| Interaction lengths (5°) | 18.7 |
| Drift-coordinate resolution | $\pm$0.45 mm |

Table 2.4: Design parameters of the DØ muon system

[a] Absolute theoretical limit assuming 100% chamber efficiency.

between the trajectories before and after the magnets. The strength of the fields is approximately 2 Tesla. The incident trajectory is determined from the primary interaction point, central tracking, and the first layer of muon chamber. Multiple Coulomb scattering in the calorimeters and iron toroids limits the relative momentum resolution to $\geq$ 18%. The precision of defining position and angle is $\pm$0.3mm and $\pm$0.6mrad [18], respectively, for the first muon chamber. The expected precision in determining the angle and position of the outgoing particle from the iron measured in the subsequent two layers of the PDT's are $\pm$0.2mrad and $\pm$0.17mm respectively [22]. Table 2.4 summarizes the design parameters of the muon system.

## 2.4 Trigger and Data Acquisition system

There are three different trigger levels in DØ. These control the data rate from the detector as well as filter the data written to tape. The level 0 scintillator-based trigger indicates the occurrence of an inelastic collision. The level 1 trigger is a collection of hardware trigger elements arranged in a flexible and easily modified software-driven architecture. The level 1 trigger is based on the transverse energy in the calorimeter and aligned hits in the muon system. Most level 1 triggers operate within the 3.5 $\mu$s time interval between bunch crossings. Others, however, require several bunch crossing interval to complete computations and are referred to as Level 1.5 triggers. Once an event is passed by the Level 1 or Level 1.5 trigger, it is sent through the standard DØ data acquisition pathway to a farm of microprocessors which serve as event builders as well as the Level 2 software trigger system. The Level 2 triggers use sophisticated algorithms to reduce the event rate before passing events to the host computers for event monitoring and recording. Figure 2.5 shows a block diagram of the trigger and data acquisition system.

### 2.4.1 Level 0

The Level 0 consists of two scintillator hodoscopes. Each is mounted on the front surfaces of the opposing EC cryostats (perpendicular to the beam direction). These hodoscopes have two planes of scintillation counters rotated by 90°. Each hodocope has 20 short ($7cm \times 7cm$) scintillation elements readout

by single photomultiplier tube and 8 long ($7cm \times 65cm$) elements each readout by 2 photomultipliers. These hodocopes give partial coverage for the pseudorapidity range $1.9 <| \eta |< 4.3$ and nearly complete coverage over $2.2 <| \eta |< 3.9$. The time of flight resolution of the hodocopes is less than 150ps [18].

The Level 0 trigger [24] registers the presence of inelastic collisions by detecting low angle particles produced in the interaction region. By measuring the arrival time difference between these low angle particles, the Level 0 can determine the $z$ position of the interaction. The Level 0 also serves as a luminosity monitoring device and identifies multiple interactions.

### 2.4.2 Hardware trigger (The Level 1)

The Level 1 trigger framework [25] [26] [27] gathers digital information from the Level 0, calorimeter, and muon systems. A decision has to be made before the next beam crossing ($3.5\mu$sec) by the Level 1 as to whether a particular event is to be kept for further examination. A total of 32 possible triggers are available. Each is the logical combination of 256 programmable input terms. The input terms can be beam quality conditions provided by the Level 0 (the vertex positions, etc), the number of coarse muon candidates, transverse energy above threshold from the calorimeter Level 1 processor, etc. The calorimeter trigger extends to $| \eta |=3.2$ in trigger towers of $0.2 \times 0.2$ in $\eta - \phi$ space. These trigger towers are further divided longitudinally into electromagnetic trigger towers and hadronic trigger towers. Events are selected

as events with electron candidates if the $EM$ section of a single trigger tower exceeds one of four given transverse energy thresholds. On the other hand, events are selected as events with jet candidates if the sum of the $EM$ and hadronic trigger towers exceeds various thresholds. Scalar $E_T$ and missing $E_T$ are computed from the vector sum of $E_T$ of all towers.

### 2.4.3 Software triggers (The Level 2)

The Level 2 trigger system is based upon a farm of 48 micro-VAX 4000-M60s [28]. The main purpose of the Level 2 is to collect the digitized data from all relevant detector elements for events that successfully pass the Level 1 triggers. If a Level 1 trigger bit is satisfied, a specified sequence of "filter tools" examine the event. Specific tools or algorithms exist for electrons, photons, jets, muons, $\tau$'s, scalar $E_T$, and $\not\!\!E_T$ . The rejection factor at this level of the trigger is governed by the bandwidth of the data acquisition system. More sophisticated tools exist for jet topologies with restricted $\eta$ ranges. A total of 128 programmable filter conditions are available for specific physics interests. If an event passes a filter, the data is transfered to the host computers for logging. The designed maximum input rates to the Level 2 system is $200Hz$. The output from the Level 2 trigger is limited to 1-2$Hz$.

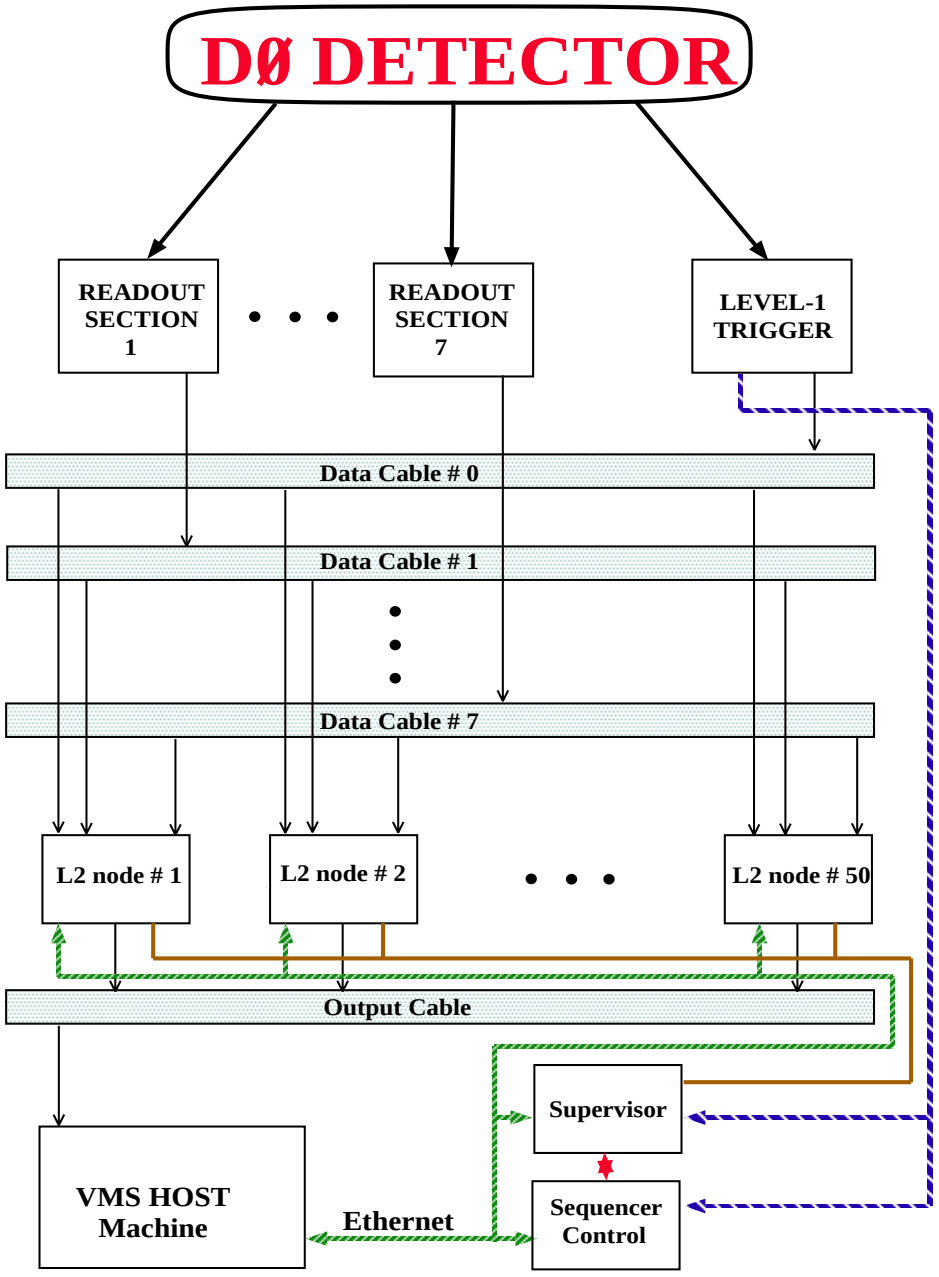


Figure 2.5: A block diagram of the DØ trigger and data acquisition system

# Chapter 3

# Data sample

The data used in this analysis corresponds to an integrated luminosity of $(14.3 \pm 1.7) pb^{-1}$ collected from August 1992 to May 1993. During this collider run period, the hardware triggers were active for $\mid \eta \mid < 3.2$.

## 3.1 Triggers

The trigger used in this analysis required a combination of an $EM$ candidate at Level 1 and a high $E_T$ electron candidate with missing $E_T$ at Level 2. The algorithms, electron $E_T$ thresholds, and $\not\!\!E_T$ thresholds are discussed in more detail in the following sections.

### 3.1.1 Level 1

The Level 1 trigger required at least one $EM$ candidate above a threshold transverse energy. This threshold changed during the 1992 collider run. One of the main purposes of the Level 1 trigger was to regulate the data flow rate

| Trigger Version | Threshold (GeV) | Run range | $\int Ldt(nb^{-1})$ |
|---|---|---|---|
| | 14 | 50226-50732 | $< 50$ |
| 5.2 | 14 | 50733-51283 | $< 50$ |
| 5.3 | 14 | 51284-51422 | $< 20$ |
| 5.4 | 14 | 51423-53752 | 296 |
| 5.5 | 14 | 53761-54963 | 404 |
| 6.0 | 14 | 54965-55200 | 297 |
| 6.1 | 14 | 55217-55600 | 100 |
| 6.2 | 14 | 55601-56297 | 626 |
| 6.3 | 12 | 56298-57711 | 2192 |
| 6.4 | 10 | 57712-58141 | 414 |
| 6.5 | 10 | 58142-59378 | 2214 |
| 7.0 | 10 | 59390-59443 | 178 |
| 7.1 | 10 | 60100-62149 | 2047 |
| 7.2 | 10 | 62150-64085 | 4615 |
| 7.3 | 10 | 64086-65879 | 1477 |

Table 3.1: History of the Level 1 trigger

into the Level 2 to avoid increasing dead time while providing a background rejection factor of approximately 500. As the bandwidth capabilities increased early in the run due to hardware and software improvement, the threshold was lowered to ensure a full efficiency at low offline threshold for other Level 2 triggers. Since the Level 1 computes $E_T$ relative to the nominal interaction point ($z$=0) the resolution is worse than that in offline. Therefore, it was necessary to lower the threshold in the Level 1. Table 3.1 shows the history of the thresholds used for the Level 1 trigger with the corresponding run numbers and integrated luminosities. This continuous change did not affect this analysis because the offline threshold was well above the threshold set by the trigger and was fully efficient. The offline thresholds were set to ensure a full efficiency based on the studies of the Level 1 trigger efficiencies [29].

### 3.1.2 Level 2

The software trigger used in this analysis required an electron candidate above a 20 GeV $E_T$ together with missing $E_T$ greater than 20 GeV. This Level 2 trigger is called $ELE - MAX$. The algorithms used in the trigger are discussed in the following sections. The combined Level 1 and Level 2 trigger efficiency including the detector geometric acceptance from a Monte Carlo study is 63%$\pm$2% [30]. These conditions for $ELE - MAX$ were stable throughout the run.

### The Level 2 Electron algorithm

The Level 2 electron algorithm [31] works in the following order:

- Find $EM$ candidate(s) tagged by the Level 1 trigger.
- Find the most energetic EM readout layer 3 cell, "peak" cell, within each Level 1 candidate EM tower above threshold.
- Calculate the $E_T$ in each EM layer in a $3 \times 3$ ($\Delta\eta \times \Delta\phi = 0.3 \times 0.3$) tower surrounding the peak cell for each candidates independent of the $\eta$.
- Within the EM layer 3 cells calculate the transverse shape variables (e.g, difference in the summed energy in $\Delta\eta \times \Delta\phi = 0.25 \times 0.25$ and $\Delta\eta \times \Delta\phi = 0.15 \times 0.15$ in EM layer 3 cells).
- Apply cuts on vertex corrected $E_T(> 20GeV)$. The vertex correction is done based on the vertex $z$ information from the Level 0 detector.
- Apply shower shape cuts on longitudinal layer energy fraction ($\frac{E_{EH1}}{EM_{tot}} <$ 0.1 and $0.1 < \frac{E_{EM3}}{EM_{tot}} < 0.9$).
- Apply cuts on transverse shower shape variables.
- Isolation fraction less than 0.15. The isolation fraction is defined as:

$$ISO_{L2} = \frac{E^{total}_{\Delta R=0.4} - E^{EM}_{3\times3}}{E^{EM}_{3\times3}} \tag{3.1}$$

where $E^{total}_{\Delta R=0.4}$ is the total energy summed over all layers inside of cone of radius 0.4, $E^{EM}_{3\times3}$ is the electromagnetic energy inside of $3\times3$ ($\Delta\eta\times\Delta\phi = 0.3\times0.3$) window about the peak tower.

- One of the available tools in the Level 2 is finding a matched track in the central tracking detectors and the calorimeter cluster. This option was not used for $ELE-MAX$.

### The Level 2 Missing $E_T$ algorithm

The missing $E_T$ in the Level 2 [32] is computed as follows:

$$E_x = \sum_{\eta,\phi,l} E_T(\eta,\phi,l) e_t corr(\eta) cos\phi \tag{3.2}$$

$$E_y = \sum_{\eta,\phi,l} E_T(\eta,\phi,l) e_t corr(\eta) sin\phi \tag{3.3}$$

$$\not\!\!E_T = \sqrt{E_x^2 + E_y^2} \tag{3.4}$$

$$\phi_{\not\!\!E_T} = tan^{-1}(-E_y/-E_x) \tag{3.5}$$

where $\eta$,$\phi$,$l$ are the channel addresses, $E_T(\eta,\phi,l)$ is the nominal $E_T$ computed assuming a vertex at $z = 0$ for the channel without any corrections (e.g. gain corrections, zero suppression, pedestal subtractions, etc.), $e_t corr(\eta)$ is the vertex $z$ position correction factor defined as:

$$e_t corr(\eta) = \sqrt{\frac{X^2_{cell} + Y^2_{cell} + Z^2_{cell}}{X^2_{cell} + Y^2_{cell} + (Z_{vertex} - Z_{cell})^2}} \tag{3.6}$$

where $X_{cell}$, $Y_{cell}$, $Z_{cell}$ are the $X$,$Y$,$Z$ coordinates of the channel, and $Z_{vertex}$ is the $Z$ position of the vertex as determined by the Level 0 trigger. This vertex correction is necessary because the $E_T$ is computed based on the measured

energy in the calorimeter cell and the polar angle ($\theta$) from the beam axis. Since the vertex $z$ position computed using the Level 0 detector is not as accurate as that determined from the central tracking system, the $\not\!\!E_T$ in the Level 2 is only an approximate computation of the real $\not\!\!E_T$ in the event. The $\not\!\!E_T$ was required to be greater than 20 GeV.

## 3.2 Particle identification

In studying high energy physics the interpretation of collected data is important. This interpretation process is called reconstruction or pattern recognition. Particles produce characteristic signals in the detector. These patterns can be identified with a particular type of particle although there is always some uncertainty in this identification. Some particle types are electrons, muons, photons, and taus. Jets, collections of strongly interacting particles near one another, also produce a characteristic pattern. Other quantities of interest are the event vertex, scalar $E_T$, and $\not\!\!E_T$ . The DØ reconstruction program is designed to recognize the characteristic patterns and assigns the following identities and quantities: interaction vertex, electrons, muons, photons, taus, jets, scalar $E_T$ and $\not\!\!E_T$ . The reconstruction algorithms for these particles and quantities are discussed in the following subsections.

### 3.2.1 Interaction Vertex

The identification of a vertex from a hard interaction is very important in determining transverse energy ($E_T$) of objects in the event because the

definition of $E_T$ relies on the polar angle determined by the vertex and the direction of the object relative to the beam axis. In general, the $E_T$ of an object in a collider experiment is defined as:

$$E_T^{object} = E^{object} sin\theta \tag{3.7}$$

where $E^{object}$ is the measured energy of the object in the calorimeter and $\theta$ is the polar angle.

The DØ reconstruction algorithm uses the central tracking information to determine the vertex position. The drift chambers are the main devices for the vertex determination. The procedure is as follows:

- Find well aligned hits in the drift chambers and reconstruct the tracks in $r\phi$ plane.
- Reconstruct tracks in $rz$ plane based on the tracks reconstructed in $r\phi$ plane.
- The distribution of the $z$ position of the extrapolated tracks is constructed from the the projection of each the reconstructed track onto the beam axis.
- Clusters of tracks associated with one or more vertices is then identified. A Gaussian fit to each cluster yields the $z$ position of each vertex. The deviation of the fit represents the uncertainty.

The resolution of the vertex position is measured to be 0.65 cm to 0.95 cm in $z$ direction depending on the number of reconstructed tracks associated with the

vertex and the angular distributions of the contributing reconstructed tracks. The vertices are well identified against each other when they are separated by more than 7cm.

### 3.2.2 Electrons and photons

Electrons are relatively well defined objects in the detector, especially those electrons from the decay of $W$ vector bosons which have high $P_T$ and are well isolated from the other objects in the event. This particular property of electrons from $W$ decay makes event selection simple and well defined. In DØ particle identification photons are defined exactly the same as electrons except the matching track requirements.

The main clustering algorithm used to define an electron/photon is the nearest neighbor algorithm. The nearest neighbor algorithm forms a cluster by looping through EM towers ordered in $E_T$. The algorithm looks for the highest $E_T$ EM tower and relates other towers nearest to the tower into a cluster. These towers related with the highest $E_T$ tower are then summed into a cluster. The summing continues until there are no towers above a transverse energy threshold or until a limit in the number of towers is reached.

After clustering, the DØ reconstruction algorithm for electron-like (photon-like) objects proceeds as follows:

- An energy cluster is required to have at least 90% of its total energy deposited in the EM section. The total energy of the cluster is defined as the total sum of all the calorimeter cells (EM+HAD) within the size

of the cluster formed by the above algorithm. This simple cut is found to be more than 99% efficient for DØ test beam electrons with energies between 10 to 150 $GeV$.

- For electrons, there must be at least one matching CDC or FDC track pointing to the calorimeter cluster within a road of 0.1 ($2\pi/64$ radian) in $\phi$ and 0.1 radian in $\theta$. The size of the road may vary depending on the uncertainty in the vertex position. This condition is used to distinguish electrons from photons.

- The fraction of energy outside of the central tower of the cluster must be less than 60%.

There are additional tools available to increase the discriminating power of the electron (photon) selection over the backgrounds. These tools are explained below. At this stage of identifying an electron-like (photon-like) object, these tools are not used but the quantities are computed so that they can be used for further selection of data samples and background rejection.

To obtain the best discrimination against hadrons, DØ electron (photon) identification uses a covariance matrix technique which takes into account correlations between energy depositions in the calorimeter cells based on the longitudinal and transverse shower shapes of typical electrons. Given a sample of $N$ electrons (photons) one can define the covariance matrix:

$$M_{ij} = \frac{1}{N}\sum_{n=1}^{N}(x_i^n - \langle x_i \rangle)(x_j^n - \langle x_j \rangle), \tag{3.8}$$

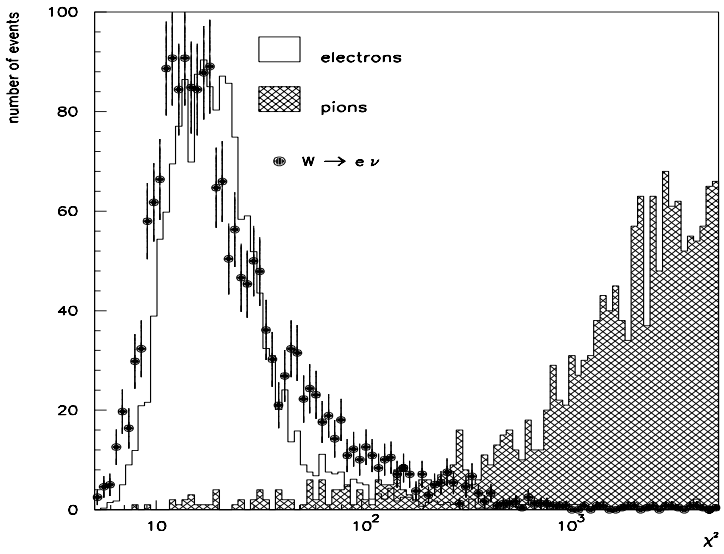


Figure 3.1: $\chi^2$ distributions of electrons (unshaded), pions (shaded), and electrons from the $W$

where $x_i^n$ is the value of observable $i$ for electron $n$ and $\langle x_i \rangle$ is the mean value of observable $i$ for the sample. If $H = M^{-1}$, one can determine whether a shower $k$ is electromagnetic by computing the covariance parameter defined as:

$$\chi^2 = \sum_{i,j} (x_i^k - \langle x_i \rangle) H_{ij} (x_j^k - \langle x_j \rangle). \tag{3.9}$$

By placing a cut on $\chi^2$ one can separate EM and hadronic showers. More detailed explanation of covariant matrix (H-matrix) algorithm can be found in Ref. [33] and [34].

Figure 3.1 [35] shows the distributions of $\chi^2$ for showers from test beam electrons and pions with an energy of $25 GeV$. The hatched area of histograms illustrates the $\chi^2$ distributions of pions. The two distributions are well separated. The data points are the distribution of electrons from $W$ vector boson

decays from the collider data which are identified using a missing transverse energy ($\not\!\!E_T > 20$ GeV), transverse energy of electron ($E_T$ >20 GeV), missing $E_T$ significance ($\sigma_{\not\!\!E_T} = \frac{\not\!\!E_T}{1.2+0.023\sum E_T} > 5$) , and no jet activity in the event. As one can see from the distributions, the electrons from the $W$ decay agree well with the distributions from the electrons in the test beam. In general, the variables defining the matrix are not normally distributed, therefore the covariance parameter $\chi^2$ does not necessarily follow a normal $\chi^2$ distribution [34].

The calorimeter position resolution is important for matching tracks in the tracking system to clusters in the calorimeter. DØ electron identification computes the shower centroid ($\vec{x}_{cog}$) using a weighted center of gravity method [36] defined as follows:

$$\vec{x}_{cog} = \frac{\sum_i w_i x_i}{\sum_i w_i}, w_i = max[0, (w_0 + ln\frac{E_i}{E_{tot}})] \tag{3.10}$$

where $E_i$ is the energy in calorimeter cell $i$, $E_{tot}$ is the total energy of the shower, $\vec{x}_i$ is the position vector of cell $i$, and $w_0$ is a parameter that is tuned to optimize the position resolution. The position resolution found from the beam test for CC and EC are 1.5mm and 2.0mm respectively. This information is used to compute a quantity called track matching significance in Eq. 3.19 for further selection of electrons.

Due to an absence of a central magnetic field in the DØ detector, the $e^+e^-$ pairs from photon conversions overlap in space. The ionization per unit length ($dE/dx$) in the drift chambers can be used to discriminate multiple tracks from a single track. Figure 3.2 shows the distribution of $dE/dx$ for tracks of reconstructed objects corresponding to EM clusters in the calorimeter. The lower

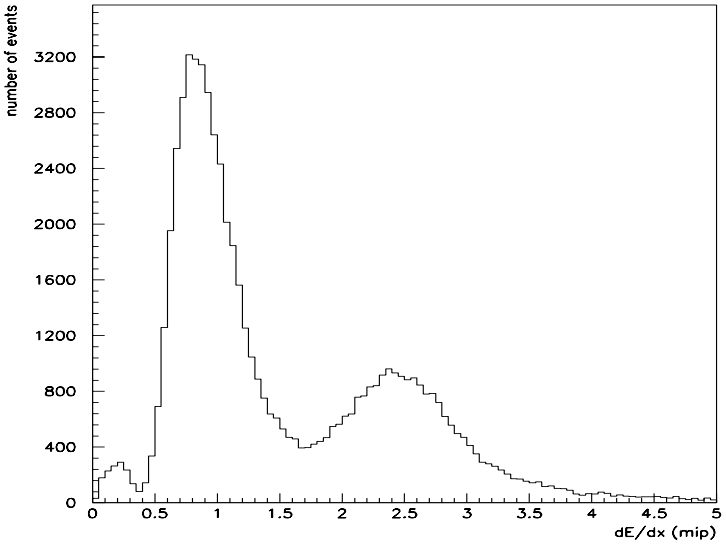


Figure 3.2: dE/dx distributions in drift chambers

peak is from minimum ionizing particles, whereas the second peak corresponds to two minimum ionizing tracks. Thus the $e^+e^-$ pairs from photon conversion can be discriminated using $dE/dx$.

Further selection criteria for electrons from $W$ decays are explained in detail in the following section.

### 3.2.3 Jets

Jets are clusters of particles produced from final state partons in a hard interaction. Because partons are subject to the strong interaction, no single colored parton can be observed before it turns into a stream of colorless final states which are hadrons. This process is called fragmentation and hadronization. These streams of particles have been observed and are commonly defined with using a cone in $\eta - \phi$ space. The radius of a cone defining a jet is

$\Delta R = \sqrt{\Delta\eta^2 + \Delta\phi^2}$.

There are two categories of algorithms defining jets in DØ. One is the cone algorithm. Three typical cone sizes are 0.3, 0.5 and 0.7. The other algorithm is the nearest neighbour algorithm described in the previous section. Most $P\bar{P}$ experiments adopt a cone algorithm.

The jets in the DØ detector are reconstructed in the following steps [37]:

- The algorithm begins from an $E_T$ ordered list of towers which are typically 0.1 in $\eta$ and $2\pi/64$ (approximately 0.1) in $\phi$. Preclusters are formed of contiguous cells within a radius of $\Delta R = \sqrt{\Delta\eta^2 + \Delta\phi^2} = 0.3$ starting from the highest $E_T$ calorimeter hadronic tower. The preclusters are formed to reduce the number of towers considered as a possible jet seeds.

- Taking the precluster center in $\eta - \phi$ space as the preliminary center of a jet, a new $E_T$ weighted center is formed from all towers within a cone of radius $\Delta R$. The $E_T$ of jets are computed at this stage by summing up the magnitude of the $E_T$ of the towers within the cone.

- The previous step is repeated until the jet is stable. (A study of Monte Carlo data showed that three or four iterations are sufficient.)

- Once a jet is formed, a threshold of 8 $GeV$ is applied to the $E_T$ of the jet.

- If any jets share energy, these jets are combined or split depending on the fractional energy shared relative to the $E_T$ of the lower $E_T$ jet. Jets are merged if they share more than 50% of the energy and split otherwise.

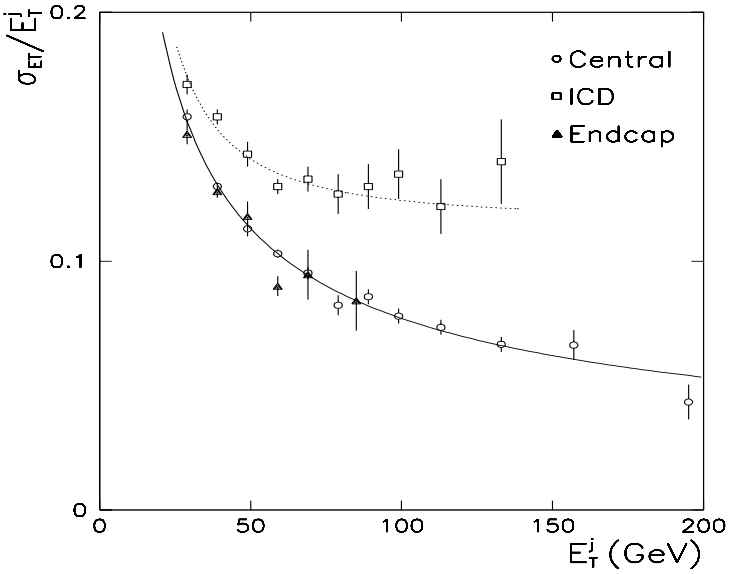


Figure 3.3: Jet $E_T$ resolution of the DØ calorimeter.

The jet energy resolution in the DØ detector has been measured from collider data using the tranverse momentum balance between two jets. Usually the jet $E_T$ ($E_T^j$) resolution can be parameterized as a function of $E_T^j$ with the following equation;

$$(\frac{\sigma}{E_T})^2 = C^2 + \frac{S^2}{E_T} + \frac{N^2}{E_T^2} \tag{3.11}$$

where $C$ is the error term from the calibration, $S$ is the shower fluctuation in the sampling gap, and $N$ corresponds to the detector noise and underlying event contribution. The fit values of these parameters from collider data are $C = 0$, $S = 0.74\sqrt{GeV}$, and $N = 2.16GeV$ for jets in the CC and EC, and are $C = 0.115$, $S = 0.32\sqrt{GeV}$, and $N = 3.36GeV$ for jets in the ICD [38]. Note that the jet energy resolution in the ICD region is worse than that of CC or EC. Figure 3.3 illustrates $E_T^j$ resolution as a function of $E_T^j$ in three different regions of the calorimeter.

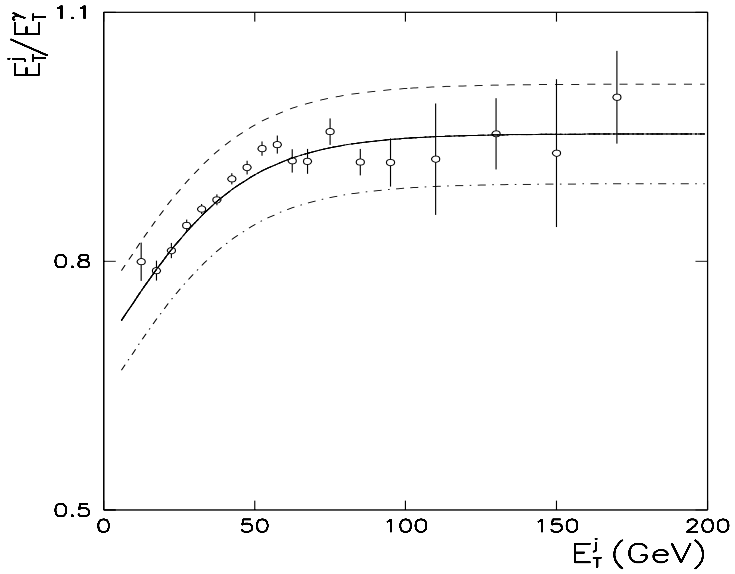


Figure 3.4: Calorimeter relative response of jet to photon as a function of jet $E_T$ ($E_T^j$).

The jet energy scale correction [39] is obtained using a technique developed by the CDF collaboration [40]. This technique uses the missing $E_T$ projection fraction. The DØ absolute jet energy correction is derived using events simulating direct photon ($\gamma$) events (either the real direct photon events or two jet events where one jet fluctuates highly electromagnetic). The missing $E_T$ projection fraction ($MPF$) is defined by the following equation:

$$MPF \equiv \frac{\vec{\not{E}}_T \cdot \hat{n}_j}{E_T^j} \tag{3.12}$$

where $\vec{\not{E}}_T$ is the missing $E_T$ vector, $\hat{n}_j$ is the unit vector of the jet axis on the transverse plane to the beam axis and $E_T^j$ is the $E_T$ of the jet. The relative response of the calorimeter to a jet is then derived from Eq. 3.12 as:

$$\frac{E_T^j}{E_T^\gamma} = \frac{1}{1 + MPF} \tag{3.13}$$

This relationship holds when there are only one jet and one photon in the event balancing each other. This scheme provides correction factors to the jet energy scale relative to the electromagnetic scale assuming a 100% EM response. The procedure for obtaining the DØ jet energy scale correction is as follows [39] [41]:

- Select events with only one jet and one photon in the CC.
- Require photon and jet to be back-to-back in azimuth to within 50 degrees.
- Determine jet energy scale correction of the jet in the CC from the relative response in Eq. 3.13. The correction factor is the inverse of the relative response.
- Correct central jets using the correction factor obtained in previous step. The size of this correction factor varies with $E_T$ and it is on the order of $20\% \pm 1\%$ at $E_T = 20$ GeV before correction.
- Subtract energy contribution from underlying events. This underlying event energy contribution has been measured in collider data and is approximately 4 GeV in cone of radius 0.7. The error from the estimation of the contribution from underlying events and uranium noise is $0.462\text{GeV}/E_T$ which corresponds to approximately 400 MeV for both effects.
- Scale up the jet energy to compensate the low absolute EM energy response in DØ. This scaling up was done based on the $Z$ boson mass

comparison between DØ and the $LEP$ experiments [42]. The estimated error from the electromagnetic scale is approximately 0.5%.

- Determine correction factor for jets in other regions of the detector relative to the CC jet from di-jet events using asymmetry variable,

$$A = \frac{E_T^{j_1} - E_T^{j_2}}{(E_T^{j_1} + E_T^{j_2})/2} \tag{3.14}$$

where $E_T^{j_1}$ is the uncorrected central jet $E_T$ and $E_T^{j_2}$ is the uncorrected probing jet $E_T$. The estimated error for this step is approximately 2.5% at $\eta = 2$.

Figure 3.4 illustrates the calorimeter response to a jet as a function of jet energy before the energy scale correction. The solid line is the fit through the data points. The errors of the data points are the linear sum of the systematic uncertainties from the EM energy scale, vertex correction in angle determination, underlying event energy contribution determination and the out of cone correction (roughly 2%). The other two lines in Fig. 3.4 are the fits through the upper and the lower bound of the systematic uncertainties which is approximately 6%. The systematic error is assigned conservatively because at the present time the various sources of the DØ jet energy scale error are not properly understood in the collider environment. However, this large systematic error is not randomly assigned but is assigned based on a Monte Carlo study using DØ test beam single particle response. This study was done by generating single jet events and replacing the detector response to each particle in the jet with the single particle response from the DØ test

beam. The major source of error in the test beam was poor statistics of low energy hadron response data. The size of the jet energy scale systematic error from this study was approximately 5.5%. This is understandable, because a jet is composed of hadrons with various energies but dominantly low energy hadrons. The error from the test beam low energy response is convoluted together with the particle energy distribution in the jet to get the overall jet energy scale error.

In this analysis, the systematic error due to jet energy scale calibration was estimated by analyzing the same data three times with three different energy scale corrections which were determined from the 6% error assigned on the jet energy scale. The difference in the central values from the jet energy corrections relative to the nominal correction (the central line in Fig. 3.4) are used as the jet energy scale systematic errors.

### 3.2.4 Muons

Muons have small nuclear cross sections. Therefore, the muon system surrounds the calorimeter volume which filters out all other particles from the interaction. The DØ muon reconstruction [43] [44] is done in two steps. First, the muon reconstruction program loops over all the hits in the muon chambers to determine their location and calculates their positions in the DØ coordinate system. At this stage all the necessary corrections (e.g, calibration constants, survey information, etc) are applied. Next, pattern recognition is done and the hits are used to form muon track segments. These are linked by

projection through the muon toroidal magnets to provide a measurement of the preliminary muon momentum. Later more elaborate muon fits are performed by linking the muon tracks to information from the calorimeter and central tracking system.

### 3.2.5 Missing $E_T$

Neutrinos are weakly interacting leptons which escape nearly 100% of the time from the detector. Therefore, the only way an experiment can measure the kinematic properties of neutrinos produced from a hard interaction is by relying on momentum conservation. However, the momentum conservation along the beam direction is not applicable because the longitudinal momenta of initial state partons are not known. On the other hand, the momentum conservation in the transverse direction is still applicable to the extent that initial partons contributing to the hard interaction have very little or no net transverse momentum. Therefore, the vector sum of the final state transverse momentum has to be close to zero.

In DØ, the momentum of a neutrino is reconstructed by summing all the transverse energy in the calorimeter cells vectorially. The negation of this vector would be the neutrino's transverse momentum. This definition can be written as follows:

$$\not\!\!E_x = -\sum_{i=1}^{n} E_i sin\theta_i cos\phi_i \tag{3.15}$$

$$\not\!\!E_y = -\sum_{i=1}^{n} E_i sin\theta_i sin\phi_i \tag{3.16}$$

$$\not\!\!E_T = \sqrt{\not\!\!E_x{}^2 + \not\!\!E_y{}^2} \tag{3.17}$$

where the index $i$ runs over all $n$ cells in the calorimeter, $E_i$ is the energy deposited in the cell $i$, and $\theta_i$ and $\phi_i$ are the polar and azimuthal angles, respectively, of the center of cell $i$ as measured from the reconstructed vertex of the event. This is a standard technique used for a finely segmented calorimeter. One difficulty with this algorithm is that if more than one neutrino results from the hard interaction then there is no way one can find out what the direction and magnitude of the $E_T$ of individual neutrinos are. This complicates the top quark search in the di-lepton decay channels which involve at least two neutrinos in the final state from the decay of two $W$ vector bosons involved in $t\bar{t}$ decay.

## 3.3 Offline selection criteria

The main characteristic used to select an event with a $W$ vector boson decaying into $e + \nu$ final state is an isolated high $P_T$ electron and a suitable amount of $\not\!\!E_T$ . The selection criteria are imposed only on electrons and $\not\!\!E_T$ to avoid any possible bias in the jet sample.

The selection criteria used in this analysis to extract an event with a $W \rightarrow e + \nu$ decay are as follows:

- H-matrix $\chi^2$ (electron shower shape)

    1. $\chi^2_{Hmatrix} < 100$ in the pseudo-rapidity range of $\mid \eta \mid < 1.3$
    2. $\chi^2_{Hmatrix} < 200$ in the pseudo-rapidity range of $1.3 < \mid \eta \mid < 2.5$
    3. $\chi^2_{Hmatrix} < 30$ in the pseudo-rapidity range of $2.5 < \mid \eta \mid$

- Isolation fraction:

$$Isolation = \frac{E^{total}_{\Delta R=0.4} - E^{EM}_{\Delta R=0.2}}{E^{EM}_{\Delta R=0.2}} < 0.15 \tag{3.18}$$

where $E^{total}_{\Delta R=0.4}$ is the total energy inside of a cone of radius 0.4 summed over all layers and $E^{EM}_{\Delta R=0.2}$ is the $EM$ energy inside of a cone of radius 0.2.

- Electromagnetic fraction of a candidate electron cluster greater than 0.9.

- Number of cells in the cluster above 50MeV has to be greater than 20 to eliminate false electrons caused by noisy cells in the EM calorimeter.

- Track matching significance between the reconstructed track and the candidate calorimeter cluster less than 10. The significance is defined as:

$$\sigma_{track} = \sqrt{(\frac{R\Delta\phi}{R\delta\phi})^2 + (\frac{\Delta z}{\delta z})^2} \tag{3.19}$$

where $R$ is the radial distance from the vertex to the center of the candidate $EM$ shower in cm, $\Delta\phi$ and $\Delta z$ are the difference between the track position and the shower center in azimuthal angle (radian) and the beam direction (cm), respectively, and $R\delta\phi$ and $\delta z$ are the position resolution of the calorimeter in the azimuthal and beam direction.

- No other electrons in the event satisfying the above electron quality cuts with $E_T > 10GeV$. This cut is introduced mainly to reject background from $Z \rightarrow e^+ + e^-$ candidates.

- Scalar $E_T$ in the event greater than 0 GeV and less than 1800 GeV to avoid obvious multiple interaction and pile up in the detector.
- $E_T$ of the electron $> 25$ GeV.
- Missing $E_T > 25$ GeV.

All of the above cuts are determined after a careful study of the efficiencies on the quantities [45]. This study was done by using $Z \rightarrow e^+e^-$ candidates from the collider data requiring one of the two electrons satisfy the above cuts and requiring the pair mass to be within 86 GeV$< m_{ee} <$ 96 GeV. The efficiencies are then determined by imposing each of the above cuts one at a time to the other electron which didn't have any cuts imposed. Figure 3.1 shows the H-matrix $\chi^2$ distribution of electrons from the test beam, pions from the test beam and the electrons from the collider data in the CC. The two distributions of the test beam electrons and pions are well separated at around $\chi^2 = 100$. Figure 3.5 and 3.6 show the distributions of H-matrix $\chi^2$ variables of the loosely selected electrons from the $Z \rightarrow e^+e^-$ candidates. Both distributions show optimized efficiencies for the H-matrix $\chi^2$ cuts in retaining electrons. The cuts are determined to keep the efficiencies approximately the same both in the CC and EC. Since the $\eta$ distribution of electrons from the $W$ decay diminishes quickly beyond approximately $\mid \eta \mid = 1.0$, the $\chi^2$ cut for the range of $\mid \eta \mid > 2.5$ very little impact on the electrons from $W$ decays. This cut for $\mid \eta \mid > 2.5$ is for the completion of the cuts to the maximum coverage of the detector. At the same time the cut in this region contributes reducing any possible background occupying this region. In addition since there are not

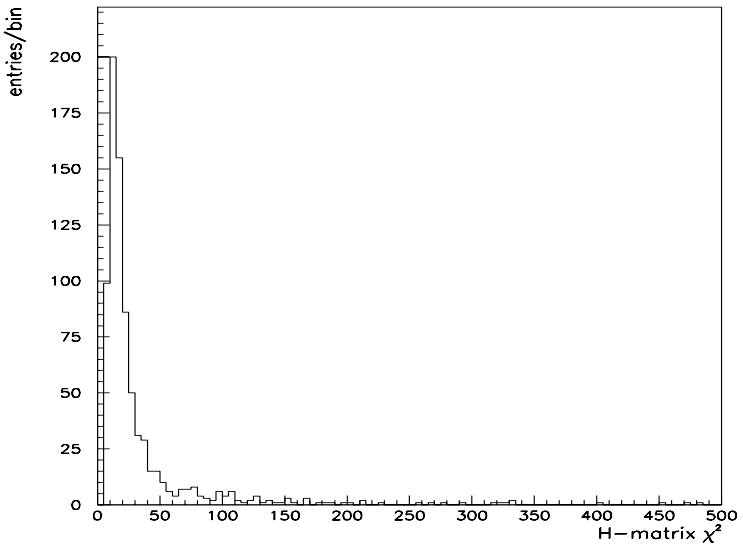


Figure 3.5: H-matrix $\chi^2$ distributions of electrons from $Z \rightarrow e^+e^-$ events from collider data in the CC.

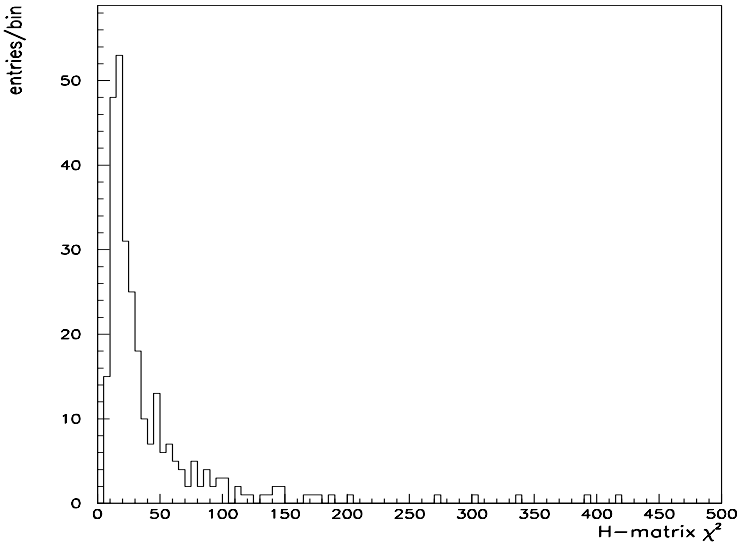


Figure 3.6: H-matrix $\chi^2$ distributions of electrons from $Z \rightarrow e^+e^-$ events from collider data in the EC.

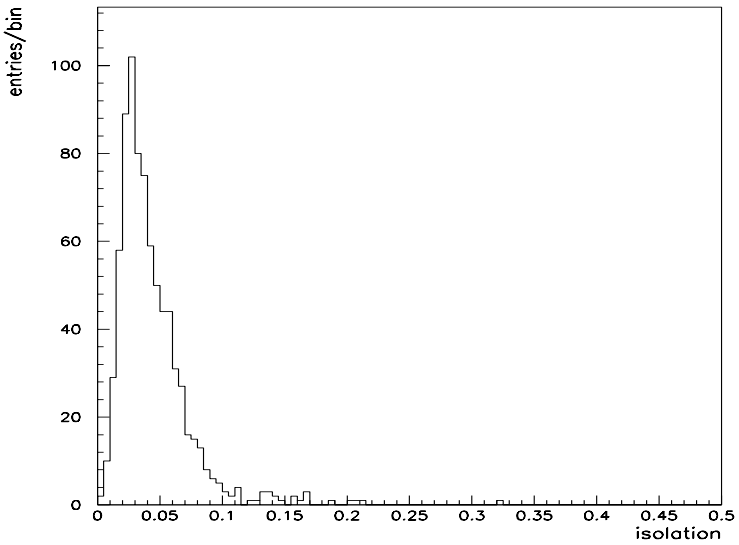


Figure 3.7: Isolation fraction distributions of electrons from $Z \rightarrow e^+e^-$ events from collider data in the CC.

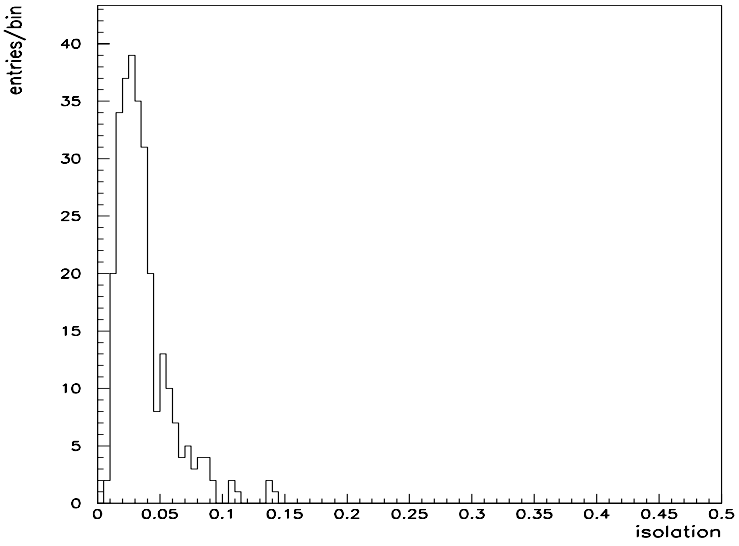


Figure 3.8: Isolation fraction distributions of electrons from $Z \rightarrow e^+e^-$ events from collider data in the EC.

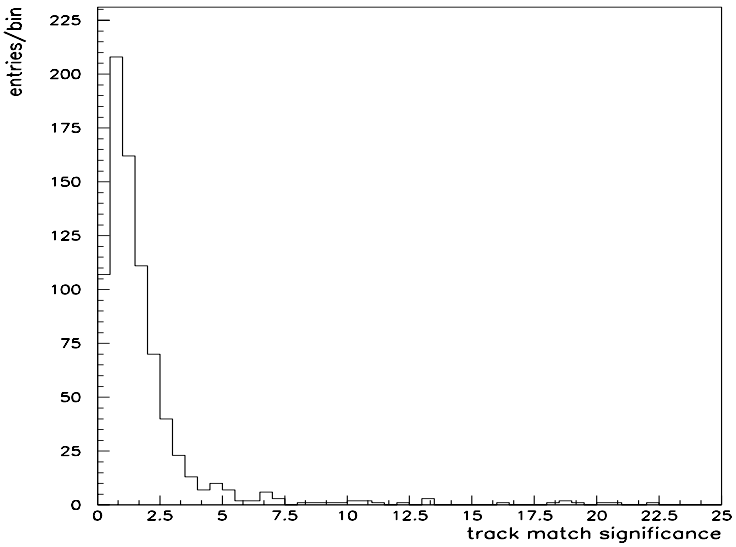


Figure 3.9: Track matching significance distributions of electrons from $Z \rightarrow e^+e^-$ events from collider data in the CC.

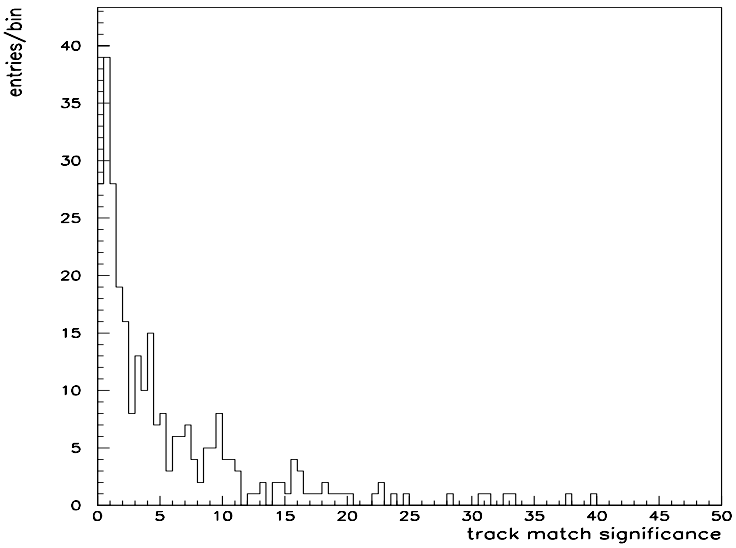


Figure 3.10: Track matching significance distributions of electrons from $Z \rightarrow e^+e^-$ events from collider data in the EC.

| Cut | $\eta_{Det}$ | efficiency (%) |
|---|---|---|
| $\sigma_{track}$ | $\leq 1.1$ | $96.5 \pm 0.6$ |
| | $> 1.1$ | $81.6 \pm 2.3$ |
| $\chi^2$ | $\leq 1.1$ | $92.2 \pm 0.9$ |
| | $> 1.1$ | $96.9 \pm 1$ |
| Isolation | $\leq 1.1$ | $98.2 \pm 0.5$ |
| | $> 1.1$ | $99.7 \pm 0.3$ |

Table 3.2: Efficiencies of electron quality cuts

many electrons from the decay of the $Z$ bosons present in $\mid \eta \mid > 2.5$ the efficiency study from collider data is practically impossible. The total efficiency including this region is given at the end of this section based on the Monte Carlo study.

Figure 3.7 and 3.8 show the distributions of the isolation fraction variables defined in Eq. 3.18 for the loosely selected electrons in the CC and EC, respectively. Figure 3.9 and 3.10 show the distribution of the track matching significance for the electrons in the CC and EC, respectively. The thresholds of these quantities are set to retain the maximum efficiencies for electrons. Table 3.2 summarizes the efficiencies of these cuts.

Since the ratio of the $W+1$ jet to the $W+0$ jet is the physical observable in this analysis, it is important to keep the efficiencies of the above cuts the same independent of event topology to eliminate systematic error. However, since the kinematic cuts on the decay products and the isolation criteria are

simulated in the Monte Carlo used in this analysis (see chapter 5), the only cuts that needs to be verified for the identical efficiencies are the H-matrix $\chi^2$ cuts and the track matching significance cut. The efficiencies of these cuts for event topology were also investigated using the $Z + 0$ jet and the $Z + 1$ jet events [45]. The jet minimum $E_T$ cutoff ($E_T^{min}$) used for $Z + 1$ jet samples was the DØ default value of 8 GeV (see section 3.2.3). The study showed that the efficiencies of both cuts are the same within error for both the 0 jet and 1 jet samples [45]. The dominant error in this study was the statistical uncertainty. The errors were on the order of 1-2% and 3-5% in the CC and EC, respectively. The efficiencies of the cuts are the smallest at the lowest $E_T^{min}$ where there is small but measuable probability for the electron to overlap with the jet. Therefore, the efficiencies at the lowest $E_T^{min}$ is the lower limit, because as the $E_T$ of jet increases the separation between the electron and the jet increases and the possibility of the overlap between the jet and the electron decreases. This is because the $W$ in the event has to balance the $E_T$ of the jet so that the decay products of the $W$ tend to be more back-to-back with the jet.

There are a few more cuts applied to remove instrumental background. An event is rejected if there is any indication of noisy cells defined by the following conditions which are applied to jets in the events reconstructed with the nearest neighbor algorithm:

- The ratio of the energy of maximum cell to second maximum cell in the cluster is greater than 15.

- The fraction of the cluster energy deposited in the coarse hadronic calorimeter is greater than 0.4.

- The fraction of the cluster energy deposited in the EM calorimeter is less than 0.1.

The effect of the above cuts was studied using full DØ detector simulated Monte Carlo event samples and showed an average of 99% efficiency below 90 GeV jet $E_T$. In addition, the effect of more stringent thresholds for the above quantities to good jets has been investigated using $11.5 pb^{-1}$ of jet triggered events [46]. The cone size was fixed at 0.7. The good jets distributions for above quantities were defined after the noisy jets are removed as much as possible. The efficiencies after all of the cuts were applied were an average of 98% for jets with $E_T$ below 90 GeV. Therefore, these cuts have virtually no effect at all on the ratio of the number of the $W + 1$ jet to $W + 0$ jet events in the $E_T$ range of interest.

## 3.4 Total efficiency

A study using a sample of DØ detector simulated Monte Carlo events showed that the total efficiency for all the above selection criteria including trigger, the detector geometric acceptance, and the kinematic acceptance is $(33.1 \pm 1.1)\%$.

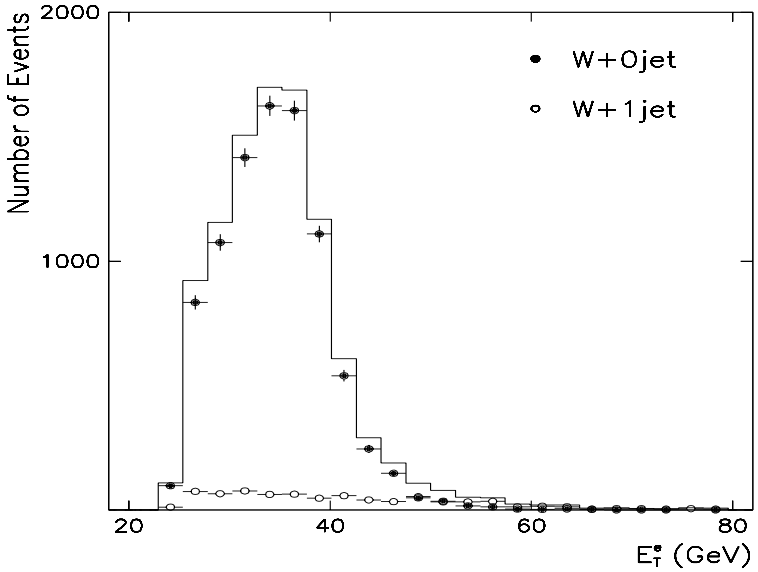


Figure 3.11: $E_T^e$ distributions for selected candidates for all $W$ (histogram), $W + 0$ jet(solid circle), and $W + 1$ jet (open circle) with $E_T^{min} > 25$GeV.

## 3.5 Final data sample

The total number of $W$ candidates after offline selection is 9770. The selection of events is done independent of the number of associated jets. The jet energy scale correction is done on the final events. Figures 3.11 and 3.12 show the momentum distributions of the decay products from the $W$. The histogram is for all selected candidates whereas solid and open data points represent the transverse momentum distributions of the $W$ decay products from the $W + 0$jet and $W + 1$jet candidates with jet minimum $E_T$ ($E_T^{min}$) $> 25$ GeV, respectively. The $E_T$ of the electron is directly measured by the detector whereas $\not\!\!E_T$ is reconstructed from the momentum vectors of objects in the event. Therefore, the $\not\!\!E_T$ distribution is expected to be more sensitive to the

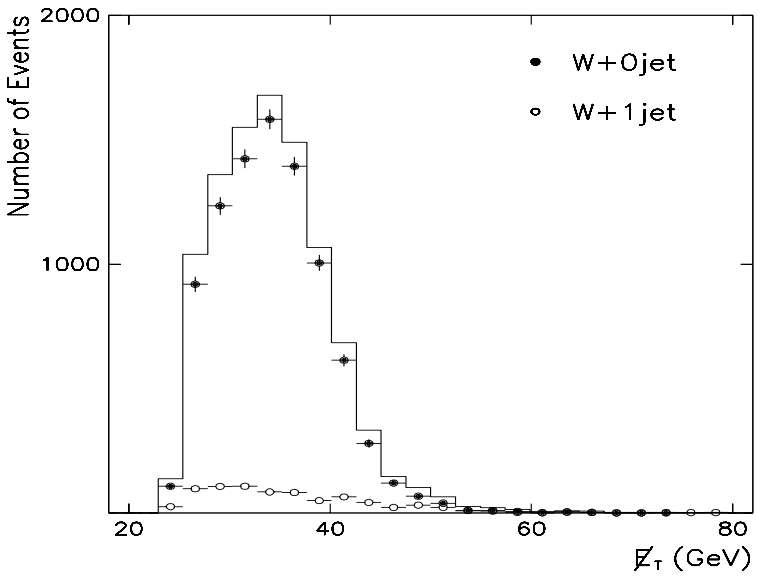


Figure 3.12: $\not\!\!E_T$ distributions for selected candidates for all $W$ (histogram), $W + 0$ jet(solid circle), and $W + 1$ jet (open circle) with $E_T^{min} > 25$GeV.

detector resolution. Since the result of this analysis does not depend on the absolute energy scale of electron nor $\not\!\!E_T$ , none of the known corrections (such as high voltage correction, etc) for the absolute energy of the electrons are applied. The vertical error bar on each data point is the statistical error. The horizontal error bars indicate the bin size.

Figure 3.13 shows the transverse mass distributions reconstructed from the kinematics of the event. The formula for the $W$ transverse mass [47], $M_T^W$ , is defined as follows:

$$M_T^W = \sqrt{2E_T^e \not\!\!E_T \, (1 - cos\phi_{e\nu})} \tag{3.20}$$

where $E_T^e$ is the transverse energy of the electron, $\not\!\!E_T$ is the reconstructed missing $E_T$ of the event, and $\phi_{e\nu}$ is the azimuthal angle between the electron

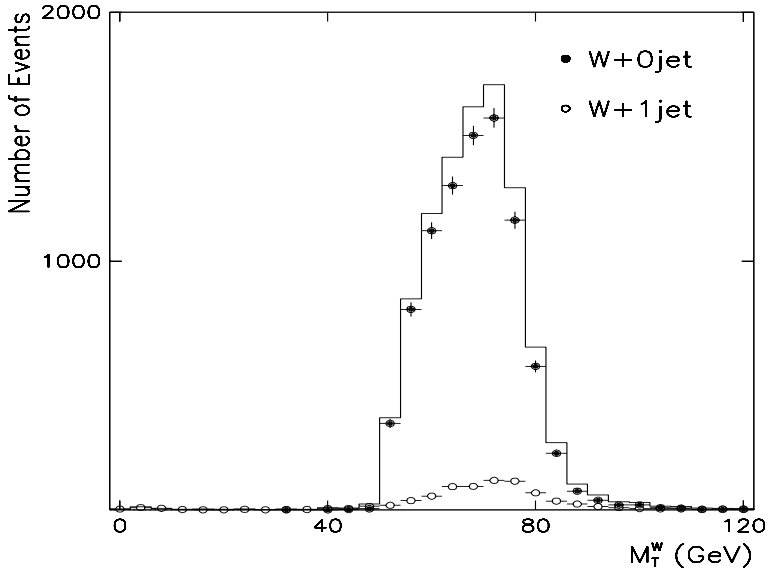


Figure 3.13: $M_T^W$ distributions for selected candidates for all $W$ (histogram), $W + 0$ jet(solid circle), and $W + 1$ jet (open circle) with $E_T^{min} > 25$GeV.

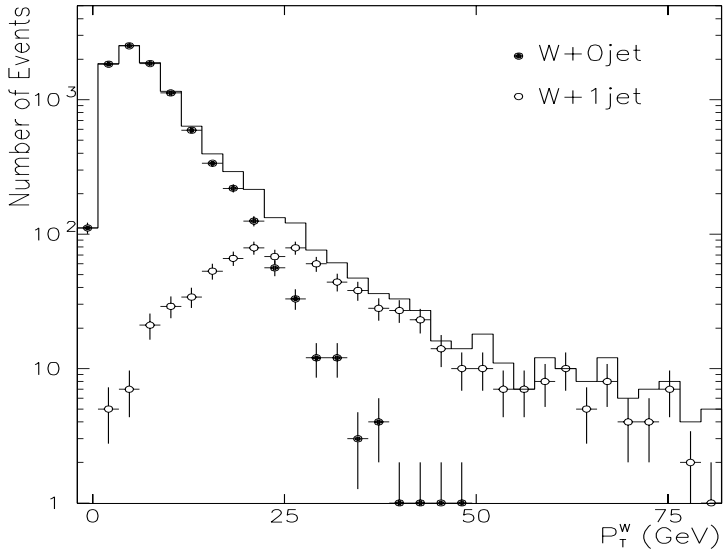


Figure 3.14: $P_T^W$ distributions for selected candidates for all $W$ (histogram), $W + 0$ jet(solid circle), and $W + 1$ jet (open circle) with $E_T^{min} > 25$GeV.

and $\not\!\!E_T$ vector. The histogram shows the transverse mass distributions of all selected candidates independent of the number of associated jets. Solid and open data points represent the transverse mass distribution of $W + 0$ jet and $W + 1$ jet candidates with $E_T^{min} > 25$ GeV, respectively.

Figure 3.14 illustrates the transverse momentum distributions of the $W$ for the selected candidates. The transverse momentum is computed from the vector sum of electron $E_T$ and $\not\!\!E_T$ in the event. The histogram is from all candidates whereas solid and open data points represent the transverse momentum distribution of the $W$ from the $W + 0$ jet and $W + 1$ jet candidates, respectively. Here one can find a drastically different behavior between the two samples. The transverse momentum of the $W$ from the $W + 1$jet events is much harder than that of the $W + 0$jet events.

# Chapter 4

# Backgrounds

It is possible to remove a substantial fraction of background in an analysis using stringent offline selection criteria. The estimates of backgrounds for this analysis are discussed in this chapter.

The physical quantity measured in this analysis, the ratio of the $W + 1$jet to $W + 0$jet cross sections, is vulnerable to several backgrounds from various sources. Backgrounds which come from the same source may have different levels of contribution for different event topologies. Therefore, the estimates of backgrounds have to be done for each different event topology.

In order for a background event to mimic a $W \rightarrow e + \nu$ event in this analysis, it must imitate both the high $E_T$ electron satisfying the offline criteria in section 3.3 and the high $\not\!\!E_T$ requirements of the online and offline cuts. The $\not\!\!E_T$ may be caused by mismeasurement in $E_T$ due to inherent detector resolution, lack of hermeticity, nonlinear response of the calorimeter, noisy cells in the calorimeter, malfunction of calorimeter electronics, the improper determination of hadronic response relative to the electromagnetic response. The last

possibility is a substantial source of background for this analysis because all the events which passed the online filter must have a high $E_T$ electromagnetic cluster.

On the contrary, background from two sources can satisfy the high $E_T$ electron selection criteria. One source of high $E_T$ electron is not from the real electrons but from electromagnetic clusters passing the selection criteria. These electrons are not the electrons from the $W$ decay but from the QCD multi-jet events faking good electrons. These events can be background for the signal if the $\not\!\!E_T$ is substantially mismeasured. This background can be estimated from the collider data by comparing its $\not\!\!E_T$ spectrum with that of topologically similar events (i.e. events with a high $E_T$ electromagnetic cluster). The background from QCD multijet events and instrumental effects are in this category. The estimation of this background is discussed in the first section of this chapter.

The other source of electrons is the decay of heavy mass states (e.g, $Z \rightarrow e^+e^-$ when one of the two electrons is misidentified). These events produce real high $E_T$ electrons satisfying the selection criteria which can become background to the signal if the $\not\!\!E_T$ is significantly mismeasured or if real neutrinos are involved in the decay. Background from these sources are estimated with Monte Carlo in the second section of this chapter.

The combined number of background events from the above sources and the number of the $W + 1$ jet and the $W + 0$ jet candidates after background subtraciton are given in the last section.

| $E_T^{min}$ $(GeV)$ | CC 0j$\pm stat \pm sys$ (%) | CC 1j $\pm stat$ $\pm sys$ (%) |
|---|---|---|
| 20 | $2.73 \pm 0.56^{-0.20}_{+0.02}$ | $16.09 \pm 3.33^{+1.30}_{-3.83}$ |
| 25 | $2.98 \pm 0.57^{-0.12}_{+0.16}$ | $20.41 \pm 4.42^{+1.72}_{-1.30}$ |
| 30 | $3.43 \pm 0.60^{-0.17}_{+0.04}$ | $19.48 \pm 4.97^{+1.11}_{-3.73}$ |
| 35 | $3.35 \pm 0.59^{-0.08}_{+0.01}$ | $26.42 \pm 6.26^{+3.85}_{-0.61}$ |
| 40 | $3.40 \pm 0.59^{-0.04}_{+0.05}$ | $33.06 \pm 7.30^{+6.82}_{-1.20}$ |
| 45 | $3.44 \pm 0.59^{-0.04}_{+0.13}$ | $34.87 \pm 7.72^{+0.89}_{-4.15}$ |
| 50 | $3.67 \pm 0.60^{-0.09}_{+0.18}$ | $27.97 \pm 7.61^{+1.38}_{-0.83}$ |
| 55 | $3.84 \pm 0.62^{-0.17}_{+0.01}$ | $27.95 \pm 7.90^{+0.42}_{-8.89}$ |
| 60 | $3.84 \pm 0.61^{-0.01}_{+0.15}$ | $36.81 \pm 9.39^{+9.31}_{-3.33}$ |

Table 4.1: Fraction of QCD background for W+0j and W+1j with the electron in the CC as a function of jet minimum $E_T$ cut ($E_T^{min}$)

## 4.1 QCD multi-jet events and instrumental effects

For a QCD multi-jet event to mimic the $W \rightarrow e + \nu$ signal, it must have a jet faking a good electron and suitable amount of $\not\!\!E_T$ . A jet can fake a good electron, if it has a high energy neutral particle accompanied with one or more low energy charged particles. The probability of a jet faking a good electron satisfying all the electron quality criteria described in section 3.3 has been studied [48]. The study demonstrated that the probability is on the order of $10^{-3}$. However, since the cross section of QCD multi-jet event is high, there is a considerable number of QCD multi-jet events being misidentified as event containing good electrons.

| $E_T^{min}$ $(GeV)$ | EC 0j$\pm stat \pm sys$ (%) | EC 1j $\pm stat$ $\pm sys$ (%) |
|---|---|---|
| 20 | $10.48 \pm 1.38^{-1.14}_{+0.03}$ | $36.26 \pm 4.24^{+1.37}_{-7.80}$ |
| 25 | $11.16 \pm 1.36^{-0.42}_{+0.31}$ | $50.64 \pm 4.82^{+6.51}_{-2.84}$ |
| 30 | $13.51 \pm 1.42^{-2.12}_{+0.34}$ | $53.47 \pm 5.51^{+1.85}_{-1.56}$ |
| 35 | $14.33 \pm 1.44^{-0.43}_{+0.49}$ | $47.43 \pm 5.92^{+0.73}_{-11.85}$ |
| 40 | $14.05 \pm 1.41^{-0.04}_{+1.42}$ | $67.96 \pm 6.23^{+18.73}_{-13.94}$ |
| 45 | $15.70 \pm 1.46^{-1.51}_{+0.11}$ | $57.11 \pm 7.41^{+13.75}_{-2.32}$ |
| 50 | $16.45 \pm 1.47^{-0.44}_{+0.20}$ | $45.31 \pm 8.38^{+6.06}_{-2.63}$ |
| 55 | $16.98 \pm 1.48^{-0.18}_{+0.16}$ | $34.78 \pm 9.11^{+5.54}_{-3.16}$ |
| 60 | $17.08 \pm 1.48^{-0.54}_{+0.12}$ | $34.74 \pm 10.50^{+9.17}_{-0.34}$ |

Table 4.2: Fraction of QCD background for W+0j and W+1j with the electron in the EC as a function of jet minimum $E_T$ cut ($E_T^{min}$)

Since QCD multi-jet events have in general little $\not\!\!E_T$ , a perfect detector will not generate large $\not\!\!E_T$ for these events. However, in practice there are always causes of substantial $\not\!\!E_T$ mismeasurement in a detector as explained previously. One of the sources of substantial $\not\!\!E_T$ mismeasurement comes from instrumental effects. Noisy cells in the calorimeter can add energy independent of an interaction and cause imbalance in the $E_T$ in the event. In most cases, these kinds of instrumental effects are easy to remove because the cells are in general well isolated. However, in some cases these cells can be overlapped with a real object (e.g. jets or electrons) in an event and may not be removable. Therefore, the background from this effect also needs to be estimated. Since this effect occurs randomly, estimates of backgrounds for normal QCD multi-jet events using collider data will also include this effect.

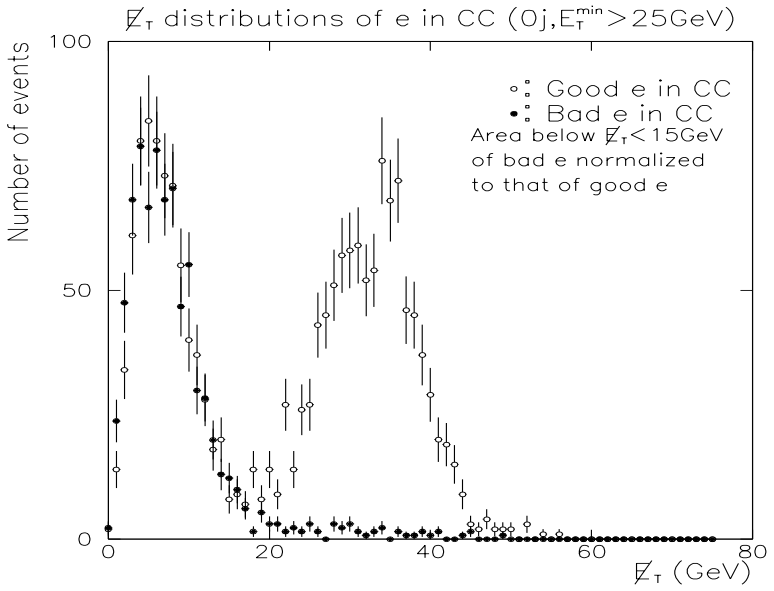


Figure 4.1: $\not\!\!E_T$ distributions for W+0j in CC. Open circles represent "good" electrons and solid circles are "bad" electrons.

Based on the concept explained previously, background from both the QCD multi-jet events and instrumental effects are estimated by choosing a set of EM triggers without missing $E_T$ constraints. This trigger requirement is exactly the same as $ELE - MAX$ except it has no $\not\!\!E_T$ requirement at Level 2.

Two sets of $\not\!\!E_T$ spectra are obtained from the events passing the trigger requirement. The first is the $\not\!\!E_T$ spectrum from events with electrons satisfying the selection criteria in section 3.3 ("good" electrons). The second is the $\not\!\!E_T$ spectrum from events with the electromagnetic cluster failing the selection criteria ("bad" electrons). To increase the statistics of bad electrons and to remove as many of the real electrons from the signal, the following cuts are applied to both the electrons and photons:

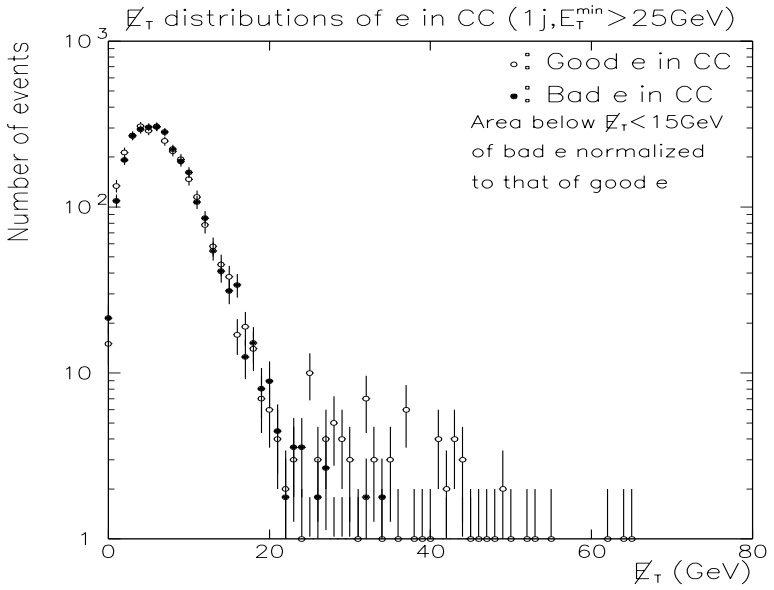


Figure 4.2: $\not\!\!E_T$ distributions for W+1j in CC. Open circles represent "good" electrons and solid circles are "bad" electrons.

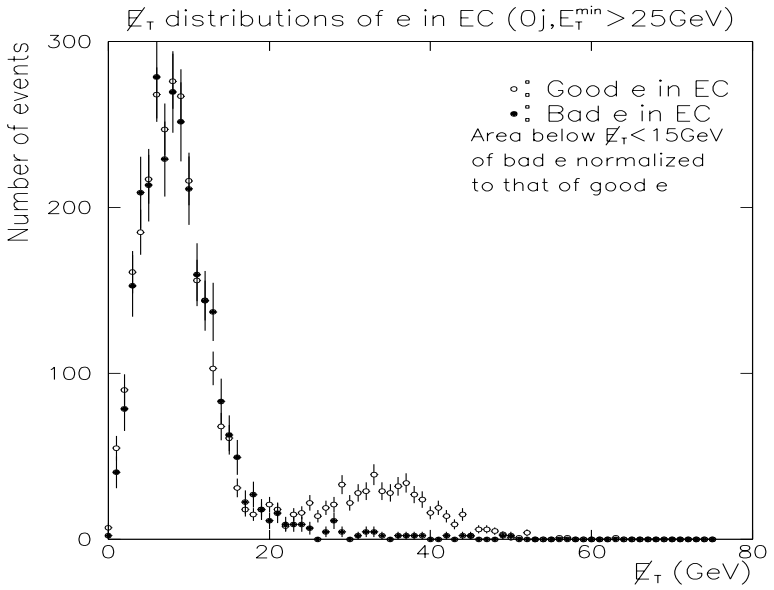


Figure 4.3: $\not\!\!E_T$ distributions for W+0j in EC. Open circles represent "good" electrons and solid circles are "bad" electrons.

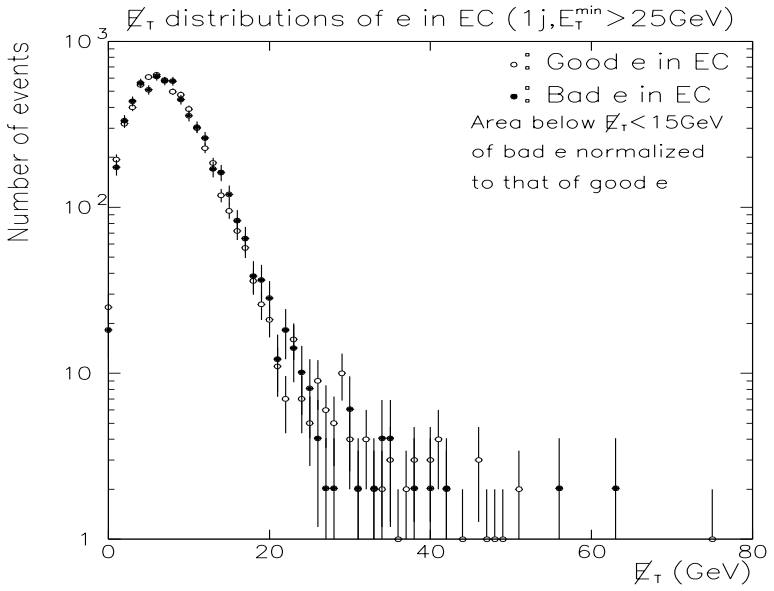


Figure 4.4: $\not\!\!E_T$ distributions for W+1j in EC. Open circles represent "good" electrons and solid circles are "bad" electrons.

- Electromagnetic fraction of a candidate electron cluster greater than 0.9.
- H matrix $\chi^2$ greater than 200 (independent of $\eta$).
- isolation fraction greater than 0.2.
- One and only one electron/photon in an event.
- $E_T$ of the electron/photon $>$ 25 GeV.

Based on a Monte Carlo study with $W + 0$ jet (1983 events), $W + 1$ jet (2003 events), and $W + 2jet$ (1527 events), non of the events from the $W + 0$ jet and the $W + 1$ jet sample passed the above cuts whereas only 1 event from the $W + 2$ jet sample passed the cuts. Thus, there is extremely small probability for the most of the $W$ events passing the above cuts. Therefore, these cuts

are already close to 100% efficient in removing the $W$ candidates from the background samples. In addition to the above four criteria which must be satisfied all at the same time, following few more cuts are given as optional cuts:

- Track matching significance >10 (electrons only).
- Number of cells in the cluster above 50MeV less than 20.
- Scalar $E_T$ in the event less than 0 GeV or greater than 1800 GeV.

Note that the offline $\not\!\!E_T$ requirement is not applied for both spectra. The $\not\!\!E_T$ spectra of these two samples can then be compared by normalizing the integrated area of $\not\!\!E_T$ spectra below 15 GeV. Figures 4.1, 4.2, 4.3 and 4.4 show the $\not\!\!E_T$ spectrum of both samples depending on the event topology and the location of the good electrons or bad electrons. The $\not\!\!E_T$ spectra from the good electron samples are indicated with open circles in the plots. Likewise, the $\not\!\!E_T$ spectra from bad electron samples are indicated with solid circles. These figures show that the two normalized spectra of these two samples are indistinguishable below 15 GeV. This gives us confidence that this way of estimating the background is correct.

The $\not\!\!E_T$ spectra for events with a good electron are the sums of two distributions. The low $\not\!\!E_T$ region is a convolution of two Gaussian distributions (see the definition of $\not\!\!E_T$ in the section 3.2.5) which is expected from the events with very little $\not\!\!E_T$ . The events without legitimate $\not\!\!E_T$ will have the Gaussian distributions of $\not\!\!E_x$ and $\not\!\!E_y$ close to zero. Therefore, the quadratic sum of

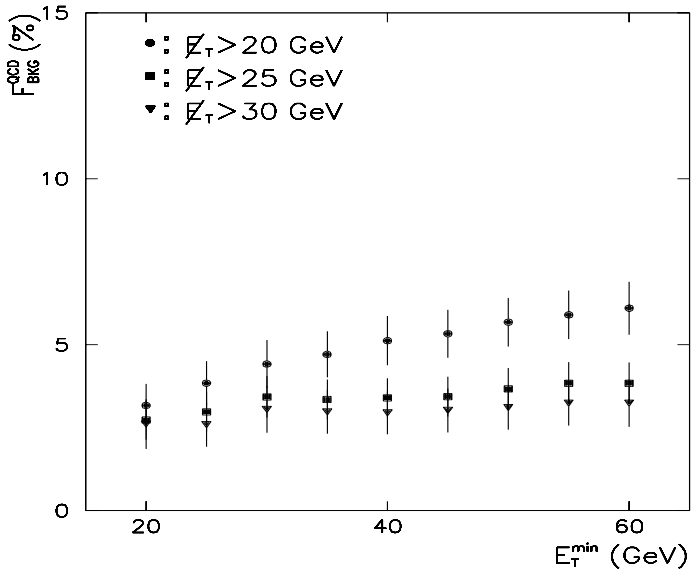


Figure 4.5: QCD background fraction for W+0j in CC vs jet minimum $E_T$ cut ($E_T^{min}$).

these two Gaussian will show the distribution of the low $\not\!\!E_T$ region [49]. This distribution comes from the QCD multi-jet backgrounds which have little $\not\!\!E_T$ beyond that coming from the detector resolution. The other distribution, occupying a region around 40GeV, comes from the real neutrinos from the $W$ decays.

The contribution of background is then estimated by the fraction of the integrated area of $\not\!\!E_T$ spectra of the bad electrons above 20, 25, and 30 GeV to the integrated area of $\not\!\!E_T$ spectrum of the good electrons with the same $\not\!\!E_T$ thresholds. Table 4.1 and 4.2 show the fraction of estimated backgrounds with $\not\!\!E_T$ above $25GeV$ as a function of jet minimum $E_T$ ($E_T^{min}$) for events with an electron in the CC and the EC, respectively. The systematic errors due to jet energy scale in the tables are estimated by doing the same background

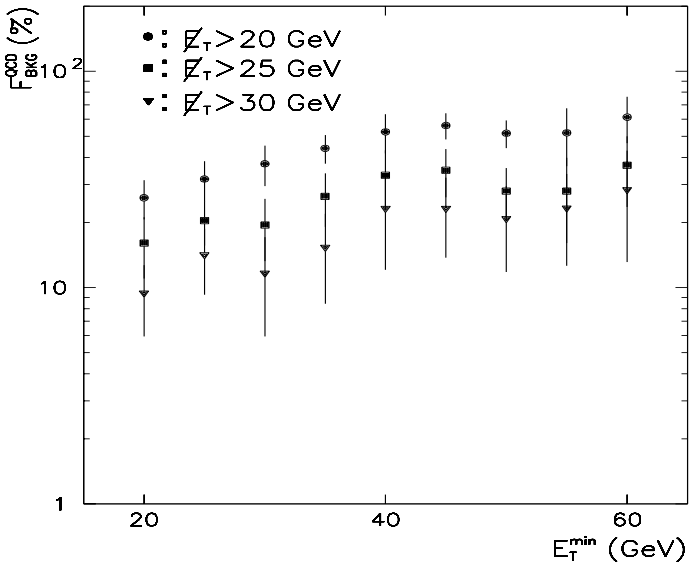


Figure 4.6: QCD background fraction for W+1j in CC vs jet minimum $E_T$ cut ($E_T^{min}$).

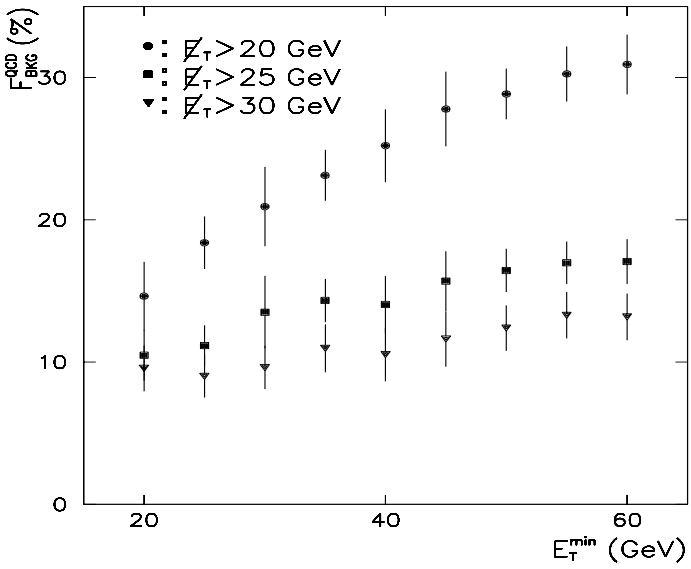


Figure 4.7: QCD background fraction for W+0j in EC vs jet minimum $E_T$ cut ($E_T^{min}$).

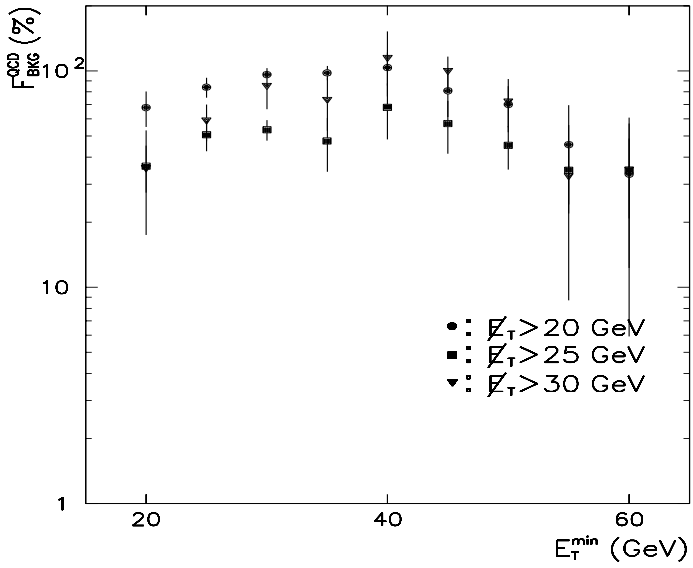


Figure 4.8: QCD background fraction for W+1j in EC vs jet minimum $E_T$ cut ($E_T^{min}$).

analysis with the three different energy scale corrections (see 3.2.3). However, since these errors are estimated under the assumption that the $E_T$ distribution of the jets in the normal QCD multi-jet events are almost completely different from the distribution of the jets associated with $W$, the errors might be overstimated. Dispite of the possible overestimation of the systematic errors in the background estimation, the systematic errors in the background estimation does not affect to the final results because the errors in the tables are not directly used in the error estimation of the final results. The global behavior of the background fraction is graphically demonstrated in Figs 4.5, 4.6 , 4.7, and 4.8. It is clear from the plots that the fraction of background decreases as $\not\!\!E_T$ threshold increases.

A study was done on the variation of the background fraction depending

on applying stricter cuts on $\chi^2$ values (see section 3.3). When the cuts on $\chi^2$ are tightened by factor two in the EC and the CC, it is observed that the fraction of the background in the EC is almost the same as that in CC (note that the $\chi^2$ cut on the EC is set twice higher than that in the CC). On the other hand, no gain in signal to background ratio was observed by tightening $\chi^2$ in the CC. This means that the rejection power increases with tightening $\chi^2$ on electrons to a certain the value of $\chi^2$. However, after passing the value, real electrons start to be rejected by the same or greater factor than the background.

## 4.2 Background from electroweak processes

In most cases, the other electroweak processes do not mimic $W$ events. However, a study performed using full DØ detector simulated Monte Carlo event samples showed that under certain conditions an electroweak process can actually mimic the $W + n$ jets signal either due to misidentification of decay products in the detector or due to the presence of a real electron, neutrino, and jets in the final states. In this section, the contributions from these processes are discussed.

### 4.2.1 $Z \rightarrow e^+ + e^-$

In most cases this process has very definite objects, electrons, in the final state. If a detector is perfect and has no crack or inefficiencies then this will never mimic $W \rightarrow e + \nu$ signal. But since in practice there are cracks in

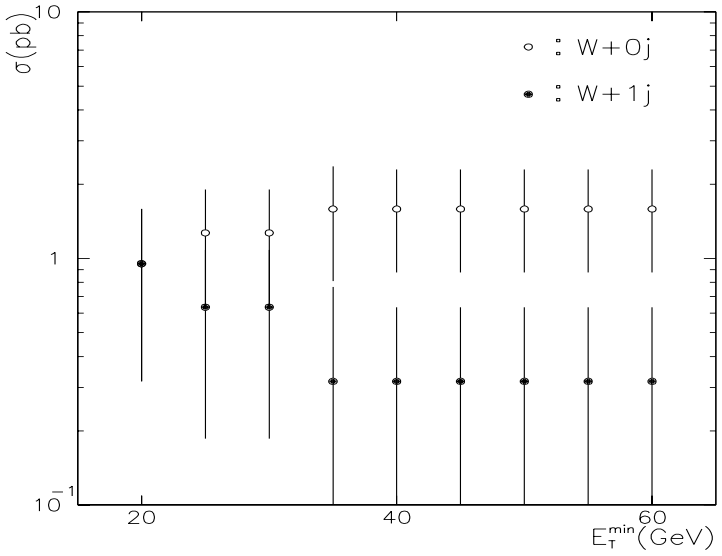


Figure 4.9: Effective cross section of $Z \rightarrow e^+ + e^-$ Monte Carlo samples ($\sigma_{eff}(Z \rightarrow e^+ + e^-)$ vs jet minimum $E_T$ cut ($E_T^{min}$) in the CC.

the detector, even if the fiducial volume of the cracks is small, the probability of misidentifying an electron as a jet is rather large making this process mimic $W + n(\geq 0)$ jets signal. For mechanical reasons, the DØ calorimeter has projective $\phi$ cracks between the CCEM modules ($\Delta\phi = 0.2$). Whenever an electron goes through this region, the energy lost is not likely to be fully recovered. This will cause an imbalance in the $E_T$ measurement of the final state and create false $\not\!\!E_T$ in the event. In addition to that, the DØ electron reconstruction algorithm requires that the EM fraction of a cluster be more than 90% to be identified as an electron, so the electron in the crack region of the detector will be misidentified as a jet with rather high $E_T$

The $Z \rightarrow e^+ + e^-$ samples used here were generated with the ISAJET Monte Carlo with initial kinematic cuts on the transverse momentum of both

| $E_T^{min}$ $(GeV)$ | CC 0j$\pm stat \pm sys$(pb) | CC 1j $\pm stat \pm sys$ (pb) |
|---|---|---|
| 20.0 | $0.95\pm0.55^{-0.32}_{+0.32}$ | $0.95\pm0.55^{+0.32}_{-0.32}$ |
| 25.0 | $1.27\pm0.63^{-0}_{+0}$ | $0.63\pm0.45^{+0}_{-0}$ |
| 30.0 | $1.27\pm0.63^{-0}_{+0}$ | $0.63\pm0.45^{+0}_{-0}$ |
| 35.0 | $1.59\pm0.71^{-0.32}_{+0}$ | $0.32\pm0.32^{+0.32}_{-0}$ |
| $\geq$40.0 | $1.59\pm0.71^{-0}_{+0}$ | $0.32\pm0.32^{+0}_{-0}$ |

Table 4.3: $\sigma_{eff}(Z \rightarrow e^+ + e^-)$ for jet minimum $E_T$ cutoff ($E_T^{min}$) values in the CC.

electrons from $Z$ decay to be greater than 5 GeV. The total number of events generated was 600 which corresponds to $(2.9 \pm 0.12)pb^{-1}$. The interaction vertex was smeared according to the measured distribution of the interaction position ($\sigma$ = 30cm) from the collider data and shifted by 7 cm in $z$ toward the incoming proton direction These samples were put through the full DØ detector simulation and were reconstructed with the DØ reconstruction program. Then the standard selection criteria discussed in section 3.3 were imposed to select those events mimicking the $W \rightarrow e + \nu$ signal. Figure 4.9 and Table 4.3 show the effective integrated cross section as a function of jet minimum $E_T$ ($E_T^{min}$) for $W$ + 0jet and $W$ + 1jet with electron in the CC. In the EC only one event with no jet was left at all $E_T^{min}$ after the selection. This one event corresponds to the effective integrated cross section of $0.32 \pm 0.32$ pb.

The total effective inclusive cross section of the background from this channel is $(2.23 \pm 0.87)$ pb (see the cross sections at $E_T^{min}$ = 35 GeV), so the relative fraction to the total cross section of $W(\rightarrow e + \nu) + X$ is small (roughly

0.3%). However, as illustrated in Fig. 4.9 and Table 4.3 for $W + n(> 0)$ jets, the contribution can be as large as a few percent depending on $E_T^{min}$. The systematic errors in the tables might have been over estimated, because the fake jet in this background has only one particle with high energy and the response in the detector is better than that from normal jet which is composed of many hadrons with various energies. In addition, the errors in the tables are not directly used in estimating jet energy scale systematic error in the ratio of the $W + 1$jet to the $W + 0$jet cross sections, because all the systematic errors in the final results are determined by doing the same analysis three times with three different energy scale corrections (see 3.2.3). Note that the effective cross sections don't fall with $E_T^{min}$, because the background source arises from the misidentified electron from Z whose $E_T$ is approximately $M_Z/2$ (45 GeV). Moreover, since the relative contributions of background from this process to the $W + 0$jet and $W + 1$jet are different, the effect on the ratio is larger than it would appear from the inclusive cross sections.

### 4.2.2 $Z \rightarrow \tau^+ + \tau^-$

This process can create a real electron, neutrinos, and a hadronic jet when one $\tau$ decays to $e + \nu_e + \nu_\tau$ and the other $\tau$ decays hadronically. The branching ratios of these particular subsequent decay processes are 0.18 and 0.64 respectively. Therefore, approximately 11.8% of the total $Z \rightarrow \tau^+ + \tau^-$ events will have exactly the same event topology as that of $W$+jets process. Since the total cross section of $W + n(> 0)$ jets processes is comparable to

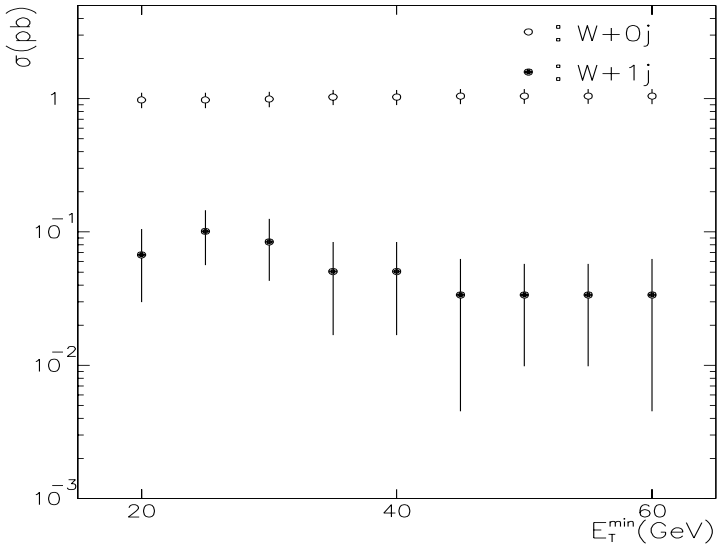


Figure 4.10: Effective cross section of $Z \rightarrow \tau^+ + \tau^-$ Monte Carlo samples ($\sigma_{eff}(Z \rightarrow \tau^+ + \tau^-)$) vs $E_T^{min}$ in the CC.

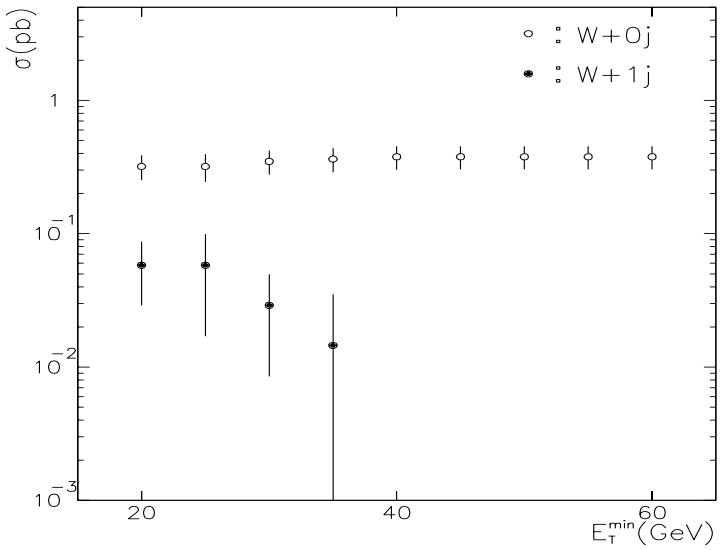


Figure 4.11: Effective cross section of $Z \rightarrow \tau^+ + \tau^-$ Monte Carlo samples ($\sigma_{eff}(Z \rightarrow \tau^+ + \tau^-)$) vs $E_T^{min}$ in the EC.

| $E_T^{min}$ $(GeV)$ | CC 0j$\pm stat \pm sys$(pb) | CC 1j $\pm stat \pm sys$ (pb) |
|---|---|---|
| 20.0 | $0.98\pm0.13^{-0}_{+0}$ | $0.07\pm0.03^{+0}_{-0.02}$ |
| 25.0 | $0.98\pm0.13^{-0}_{+0.02}$ | $0.10\pm0.04^{+0.02}_{-0.02}$ |
| 30.0 | $0.99\pm0.13^{-0}_{+0.02}$ | $0.08\pm0.04^{+0}_{-0.02}$ |
| 35.0 | $1.03\pm0.13^{-0.02}_{+0}$ | $0.05\pm0.03^{+0.02}_{-0}$ |
| 40.0 | $1.03\pm0.13^{-0}_{+0.02}$ | $0.05\pm0.03^{+0}_{-0.02}$ |
| 45.0 | $1.04\pm0.13^{-0.02}_{+0}$ | $0.03\pm0.02^{+0.02}_{-0}$ |
| 50.0 | $1.04\pm0.13^{-0}_{+0}$ | $0.03\pm0.02^{+0}_{-0}$ |
| 55.0 | $1.04\pm0.13^{-0}_{+0}$ | $0.03\pm0.02^{+0}_{-0}$ |
| 60.0 | $1.04\pm0.13^{-0}_{+0.02}$ | $0.03\pm0.02^{+0}_{-0.02}$ |

Table 4.4: $\sigma_{eff}(Z \rightarrow \tau^+ + \tau^-)$ for jet minimum $E_T$ cutoff in the CC.

the total cross section of $Z \rightarrow \tau^+ + \tau^-$, the background contribution from this process can not be ignored.

Since this process is not separable from the signal in the data, full DØ detector simulated ISAJET Monte Carlo samples were used to estimate the contribution from this process. The total number of events used was 10028 which corresponds to $(50.9 \pm 0.51)\ pb^{-1}$. There were no specific cuts applied at the generation stage nor were any specific decay modes of the $\tau$ selected. The response of the detector was simulated with the shower library (a fast version of the full DØ detector simulation without tracking) and reconstructed with the DØ reconstruction program. Then the standard selection criteria (see section 3.3 are applied. The effective integrated cross sections as a function of jet minimum $E_T$ cutoff are tabulated in Table 4.4 and Table 4.5 for electrons in the CC and the EC, respectively. The column "sys" in the table represents

| $E_T^{min}$ $(GeV)$ | EC 0j$\pm stat \pm sys$(pb) | EC 1j $\pm stat \pm sys$ (pb) |
|---|---|---|
| 20.0 | $0.32\pm0.07^{-0}_{+0}$ | $0.06\pm0.03^{+0}_{-0}$ |
| 25.0 | $0.32\pm0.07^{-0}_{+0.03}$ | $0.06\pm0.03^{+0}_{-0.03}$ |
| 30.0 | $0.35\pm0.07^{-0}_{+0}$ | $0.03\pm0.02^{+0}_{-0}$ |
| 35.0 | $0.36\pm0.07^{-0.01}_{+0.01}$ | $0.01\pm0.01^{+0.01}_{-0.01}$ |
| 40.0 | $0.38\pm0.07^{-0.01}_{+0}$ | $0\pm0^{+0.01}_{-0}$ |
| $\geq$45.0 | $0.38\pm0.07^{-0}_{+0}$ | $0\pm0^{+0}_{-0}$ |

Table 4.5: $\sigma_{eff}(Z \rightarrow \tau^+ + \tau^-)$ for jet minimum $E_T$ cutoff in the EC.

the systematic error due to the jet energy scale calibration. The total effective cross section from this process is $(1.45 \pm 0.18)$ pb (see the cross sections at $E_T^{min} = 45$ GeV) which is about 0.2% of the effective inclusive $W$ cross section. Since the electrons in $\tau$ decay have typically low $E_T$, the main rejection power on this process comes from the high threshold on the $E_T$ of electrons.

### 4.2.3 Drell-Yan $(q\bar{q} \rightarrow \gamma \rightarrow e^+ + e^-)$

This process can mimic the $W + jets$ signal in exactly the same way as $Z \rightarrow e^+ + e^-$. However, because the invariant mass of the final state electrons from this process is low compared to the mass of Z so that the $E_T$ distributions of the final state electrons peak at low transverse energy relative to those of the $Z$ and the cross section is comparable to that of the $Z$, it does not contribute as much as the previous two processes. An analysis using 596 full DØ detector simulated ISAJET Monte-Carlo events showed that after the standard $W$ selection criteria were applied, no events survived. Since this particular sample

corresponds to $(2.0 \pm 0.08) pb^{-1}$, the upper limit for the effective inclusive cross section is set to 1.5 pb at 95% confidence level.

### 4.2.4 $W[\rightarrow \tau(\rightarrow e\nu_e\nu_\tau) + \nu] + X$

Since this process has the same final state event topology as $W \rightarrow e+\nu$, it contributes as a background source. In fact, this process is one of the significant backgrounds for inclusive $W$ studies. The total cross section of $W \rightarrow e + \nu$ process is roughly 2.19nb [50] and so is for $W \rightarrow \tau + \nu$ process. The branching ratio of the $\tau \rightarrow e\nu_e\nu_\tau$ is approximately 18%. The contribution from this process to the $W$ inclusive study can be on the order of a few %. However, the production mechanism of jets associated with a $W$ boson is independent of the decay mode of the $W$. Therefore, the background from this process does not affect the final measurement of the ratio of the $W + 1$ jet to the $W + 0$ jet cross sections. Thus this background source can be ignored for this analysis.

## 4.3 Summary of estimated backgrounds

Various background sources have been studied either from the collider data or from the Monte Carlo events. Table 4.6 summarizes the combined number of background events from the various sources for the $W$ + 1jet and $W$ + 0jet events as a function of $E_T^{min}$. Table 4.7 summarizes the number of signal events after background subtraction. The errors in Tables 4.6 and 4.7 are the statistical uncertainty, the systematic error due to the uncertainty

| $E_T^{min}$(GeV) | $N_{0j} \pm stat \pm sys(\mathrm{L}) \pm sys(E_j)$ | $N_{1j} \pm stat \pm sys(\mathrm{L}) \pm sys(E_j)$ |
|---|---|---|
| 20.0 | $486.9 \pm 20.6 \pm 4.4^{-62.6}_{+16.0}$ | $293 \pm 18.1 \pm 1.85^{+35.6}_{-8.61}$ |
| 25.0 | $557.4 \pm 23.0 \pm 4.95^{-30.9}_{+28.8}$ | $255.2 \pm 17.0 \pm 1.36^{+32.3}_{-26.5}$ |
| 30.0 | $676.6 \pm 24.3 \pm 5.02^{-85.0}_{+14.8}$ | $186.7 \pm 14.6 \pm 1.28^{+26.7}_{-12.4}$ |
| 35.0 | $715.9 \pm 26.4 \pm 5.65^{-21.4}_{+11.1}$ | $147.6 \pm 13.1 \pm 0.66^{+22.86}_{-6.64}$ |
| 40.0 | $719.5 \pm 26.6 \pm 5.68^{-10.4}_{+54.5}$ | $144.0 \pm 11.7 \pm 0.63^{+6.35}_{-33.1}$ |
| 45.0 | $782.7 \pm 26.9 \pm 5.71^{-57.0}_{+14.5}$ | $106.1 \pm 11.8 \pm 0.60^{+32.15}_{-19.87}$ |
| 50.0 | $826.3 \pm 28.3 \pm 5.71^{-23.5}_{+20.6}$ | $70.5 \pm 9.42 \pm 0.60^{+18.23}_{-12.13}$ |
| 55.0 | $858.1 \pm 29.0 \pm 5.71^{-19.5}_{+6.6}$ | $53.2 \pm 8.06 \pm 0.60^{+11.7}_{-1.56}$ |
| 60.0 | $864.3 \pm 29.1 \pm 5.71^{-20.2}_{+16.0}$ | $52.7 \pm 7.59 \pm 0.60^{+4.95}_{-10.7}$ |

Table 4.6: Number of background events

| $E_T^{min}$(GeV) | $N_{0j} \pm stat \pm sys(\mathrm{L}) \pm sys(E_j)$ | $N_{1j} \pm stat \pm sys(\mathrm{L}) \pm sys(E_j)$ |
|---|---|---|
| 20.00 | $7801.08 \pm 88.32 \pm 4.40^{-230.36}_{+233.98}$ | $903.04 \pm 30.05 \pm 1.85^{+167.40}_{-187.61}$ |
| 25.00 | $8279.60 \pm 90.99 \pm 4.95^{-150.11}_{+118.20}$ | $527.80 \pm 22.97 \pm 1.36^{+102.68}_{-90.47}$ |
| 30.00 | $8449.35 \pm 91.92 \pm 5.02^{-40.00}_{+74.23}$ | $371.31 \pm 19.27 \pm 1.28^{+64.27}_{-58.59}$ |
| 35.00 | $8583.10 \pm 92.6 \pm 5.65^{-80.59}_{+84.07}$ | $270.37 \pm 16.44 \pm 0.66^{+64.14}_{-58.36}$ |
| 40.00 | $8700.54 \pm 93.28 \pm 5.68^{-67.57}_{+4.46}$ | $165.96 \pm 12.88 \pm 0.63^{+79.35}_{-18.95}$ |
| 45.00 | $8720.29 \pm 93.38 \pm 5.71^{-2.99}_{+20.47}$ | $130.88 \pm 11.44 \pm 0.60^{+14.85}_{-9.13}$ |
| 50.00 | $8730.71 \pm 93.44 \pm 5.71^{-16.50}_{+9.44}$ | $121.49 \pm 11.02 \pm 0.60^{+15.77}_{-15.87}$ |
| 55.00 | $8735.88 \pm 93.47 \pm 5.71^{-10.55}_{+14.37}$ | $105.78 \pm 10.29 \pm 0.60^{+16.27}_{-18.56}$ |
| 60.00 | $8761.70 \pm 93.60 \pm 5.71^{-9.84}_{+9.01}$ | $79.34 \pm 8.91 \pm 0.60^{+22.05}_{-11.30}$ |

Table 4.7: Number of signal events after background subtraction.

in the luminosity measurement, and the systematic error from the jet energy scale uncertainty. The error in the luminosity measurement is estimated to be 12%. However, the error due to luminosity cancels out when the ratio of the number of events of the $W + 1$ jet to the $W + 0$ jet is measured.

The systematic error due to the jet energy scale calibration uncertainty is amplified in the number of the $W + 1$ jet events (for example at $E_T^{min}$=25 GeV, the error in the number of events in Tab. 4.7 is approximately 18%). This is due to $E_T$ distribution of the highest $E_T$ jet in the events. A crude exponential fit ($\chi^2$/DOF=11.0) on the $E_T$ distribution is:

$$\frac{dN(E_T)}{dE_T} = e^{9.28-0.14E_T}. \tag{4.1}$$

The number of the $W + 1$ jet candidate is then the integration of Eq. 4.1 in $E_T$ above the threshold ($E_T^{min}$). Therefore, the effect of the uncertainty in the numebr of the $W+1$ jet candidates due to the jet energy scale uncertainty (6%) can be estimated by computing the areas above the thresholds and comparing the difference. So the uncertainty of the number of the $W + 1$ jet events above a certain $E_T^{min}$ is:

$$\frac{N(1.06 \times E_T^{min}) - N(E_T^{min})}{N(E_T^{min})} = \frac{\frac{e^{9.28}(e^{-0.14\times 1.06E_T^{min}} - e^{-0.14E_T^{min}})}{0.14}}{\frac{e^{9.28-0.14E_T^{min}}}{0.14}}. \tag{4.2}$$

Using Eq. 4.2, the uncertainty at $E_T^{min}$=25 GeV is:

$$\frac{\Delta N(25GeV)}{N(25GeV)} = \mid e^{-0.14\times 0.06\times 25} - 1 \mid = 0.189. \tag{4.3}$$

So the variation of the number of the $W + 1$ jet candidates is approximately 19%. Therefore, the jet energy scale uncertainty is very crucial to this analysis,

because the error in jet energy scale is amplified a great deal (about factor three at $E_T$=25 GeV) due to the $E_T$ distribution of the highest $E_T$ jet. The effect of the jet energy scale uncertainty to the results of the measured ratio and the values of $\alpha_s$ is dominated by the systematic error in the number of $W + 1$ jet candidates, because the effect of the jet energy scale uncertainty on the $W + 0$ jet is much smaller (on the order of 2% at $E_T^{min} = 25$GeV) than that on the $W + 1$ jet events.

# Chapter 5

# $\alpha_s$ determination

The theoretical prediction of physical observables in high momentum transfer processes can be achieved by perturbative QCD. Then the physical observable is measured by experiment and compared with the theoretical predictions for a quantitative test of QCD.

The physical observable used in this analysis is the ratio between the cross section of the $W + 1$ jet [4] final state and that of the $W + 0$ jet [3] final state. The cross sections of these processes are predicted with next-to-leading order perturbative QCD. This enables not only a direct comparison of the experimental results with the theoretical prediction, but also a determination of the value of $\alpha_s$. The prediction is given by a Monte Carlo program called DYRAD [4].

The theoretical aspects of the cross section calculations are discussed followed by a discussion of the Monte Carlo. The method used to determine $\alpha_s$ will close this chapter.

## 5.1 The theoretical cross section calculations

The lowest order matrix elements for the $W$+jets processes at hadron colliders,

$$p\bar{p} \rightarrow W^{\pm} + njets, \tag{5.1}$$

have been computed for $n \leq 4$ [51] [52] [53] [54] using various techniques [55] to control the rapid growth of the number of Feynmann diagrams as the number of involved partons increases. The cross section is then obtained by Monte Carlo integration of the final state parton phase space. This approach makes applications of any experimental jet algorithm and acceptance limitation possible. Because the integration is done at the final state, the exclusion of a certain region of phase space can easily be done. For instance, cone algorithms are commonly used in $p\bar{p}$ experiments to define jets. The cone of radius $\Delta R$ limits the phase space which can be occupied by other partons in an event in the final state. These restrictions of the final state phase space based on jet algorithms provide an experimentally compatible cross section for the processes in which jets are involved.

From the theoretical point of view, the jet algorithm plays an important role in selecting high momentum transfer events by a cut on the jet minimum $E_T$ which keeps the phase space in the perturbative QCD regime. The individual hadron behavior is averaged out within a cone of a given size and is represented by a single jet with the given axis and energy. This averaging of hadron behavior enables the comparison between experimentally observed hadronic jets with the theoretically predicted jets reconstructed from the par-

ton shower. The jet axis and energy observed in the experiment from the hadronic shower are thus modeled by the jet axis and energy obtained from the parton shower. This is a weak form of the parton-hadron duality theorem [56]. The parton-hadron duality theorem states that there is a correspondence between parton and hadron distributions in hard processes. In other words, even if the dynamics of the colorless final states (hadrons) involving low momentum transfer cannot be predicted by perturbative QCD, the global picture of the final state hadronic clusters in hard processes is in principle calculable from perturbative QCD. The hadronization is not predicted by perturbative QCD because the momentum transfer involved in the hadronization process is not sufficiently high. However, a reasonable jet algorithm should be able to minimize the hadronization effects and allow a fairly direct comparison between theoretical predictions and experimental results.

In leading order, jets are defined by applying cuts on partons whose direction and energy are the jet axis and energy. The lowest order predictions of perturbative QCD have been compared with experimental data [57] and have been proved reasonable. However, parton showering is not present in the leading order.

In next-to-leading order radiative corrections are included in the $W + 1$ jet cross section. Virtual corrections involving a loop from the $W + 1$ parton process contribute to the $W + 1$ jet cross section. Real corrections in the form of the $W + 2$ parton final states are also taken into account. The matrix elements from virtual corrections are infrared divergent. On the other hand, the real corrections from the $W + 2$ parton process are divergent when they are in-

tegrated over the final state phase space, because the jet algorithm allows soft parton radiation as well as a collinear radiation of the second parton within the cone. These two divergences cancel each other in the integration over the final state phase space.

The addition of next-to-leading order effects has the following advantages:

- The correction from the next-to-leading order to leading order can be measured by comparing the two predictions. The comparison provides a measure of reliability of the QCD calculations.

- The dependence of the cross sections (or physical observables) on the unphysical renormalization scale, $\mu_R$, is reduced so that the normalization is better defined.

- Parton showers can be partially modeled by allowing two partons to form a single jet. This enables a more realistic simulation of experimental results.

- Since the radiation outside of the detector coverage is simulated by limiting the final state parton phase space, the calculation becomes more sensitive to detector limitations. This enables a more realistic detector simulation from the theoretical predictions by reconstructing the missing $E_T$ rather than an unmeasurable neutrino. At the same time the contributions from higher order processes due to parton radiation outside of the detector coverage is taken into account.

- The transverse momentum ($P_T$) distribution of the $W$ in the higher $P_T$ region is better predicted compared to predictions from the leading order calculations [58].

## 5.2 DYRAD

The Monte Carlo program used in this analysis is called DYRAD. It is a Matrix Element (ME) Monte Carlo which generates a theoretical prediction of cross sections rather than events. DYRAD is based on the recent next-to-leading order (NLO) calculation [3] [4] [58]. Originally, DYRAD predicted cross sections for the $W+1$ jet and that of the $W+0$ jet processes using a given jet algorithm. However, since the physical observable chosen to determine the strong coupling constant, $\alpha_s$, in this analysis is the ratio of the cross section of the W+1jet and the W+0jet processes, it was found that parameterizing the cross sections makes the $\alpha_s$ determination unambiguous. Therefore, DYRAD has been modified to provide parameters of the cross sections. The cross sections for the $W + 0$ jet process as a function of $\alpha_s$ is:

$$\sigma_{W+0j}(LO) = A_0. \tag{5.2}$$

$$\sigma_{W+0j}(NLO) = A_0 + \alpha_s A_1(E_T^{min}) \tag{5.3}$$

in leading order and next-to-leading order, respectively. By the same token the cross sections of the $W + 1$ jet process can be parameterized as:

$$\sigma_{W+1j}(LO) = \alpha_s B_0(E_T^{min}) \tag{5.4}$$

$$\sigma_{W+1j}(NLO) = \alpha_s B_0(E_T^{min}) + \alpha_s^2 B_1(E_T^{min}, \Delta R) \tag{5.5}$$

in leading order and next-to-leading order, respectively. Here $\Delta R$ is the jet cone size. The parameters $A_0$, $A_1(E_T^{min})$, $B_0(E_T^{min})$, and $B_1(E_T^{min}, \Delta R)$ are given by DYRAD. Since the parameters are coefficients of the cross sections and are independent of $\alpha_s$, one can determine the value of $\alpha_s$ without worrying about what value of $\alpha_s$ is used for the theoretical predictions of the cross sections.

Figure 5.1 illustrates some lowest order Feynman diagrams for the $W + 0$ parton, $W + 1$ parton, and $W + 2$ parton processes. In leading order the $W + 0$ jet process includes only figure 5.1a. On the other hand, in next-to-leading order the cross section of the $W + 0$ jet process receives contributions from the $W + 1$ parton diagram when the parton does not satisfy the jet minimum $E_T$ cut ($E_T^{min}$) or escapes the detector coverage. As explained in the previous section the detector coverage is taken into account in the prediction through the final state phase space integration.

In leading order the $W + 1$ jet cross section has contributions from only the $W + 1$ parton diagram which is subject only to the $E_T^{min}$ cuts of the jet algorithms. The detector coverage effect in the leading order only decreases the $W + 1$ jet cross section, because even if a parton is involved in this process, it is no longer considered as $W + 1$ jet process if this parton escapes from the integrated region of the phase space (detector coverage). However, in next-to-leading order the $W + 1$ jet cross section is affected by the $E_T^{min}$ and the cone size as well as the detector coverage. In the next-to-leading order the cone

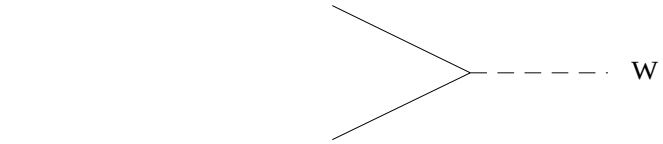


a) W + 0 parton


b) W + 1 parton

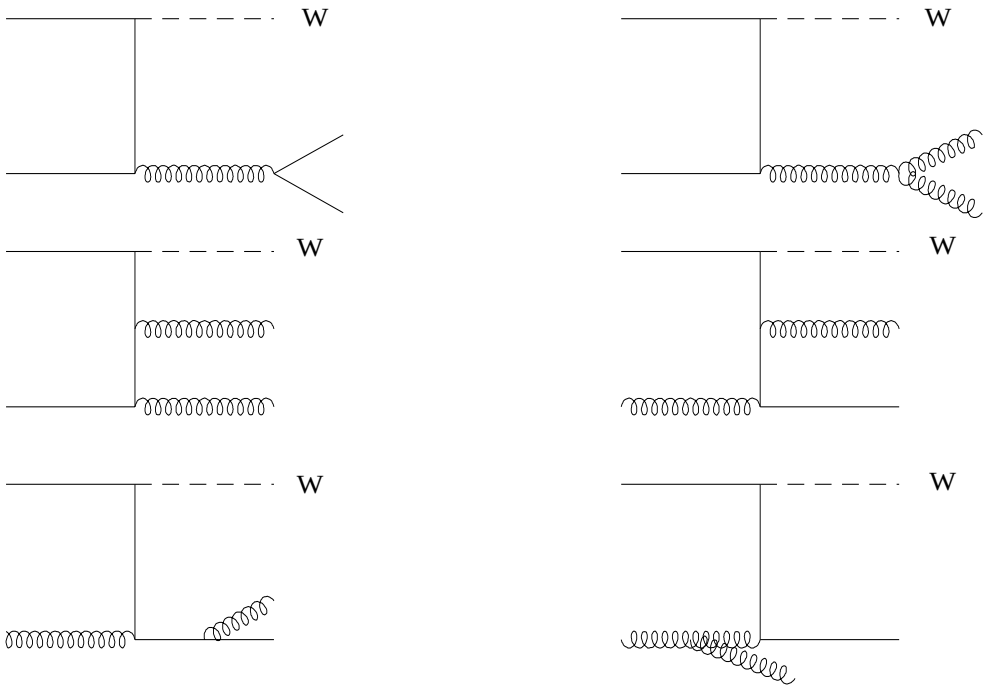


c) W + 2 partons

Figure 5.1: Some lowest order Feynmann diagrams for W+0 parton, 1 parton, and 2 parton processes

| Parameters | values |
|---|---|
| Jet cone size | 0.7 |
| Lepton isolation cone size | 0.4 |
| Lepton(e) kinematic cut | 25 GeV |
| Missing $E_T$ cut | 25 GeV |
| Center of mass energy ($\sqrt{s}$) | 1.8 TeV |
| Standard Model parameters | |
| $M_Z$, , $_Z$ | 91.0 GeV, 2.5GeV |
| $M_W$, , $_W$ | 80 GeV, 2.0GeV |

Table 5.1: Parameters used for DYRAD Monte Carlo generation

size effect comes in because the $W + 1$ jet process has contributions from the $W + 2$ parton diagrams. Whenever the second parton is inside a given cone around the other parton in the process, these two partons form a single jet. The jet four momentum is then the vector sum of the four momenta of these two partons. In addition, when the second parton in the process escapes form the detector coverage, this process becomes the $W + 1$ jet process.

Since in most theoretical Monte Carlo programs detector effects are not taken into account, the direct comparison of the experimental results with theoretical predictions is not possible unless the detector effects are removed. For this analysis, DYRAD has been modified to include smearing effects due to the DØ calorimeter jet energy resolution so that the prediction can be directly comparable to the experimental results. The smearing is done with

a Gaussian function with the width given by the measured DØ resolution ($\sqrt{1.5^2/E_T^2 + 0.7^2/E_T}$). This scheme is applied on the jets after the jets are formed from partons.

DYRAD has a feature for the reconstruction of the missing $E_T$ to provide a realistic simulation of the detector. In general, theoretical predictions involving neutrinos, the source of $\not\!\!E_T$ , have no detector coverage built in, so that the neutrino $E_T$ is not the same as the $\not\!\!E_T$ from the experiment. DYRAD is also capable of computing cross sections based on the experimental offline selections, such as kinematic cuts on the $W$ decay products, lepton isolation requirements, rapidity coverage of a detector for jets, etc.

It is very important for this analysis to keep the theoretical and experimental systematic errors as identical as possible, so that the systematic errors within the experimental data and within the theoretical prediction can be canceled out when taking the ratio. At the same time, by keeping the kinematic acceptances the same between the experiment and the theory, the effect of expected bias due to the kinematic acceptances can be canceled when the theoretical prediction and the experimental results are compared. The same isolation criterion is used for both the experiment and the theory so that the possible bias from the isolation can also be eliminated. More details in this aspect are discussed in the following section. Table 5.1 summarizes the parameters used for the Monte Carlo predictions.

## 5.3 Method of $\alpha_s$ determination

The jet algorithms play an important role in the next-to-leading order predictions. In this analysis a cone algorithm is used. The size of the cone is fixed at $\Delta R = \sqrt{\Delta\eta^2 + \Delta\phi^2} = 0.7$. The jet minimum $E_T$ cut off ($E_T^{min}$) values are varied so that the behavior of the ratio can also be studied. Since DYRAD can provide predictions of the ratio for several $E_T^{min}$ values, a comparison between theoretical predictions of the behavior of the ratio as a function of $E_T^{min}$ and the experimental results provides a good quantitative test of perturbative QCD [5].

In this analysis the determination of $\alpha_s$ is done by using the ratio between the cross sections of the $W + 0$ jet and that of the $W + 1$ jet processes. It is clear from Eqs. 5.2 and 5.4 that in leading order (LO) this ratio is directly proportional to the strong coupling constant, $\alpha_s$. Therefore, measurement of the ratio provide a means of determining the value of $\alpha_s$. These processes have been used to determine $\alpha_s$ by the $UA1$ and the $UA2$ experiments at the $\sqrt{s} = 630GeV$ and $546GeV$ [2]. However, since at the time of these measurements, no next-to-leading order prediction was available, parameters called K-factors had to be introduced to compensate the lack of the higher order corrections in the prediction. Now that the next-to-leading order predictions for the $W + 0$ jet [3] and the $W + 1$ [4] jet cross sections are available, the K-factors are not necessary.

The ratio from experimental measurement can be obtained as:

$$R_{data}(E_T^{min}) = \frac{N_{W+1jet}(E_T^{min})}{N_{W+0jet}(E_T^{min})} \tag{5.6}$$

where $N_{W+1jet}(E_T^{min})$ and $N_{W+0jet}(E_T^{min})$ are number of events after background subtraction at a certain $E_T^{min}$ for the $W+1$ jet and the $W+0$ jet events, respectively. Likewise, the theoretical prediction of the ratio of the cross sections of the $W+1$ jet and the $W+0$ jet processes can be obtained by using the cross sections in Eqs. 5.2, 5.4, 5.3, and 5.5. The ratio of the cross sections in leading order can be written as:

$$R_{LO} = \frac{\sigma_{W+1j}(LO)}{\sigma_{W+0j}(LO)} = \alpha_s \frac{B_0(E_T^{min})}{A_0}. \tag{5.7}$$

Now we replace $R_{LO}$ from the theoretical predictions with the ratio measured from experiment in Eq. 5.6. Then $\alpha_s$ from Eq. 5.7 is

$$\alpha_s(LO) = R_{data} \frac{A_0}{B_0(E_T^{min})}. \tag{5.8}$$

In next-to-leading order the ratio becomes,

$$R_{NLO} = \frac{\sigma_{W+1j}(NLO)}{\sigma_{W+0j}(NLO)} = \alpha_s \frac{B_0(E_T^{min}) + \alpha_s B_1(E_T^{min}, \Delta R)}{A_0 + \alpha_s A_1(E_T^{min})}. \tag{5.9}$$

To demonstrate what the K-factors are, one can rewrite Eq. 5.9,

$$R_{NLO} = \alpha_s \frac{B_0(E_T^{min})[1 + \alpha_s \frac{B_1(E_T^{min}, \Delta R)}{B_0(E_T^{min})}]}{A_0[1 + \alpha_s \frac{A_1(E_T^{min})}{A_0}]} = R_{LO} K(\alpha_s). \tag{5.10}$$

Then the K above can be separated in two terms as follows:

$$K(\alpha_s) = \frac{1 + \alpha_s \frac{B_1(E_T^{min}, \Delta R)}{B_0(E_T^{min})}}{1 + \alpha_s \frac{A_1(E_T^{min})}{A_0}} \tag{5.11}$$

$$= [1 + \alpha_s \frac{B_1(E_T^{min}, \Delta R)}{B_0(E_T^{min})}][1 + \sum_{i=1}^{\infty}(-\alpha_s \frac{A_1(E_T^{min})}{A_0})^i] \tag{5.12}$$

$$\simeq 1 + \alpha_s[\frac{B_1(E_T^{min}, \Delta R)}{B_0(E_T^{min})} - \frac{A_1(E_T^{min})}{A_0}] + O(\alpha_s^2) \tag{5.13}$$

$$\simeq 1 + \alpha_s[K_1 - K_0] = 1 + \alpha_s K^{'}. \tag{5.14}$$

where $K_1$ and $K_0$ correspond to the K-factors used in the other experiments.

However, in this analysis the direct solution of Eq. 5.9 is used to determine $\alpha_s$. We replace the ratio from the theory by the ratio measured from the experiment in Eq. 5.9. The Eq. 5.9 is then multiplied by the denominator and becomes a second degree equation for $\alpha_s$ as follows:

$$B_1(E_T^{min}, \Delta R)\alpha_s^2 + [B_0(E_T^{min}) - A_1(E_T^{min})R_{data}]\alpha_s - R_{data}A_0 = 0. \tag{5.15}$$

Then the solutions for $\alpha_s$ can be found by solving the above equation for $\alpha_s$. These solutions are:

$$\alpha_s = \frac{-[B_0(E_T^{min}) - A_1(E_T^{min})R_{data}]}{2B_1(E_T^{min}, \Delta R)} \tag{5.16}$$

$$\pm \frac{\sqrt{[B_0(E_T^{min}) - A_1(E_T^{min})R_{data}]^2 + 4B_1(E_T^{min}, \Delta R)R_{data}A_0}}{2B_1(E_T^{min}, \Delta R)}. \tag{5.17}$$

However, only one of the solutions in Eq. 5.17 is physically meaningful. Since $\alpha_s$ comes with physical observables (cross sections), it needs to be positive definite. Therefore, the solution one chooses is,

$$\alpha_s(NLO) = \frac{-[B_0(E_T^{min}) - A_1(E_T^{min})R_{data}]}{2B_1(E_T^{min}, \Delta R)} \tag{5.18}$$

$$+ \frac{\sqrt{[B_0(E_T^{min}) - A_1(E_T^{min})R_{data}]^2 + 4B_1(E_T^{min}, \Delta R)R_{data}A_0}}{2B_1(E_T^{min}, \Delta R)}. \tag{5.19}$$

| $E_T^{min}$ | $A_0 \pm stat(10^{-3})$ | $A_1 \pm stat(10^{-2})$ | $B_0 \pm stat(10^{-3})$ | $B_1 \pm stat$ |
|---|---|---|---|---|
| 20 | $1.509 \pm 1.421$ | $0.359 \pm 5.386$ | $1.000 \pm 4.953$ | $2.027 \pm 0.505$ |
| 25 | $1.509 \pm 1.421$ | $0.689 \pm 5.392$ | $0.673 \pm 3.511$ | $1.459 \pm 0.402$ |
| 30 | $1.509 \pm 1.421$ | $0.890 \pm 5.394$ | $0.470 \pm 2.563$ | $1.350 \pm 0.372$ |
| 35 | $1.509 \pm 1.421$ | $1.025 \pm 5.394$ | $0.339 \pm 1.930$ | $1.152 \pm 0.340$ |
| 40 | $1.509 \pm 1.421$ | $1.113 \pm 5.394$ | $0.253 \pm 1.490$ | $0.741 \pm 0.267$ |
| 45 | $1.509 \pm 1.421$ | $1.171 \pm 5.393$ | $0.194 \pm 1.180$ | $0.540 \pm 0.242$ |
| 50 | $1.509 \pm 1.421$ | $1.214 \pm 5.393$ | $0.152 \pm 0.946$ | $0.333 \pm 0.179$ |
| 55 | $1.509 \pm 1.421$ | $1.242 \pm 5.392$ | $0.121 \pm 0.768$ | $0.243 \pm 0.163$ |
| 60 | $1.509 \pm 1.421$ | $1.267 \pm 5.392$ | $0.097 \pm 0.627$ | $0.172 \pm 0.115$ |

Table 5.2: Parameters for cross sections in nb's using $MRSD^0$ parton distribution function.

Since all the parameters in Eq. 5.19 are known $\alpha_s$ can be determined by using the solution in Eq. 5.19. Table 5.2 shows a set of these parameters from DYRAD using $MRSD^0$ parton distribution function. The first column of the table is $E_T^{min}$ in GeV and the errors in other columns are statistical errors due to the number of events used to compute the parameters in DYRAD. More detailed theoretical aspects of this method can be found in Ref. [59].

# Chapter 6

# Results

In the following sections the ratio of the number of the $W + 1$ jet to the $W + 0$ jet events is measured and is compared with theoretical predictions. The measured values of $\alpha_s$ conclude the chapter.

The DØ jet energy scale correction is applied to the $E_T$ of all jets. A cone algorithm is used in this analysis. The radius of the cone is fixed to 0.7 in $\eta - \phi$ space. The theoretical predictions used in this analysis use the same experimental jet definitions and offline selection cuts in order to minimize the systematic errors of the comparison.

## 6.1 The ratio of the number of the $W + 1$ jet to the $W + 0$ jet events

Figure 6.1 shows the distribution of the ratio of the number of the $W + 1$ jet and $W + 0$ jet events. The errors on the data points are the statistical uncertainties and the systematic errors due to energy scale added in quadrature.

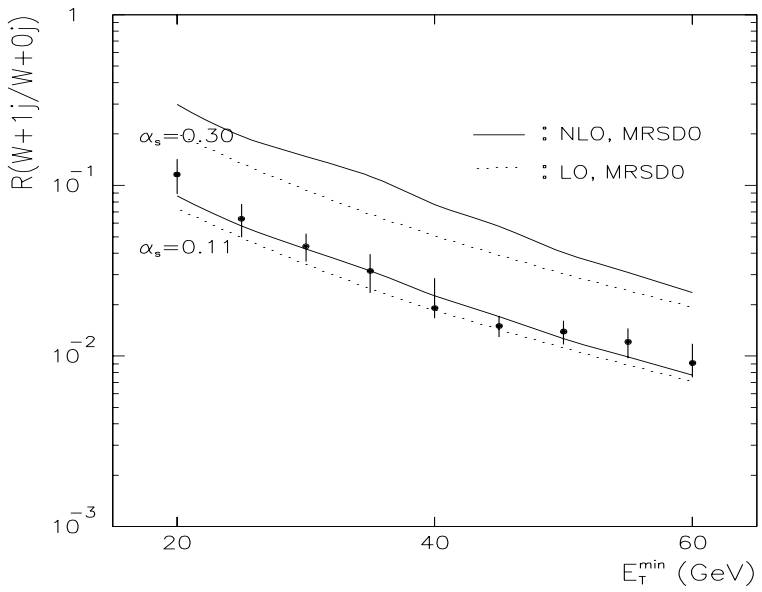


Figure 6.1: Ratio of number of the $W + 1$jet and the $W + 0$jet events vs $E_T^{min}$

The systematic errors due to energy scale is obtained by taking the differences of the central values of the ratio using the nominal jet energy scale correction and the ratios from the upper and the lower error bounds in the corrections (see section 3.2.3). The solid lines in Fig. 6.1 are the next-to-leading order theoretical predictions of the ratio and the dotted lines are the leading order predictions. The theoretical predictions are made with two different $\alpha_s$ values to show the dependence of the ratio on $\alpha_s$. The parton distribution function used for Fig. 6.1 is $MRSD^0$ [60]. The two sets of theoretical predictions show significant differences. The global behavior of the ratio as a function of $E_T^{min}$ shows changes both in the absolute normalization and a weak dependence of the slope on $\alpha_s$. These variations can provide a measure of the strong coupling constant. Table 6.1 summarizes the ratio as a funciton of $E_T^{min}$.

| $E_T^{min}$ (GeV) | $R_{data} \pm stat \pm sys$ |
|---|---|
| 20 | $0.1158 \pm 0.0034^{+0.0256}_{-0.0267}$ |
| 25 | $0.0637 \pm 0.0026^{+0.0138}_{-0.0117}$ |
| 30 | $0.0439 \pm 0.0022^{+0.0079}_{-0.0073}$ |
| 35 | $0.0315 \pm 0.0019^{+0.0078}_{-0.0070}$ |
| 40 | $0.0191 \pm 0.0015^{+0.0093}_{-0.0022}$ |
| 45 | $0.0150 \pm 0.0013^{+0.0017}_{-0.0011}$ |
| 50 | $0.0139 \pm 0.0012^{+0.0018}_{-0.0018}$ |
| 55 | $0.0121 \pm 0.0012^{+0.0019}_{-0.0021}$ |
| 60 | $0.0091 \pm 0.0010^{+0.0025}_{-0.0013}$ |

Table 6.1: Ratio of the number of the $W + 1$ jet and $W + 0$ jet events as a function of $E_T^{min}$.

The leading order prediction showed the change in the absolute normalization but did not show a change in the slope. The data show fair agreement with both next-to-leading order and leading order predictions at $\alpha_s \cong 0.11$. This shows the level of trustworthiness of the leading order prediction.

The behavior of the ratio can be a measure of uncomputed higher order (next-to-next-to-leading order or higher) corrections. This, of course, will require a more precise experimental measurement. At this point the dominant source of uncertainty is the systematic error of the jet energy scale. The uncertainty in the jet energy scale is determined by using the upper and lower bounds of the error bars of the correction factors in Fig. 3.4. The effect of the

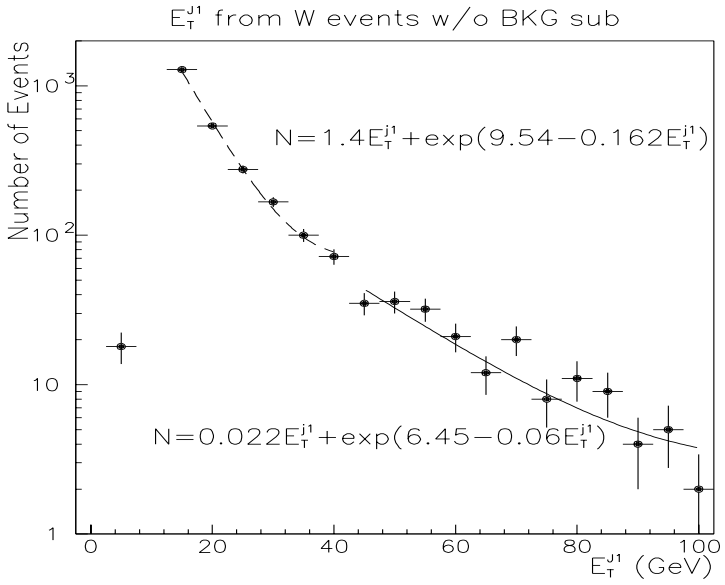


Figure 6.2: $E_T$ distributions of the highest reconstructed jet associated with $W$. The two functions are emprical best fits to the data.

error in the energy scale correction to the ratio is larger than the error itself because of the anti correlation in the number of the $W+1$ jet and the $W+0$ jet events. In other words when the jet energy is over corrected, the number of the $W+1$ jet events increases whereas the number of the $W+0$ jet events decreases. As a result the effect of jet energy systematic error to the ratio is fractionally larger than the error on the jet energy scale itself. In addition, the $E_T$ distribution of the highest $E_T$ jet in the event affects to amplification of the variation of the number of the $W+1$ jet events (see section 4.3). The extreme asymmetry of the energy scale error at $E_T^{min}$=40 GeV can be explained from Fig. 6.2. The large statistical fluctuation at 40 GeV causes the error at this value of $E_T$ to be very asymmetric. Because of the dominant systematic error from the jet energy scale, we are not capable of measuring the level of

correction from the uncomputed higher orders at the current stage. However, since the jet energy scale uncertainty will decrease as our understanding of the detector improves, this measurement will enable us to measure the corrections from higher orders in the perturbative QCD calculations.

## 6.2 Measured value of $\alpha_s$

Using the method described in section 5.3, one can determine the value of the strong coupling constant $\alpha_s$. A value of $\alpha_s$ can be obtained for every value of jet minimum $E_T$ cut ($E_T^{min}$). Figure 6.3 shows the values of $\alpha_s$ as a function of $E_T^{min}$. One naively expects to see no dependence of the measured $\alpha_s$ value on $E_T^{min}$, because $\alpha_s$ is a parameter in perturbative QCD and depends only on the renormalization scale $\mu_R$. In Fig. 6.3, one sees a consistency of the measured $\alpha_s$ values over a wide range of $E_T^{min}$.

However, since the data points are correlated with one another, taking the numerical average of the $\alpha_s$ values is not valid. Therefore, one can only take the value at one point to determine $\alpha_s$. We chose the value of $E_T^{min}$ at 25 GeV as the central value for the determination of $\alpha_s$, because 25 GeV is the first reliable value of $E_T^{min}$ with sufficient statistics and a relatively low systematic error from the jet energy scale uncertainty. Since the events used in this analysis always include a $W$, the choice of the scale in the theoretical prediction is $Q^2 = M_W^2$. Therefore the value of the first order $\alpha_s$ at $Q^2 = M_W^2$

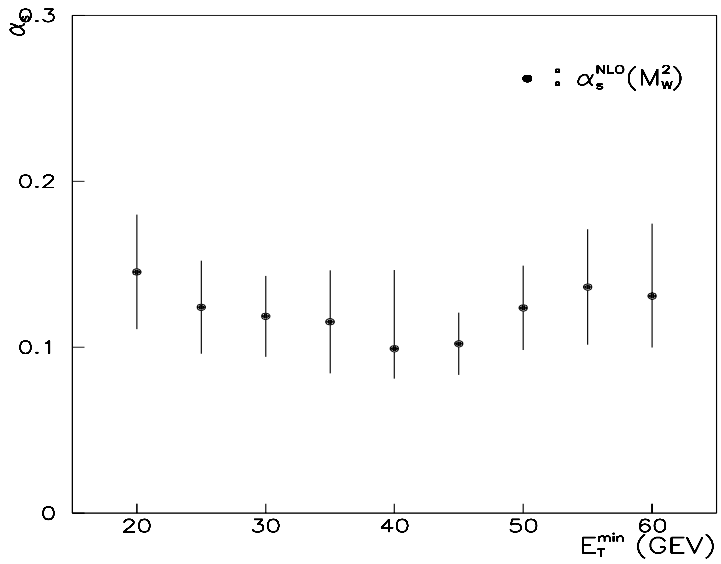


Figure 6.3: Measured values of $\alpha_s$ as a function of jet minimum $E_T$ cut ($E_T^{min}$)

with $E_T^{min}$=25GeV from this analysis is

$$\alpha_s^{NLO}(M_W^2) = 0.124 \pm 0.005(stat) \pm 0.006(MC) \pm 0.008(F_{st})^{+0.026}_{-0.022}(E-scale) \tag{6.1}$$

The corresponding zeroth order $\alpha_s$ value at the same $Q^2$ is,

$$\alpha_s^{LO}(M_W^2) = 0.145 \pm 0.006(stat) \pm 0.001(MC) \pm 0.002(F_{st})^{+0.034}_{-0.029}(E-scale). \tag{6.2}$$

The error from Monte Carlo comes due to the number of events used to generate the parameters in the cross sections of the $W+1$ jet and that of the $W+0$ jet processes. $F_{st}$ is the theoretical systematic error due to the uncertainty in the use of parton distribution functions. This error is the standard deviation of the $\alpha_s$ values from the mean value obtained from six different structure functions. The structure functions used for this analysis are $MRSD^0$, $MRSS^0$, $MRSD^-$ [60], $CTEQ1ML$, $CTEQ1M$, and $CTEQ1MS$ [61] in

| $E_T^{min}$ | $\alpha_s \pm stat(exp) \pm stat(MC) \pm sys(F_{st}) \pm sys(exp)$ | $\Delta\alpha_s$ (combined) |
|---|---|---|
| 20.0 | $0.145 \pm 0.004 \pm 0.007 \pm 0.010^{+0.030}_{-0.032}$ | $^{+0.032}_{-0.035}$ |
| 25.0 | $0.124 \pm 0.005 \pm 0.006 \pm 0.008^{+0.026}_{-0.022}$ | $^{+0.028}_{-0.025}$ |
| 30.0 | $0.119 \pm 0.006 \pm 0.007 \pm 0.011^{+0.020}_{-0.019}$ | $^{+0.025}_{-0.024}$ |
| 35.0 | $0.116 \pm 0.006 \pm 0.008 \pm 0.013^{+0.027}_{-0.025}$ | $^{+0.032}_{-0.030}$ |
| 40.0 | $0.099 \pm 0.007 \pm 0.007 \pm 0.009^{+0.046}_{-0.011}$ | $^{+0.048}_{-0.017}$ |
| 45.0 | $0.102 \pm 0.009 \pm 0.009 \pm 0.009^{+0.011}_{-0.007}$ | $^{+0.019}_{-0.017}$ |
| 50.0 | $0.124 \pm 0.011 \pm 0.013 \pm 0.009^{+0.016}_{-0.017}$ | $^{+0.025}_{-0.025}$ |
| 55.0 | $0.137 \pm 0.013 \pm 0.018 \pm 0.009^{+0.021}_{-0.025}$ | $^{+0.032}_{-0.034}$ |
| 60.0 | $0.131 \pm 0.015 \pm 0.016 \pm 0.007^{+0.037}_{-0.019}$ | $^{+0.043}_{-0.030}$ |

Table 6.2: $\alpha_s$ as a function of $E_T^{min}$

next-to-leading order.

# Chapter 7

# Conclusions

The total number of final $W \rightarrow e + \nu + X$ candidates from $(14.3 \pm 1.7) pb^{-1}$ of data is 9770.

The ratios of the number of the $W + 1$ jet and the $W + 0$ jet events with a decay mode of $W \rightarrow e + \nu$ were measured. This physical observable is predicted by perturbative QCD in leading and next-to-leading order. The experimental results were compared with the theoretical predictions. The comparison showed a good agreement between the experimental results and both the leading and the next-to-leading order theoretical predictions. The difference between the theoretical predictions and the experimental results provides the level of corrections from uncomputed higher orders at any order. However, at this stage, the level of uncertainty due to the experimental systematics is larger than the observed difference.

The value of $\alpha_s$ was determined using the measured ratio at $E_T^{min} = 25$ GeV. Since both the $W + 1$ jet and $W + 0$ jet processes involve a $W$ boson, a sensible choice of the scale would be the mass of $W$ $(M_W)$. Therefore, the

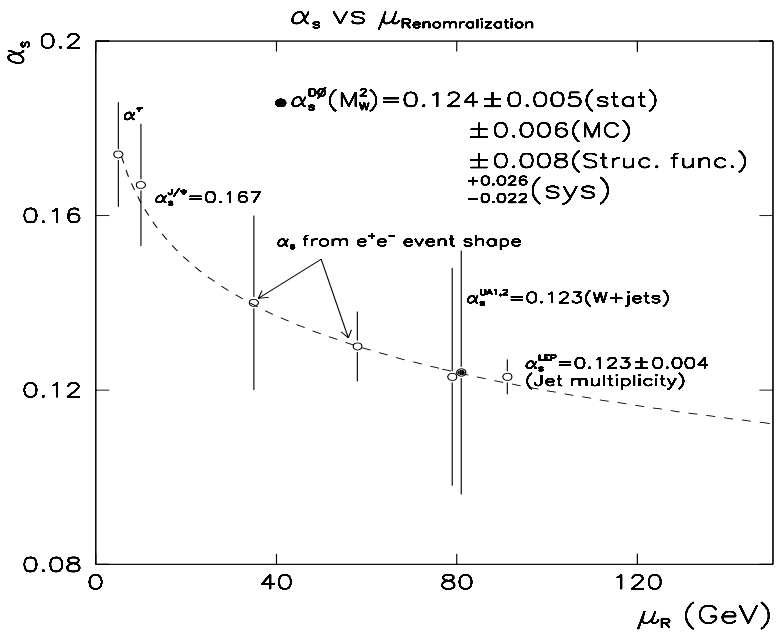


Figure 7.1: Extrapolated values of $\alpha_s$ using the DØ measurement. The dashed line is the extrapolation of $\alpha_s$ using the DØ measurement in Eq.7.2

strong coupling constant, $\alpha_s(Q^2)$, was determined at the scale $Q^2 = M_W^2$ with $E_T^{min}$=25GeV to be

$$\alpha_s = 0.124 \pm 0.005(stat) \pm 0.006(MC) \pm 0.008(F_{st})^{+0.026}_{-0.022}(sys). \qquad (7.1)$$

Once the value of $\alpha_s$ is determined at one $Q^2$ value it is straight forward to extrapolate to other renormalization scale. The relationship of $\alpha_s$ between different $Q^2$ scales is determined from next-to-leading order QCD calculations [59],

$$\alpha_s(Q^2) = \alpha_s(M_W^2)[1 + \alpha_s(M_W^2) b_0 ln(M_W^2/Q^2)] \qquad (7.2)$$

where,

$$b_0 = \frac{11N_c - 2n_f}{12\pi} = \frac{23}{12\pi}, (n_f = 5), \qquad (7.3)$$

$N_c$ is the number of colors and $n_f$ is the number of the excited quark flavors at the scale $Q^2$. Figure 7.1 shows the predicted value of the $\alpha_s$ as a function of renormalization scale ($\mu_R$) compared with the results from other experiments [65]. The extrapolated value of $\alpha_s$ at $\mu_R^2 = M_Z^2$ using Eq. 7.2 is

$$\alpha_s(M_Z^2) = 0.121 \pm 0.007(stat) \pm 0.008(F_{st})^{+0.024}_{-0.022}(sys) \tag{7.4}$$

The recent measurement of $\alpha_s$ from LEP [64] using the jet multiplicity is consistent with the extrapolated value of $\alpha_s$ based on the DØ measurement within the uncertainty as can be inferred from fig. 7.1.

In addition, from the definition of the QCD parameter $\Lambda_{\overline{MS}}$ in the first order of $\alpha_s$,

$$\Lambda^2_{\overline{MS}} = \mu_R^2 exp[\frac{-12\pi}{(33-2n_f)\alpha_s(\mu_R^2)}] \tag{7.5}$$

the value of $\Lambda_{\overline{MS}}$ can be determined using the measured $\alpha_s$ values. The value of $\Lambda_{\overline{MS}}$ with five excited quark flavors in the first order is

$$\Lambda^{(5)}_{\overline{MS}} = 113 \pm 53.9(stat) \pm 61.9(F_{st})^{+245}_{-99.9}(sys) MeV. \tag{7.6}$$

The relationship between four flavor $\Lambda^{(4)}_{\overline{MS}}$ and $\Lambda^{(5)}_{\overline{MS}}$ can be derived using continuity at $Q^2 = m_b^2$ in Eq. 7.5,

$$\Lambda^{(4)}_{\overline{MS}} \approx \Lambda^{(5)}_{\overline{MS}} (\frac{m_b}{\Lambda^{(5)}_{\overline{MS}}})^{\frac{2}{25}}, \tag{7.7}$$

where $m_b$ is the mass of b quark. Therefore, $\Lambda_{\overline{MS}}$ with four light quark flavor using Eq. 7.7 is

$$\Lambda^{(4)}_{\overline{MS}} = 152 \pm 66.9(stat) \pm 75.1(F_{st})^{+284}_{-126}(sys) MeV. \tag{7.8}$$

The statistical uncertainties are the experimental uncertainty and the Monte Carlo uncertainty added in quadrature. $F_{st}$ is the theoretical systematic error due to the use of structure functions determined from the standard deviation from the mean value. The systematic error is due to the uncertainty from the DØ jet energy scale taken upper and lower bound of the errors in the jet energy scale correction (see section 3.2.3). These two values are consistent with other experimental measurements within error [65].

In the future, one can improve the measurement of $\alpha_s$ by taking the differences of the ratio between the cross section of the $W + 1$ jet process and that of the $W + 0$ jet process in various $E_T^{min}$ bins so that the correlations between data points are removed. In this way a more precise measurement is possible by making a use of all available information. Although the current level of error in $\alpha_s$ measurement is much larger than the error from the LEP measurements, this method will eventually provide as accurate measurement as the LEP measurements [64]. The statistical error will be reduced by factor 2 after the next run which is expected to collect approximately factor 3 more statistics. The systematic error due to the use of the parton distribution function will vanish as our understanding of the function improves. The statistical error from MC can be made zero by obtaining more statistics. In addition, the jet energy scale uncertainty will be reduced to a few percent level (2%-5%) [68] [69] as understanding of the detector improves. Therefore, the accuracy of the measurements in $\alpha_s$ can be reduced to about 3%-10% level. This level of error is compatible to the error in the LEP measurements [64].

The importance of this measurement is its quantitative test of pertur-

bative QCD. Since the next-to-leading order prediction for the ratio of the $W+1$ jet to $W+0$ jet as a function of $E_T^{min}$ is available, the correction factors from the higher order can be known to a reasonable accuracy. In addition, the ratio can also provide additional information on the corrections from the uncomputed higher orders. Therefore, although the value of $\alpha_s$ determined LEP experiments are more accurate than the value from this measurement, the importance of the measurement of this ratio is on the precision test of QCD in a different physical process.

# Bibliography

[1] G. Arnison *et al.*, Phys. Lett. **122B**, 103 (1983);
G. Arnison *et al.*, Phys. Lett. **126B**, 398 (1983);
G. Arnison *et al.*, Phys. Lett. **129B**, 273 (1983);
G. Arnison *et al.*, Phys. Lett. **134B**, 469 (1983);
G. Arnison *et al.*, Phys. Lett. **147B**, 241 (1984).

[2] R. Ansari *et al*, (UA2 collaboration), Phys. Lett. **B215**, 175 (1988);
R. Ansari *et al*, (UA2 collaboration), Phys. Lett. **B186**, 440 (1987);
J. Alitti *et al*, (UA2 collaboration), Phys. Lett. **B263**, 563 (1991);
M. Lindgren *et al*, Phys. Rev. **D45**, 3038 (1992).

[3] H. Baer and M. H. Reno, Florida State report FSU-HEP-901030 (1990).

[4] W. T. Giele, E. W. N. Glover and D. A. Kosower, FERMILAB-Pub-92/230-T, 1992 (To be published).

[5] J. Yu, (DØ collaboration), Proceedings of DPF '92, 1094 (1993); FERMILAB-Conf-93/042-E (1993).

[6] D. J. Gross and F. Wilczek, Phys.Rev. **D8**, 3633 (1973).

[7] H. Fritzsch, M Gell-Mann and H. Leutwyler, Phys. Lett. **47B**, 365 (1973)

[8] D. P. Barber *et al*, Phys. Rev. Lett. **43**, 830 (1979);
G. Wolf *et al*, (TASSO collaboration), Lepton/Photon Symp.1979 **34**, QCD161:I71 (1979);
W. Bartel *et al*, (JADE collaboration), Phys. Lett. **91B**, 142 (1980).

[9] S. Coleman and D. J. Gross, Phys. Rev. Lett. **31**, 851 (1973).

[10] J. D. Bjorken, Phys. Rev. **148**, 1467 (1966);
J. D. Bjorken, Phys. Rev. **179**, 1547 (1969).

[11] F. Halzen and Alan D. Martin, "Quarks and Leptons", John Wiley and Sons (1984);
I. J. R. Aichison and A. J. G. Hey, "Gauge Theories in Particle Physics", Adam Hilger Ltd., (1982).

[12] A. Clark *et al* (DØ collaboration), Nucl. Instr. and Methods **A279**, 243 (1989)

[13] A. Clark *et al* (DØ collaboration), Nucl. Instr. and Methods **A315**, 193 (1992)

[14] J,F. Detoeuf *et al* (DØ collaboration), Nucl. Instr. and Methods, **A279**, 310 (1989)

[15] D. Pizzuto, Ph. D. Thesis, State University of New York at Stony Brook, 1989 (Unpublished)

[16] S. Rajagopalan, Ph. D. Thesis, Northwestern University, Evanston, 1992 (Unpublished)

[17] The DØ Collaboration, "The DØ Design Report" (1984)

[18] The DØ collaboration, "The DØ Detector", FERMILAB-PUB-93/179, 1993 (Submitted to Nucl. Instr. and Methods)

[19] S. Aronson *et al*, Nucl. Instr. and Meth. **A269**, 492 (1988)

[20] M. Abolins *et al* (DØ collaboration), Nucl. Instr. and Methods, **A280**, 36 (1989)

[21] H. Aihara *et al* (DØ collaboration), Nucl. Instr. and Methods, **A325**, 393 (1993)

[22] C. Brown *et al* (DØ collaboration), Nucl. Instr. and Methods, **A279**, 331 (1989)

[23] R. Partridge, DØ internal note # 1295, 1991 (Unpublished)

[24] K. McFarland, DØ internal note # 840, 1989 (Unpublished)

[25] M. Abolins *et al* (DØ collaboration), IEEE Trans. Nucl. Sci., **A36**, 384 (1989)

[26] M. Abolins *et al* (DØ collaboration), Nucl. Instr. and Methods, **A289**, 543 (1990)

[27] J. T. Linnemann, (DØ collaboration), Proceedings of DPF '92 , 1641 (1993)

[28] Digital Equipment Corporation, Maryland, Massachusetts.

[29] M. Narain and U. Heintz, DØ internal note #1481, 1992 (Unpublished).

[30] M. Narain, Private conversation.

[31] M. Fatyga, DØ internal note # 1768, 1993 (Unpublished)

[32] A. Boehnlein, DØ internal note # 1664, 1993 (Unpublished)

[33] R. Engelmann *et al*, Nucl. Instr. and Methods **A216**, 45 (1983).

[34] M. Narain, (DØ collaboration), Proceedings of DPF '92, 1678 (1993)

[35] Figure courtesy of M. Narain and U. Heintz.

[36] S. J. Durston, Ph. D. Thesis, University of Rochester, Rochester, NY, 1993 (Unpublished)

[37] N. Hadley, DØ internal note # 904, 1989 (Unpublished)

[38] A. J. Milder, Private coversation.

[39] A. J. Milder and R. V. Astur, DØ internal note #1657, 1993(Unpublished).

[40] F. Abe, *et al*, FERMILAB-Pub-92, 1992 (submitted to Phys. Rev. Lett.).

[41] A. J. Milder, Ph. D. thesis in preparation, Univ. of Arizona, AZ, 1993 (Unpublished).

[42] The working group on LEP energy and the LEP collaborations ALEPH, DELPHI, L3 and OPAL, CERN-PRE/93-53, 1993 (Submitted to Phy. Lett. B).

[43] D. Hedin, private conversation.

[44] S. J. Wimpenny, private conversation.

[45] U. Heintz and M. Narain, DØ internal note #1814, 1993 (Unpublished).

[46] R. V. Astur, DØ internal note #1662, 1993 (Unpublished);
D. Elvira, R. Astur and G. Blazey, DØ internal note #1763, 1993 (Unpublished).

[47] J. Smith, W. L. van Neerven, and J. A. M. Vermaseren, Phys. Rev. Lett. **50**, 1738 (1983).

[48] M. Fatyga and D. Chakraborty, DØ internal note # 1753, 1993 (Unpublished)

[49] M. Paterno, DØ internal note # 1374, 1992 (Unpublished).

[50] F. Abe *et al* (CDF collaboration), Phys. Rev. **D44**, 29 (1991).

[51] F. A. Berends, W. T. Giele, H. Kuijf, R. Kleiss, and W. J. Stirling, Phys. Lett. **B224**, 237 (1989)

[52] R. Kleiss and W. J. Stirling, Nucl. Phys. **B262**, 235 (1984).

[53] F. A. Berends, W. T. Giele and H. Kuijf, Nucl Phys. **B321**, 39 (1989).

[54] F. A. Berends, W. T. Giele, H. Kuijf and B. Tausk, Nucl Phys. **B357**, 32 (1991).

[55] P. de Causmaecker, R. Gastmans, W. Troost and T. T. Wu, Phys. Lett. **B105**, 215 (1981);
R. Kleiss, Nucl. Phys. **B241**, 61 (1984);
F. A. Berends, P. H. Daverveldt and R. Kleiss, Nucl. Phys. **B253**, 441 (1985);
J. F. Gunion and Z. Kunszt, Phys. Lett. **B161**, 333 (1985);
Z. Xu, D. H. Zhang and L. Chang, Nucl. Phys. **B291**, 392 (1987);
F. A. Berends and W. T. Giele, Nucl. Phys. **B294**, 700 (1987);
M. Mangano, S. J. Parke and Z. Xu, Nucl. Phys. **B299**, 673 (1988);
D. Zeppenfeld. Int. J. Mod. Phys. **A3**, 2175 (1988);
F. A. Berends and W. T. Giele, Nucl. Phys. **B306**, 759 (1988);
J. G. M. Kuijf, Ph. D. thesis, Leiden (1991).

[56] D. Amati and G. Veneziano, Phys. Lett. **B83**, 87 (1979);
G. Marchesini, L. Trentadue and G. Veneziano, Nucl. Phys. **B181**, 335 (1981);
Y. I. Azimov, Y. L. Dokshitzer, V. A. Khoze and S. I. Troyan, Z. Phys. **C27**, 65 (1985).

[57] T. Rodrigo, (CDF collaboration), Proceedings of DPF '92, 1097 (1993)

[58] P. Arnold and M. H. Reno, Nucl. Phys. **B319**, 595 (1989).

[59] W. T. Giele and J. Yu, "On the Determination of the Strong Coupling Constant from Vector Boson Production at Hadron Colliders", in preparation.

[60] A. D. Martin *et al*, Phys. Lett. **B306**, 145 (1993); Phys. Lett. **B309**, 492 (1993).

[61] J. G. Morfin *et al* (CTEQ collaboration), Phys. Lett. **B304**, 159 (1993).

[62] F. E. Paige and S. D. Protopopescu, "ISAJET Manual", Brookhaven National Laboratory, Upton, New York (1992)

[63] M. Z. Akrawy *et al.*, Phys. Lett. **235B**, 389 (1990)

[64] S. Banerjee, "Test of QCD at LEP", TIFR/EHEP 93-2 (1993)

[65] G. Altarelli, " QCD and Experiment : Status of $\alpha_s$", CERN-TH.6623/92, 1992 (Unpublished)

[66] A. A. Akhundov *et al*, Phy. Lett. **B223**, 485 (1989)

[67] R. K. Ellis and W. J. Stirling, FERMILAB-Conf-90/164-T (1990)

[68] J. Sculli, Private conversation.

[69] R. Astur, Private conversation.